POLITECNICO

MILANO 1863

Coupling between 3D hemodynamics and reduced immersed valve dynamics for the pulmonary circulation

Tesi di Laurea Magistrale in Mathematical Engineering - Ingegneria Matematica

Author: **Alessandra Messina**

Student ID: 945341
Advisor: **Prof. Christian Vergara**[a]
Co-advisors: **Dr. Ivan Fumagalli**[b]
Academic Year: 2021-2022

[a]Laboratory of Biological Structure Mechanics (LaBS), Dipartimento di Chimica, Materiali e Ingegneria Chimica "Giulio Natta" Politecnico di Milano, Milan, Italy.

[b]Modellistica e Calcolo Scientifico (MOX), Dipartimento di Matematica, Politecnico di Milano, Milan, Italy.

Abstract

In this work we detail an innovative computational framework to study and to numerically simulate the hemodynamics in the pulmonary artery, including the pulmonary valve leaflets.

The blood flow is described by the Navier-Stokes equations, where the valve is represented by the Resitive Immersed Implicit Surface (RIIS) method.

The 3D hemodynamics is coupled with a lumped-parameters model which reproduces the valve dynamics. This model is derived from a local force balance at the leaflets, including the stress exchanged with the blood flow, the elasticity associated to the leaflets curvature and damping effects.

The coupled problem is discretized through a Finite Element (FE) formulation with the Streamline Upwind Petrov-Galerkin and the Pressure-Stabilizing Petrov-Galerkin (SUPG-PSPG) stabilization and a backward differentiation formula (BDF) time scheme.

The study is applied to two clinical cases. The correct reconstruction of the pulmonary artery, and the proper positioning of the valve, in its closed and open positions, are of utmost importance in reproducing the patient-specific hemodynamics.

The results show the suitability of the system in representing the leaflets motion, the blood flow inside the pulmonary artery and the sharp pressure gradient across the pulmonary valve.

Keywords: Cardiac valve dynamics; Computational fluid dynamics; Fluid-structure interaction; Pulmonary circulation.

Abstract in lingua italiana

In questo lavoro dettagliamo un innovativo framework computazionale per studiare e simulare numericamente l'emodinamica nell'arteria polmonare, compresa la valvola polmonare.

Il flusso sanguigno è descritto dalle equazioni di Navier-Stokes, in cui la valvola è rappresentata dal metodo RIIS (*Resistive Immersed Implicit Surface*).

L'emodinamica tridimensionale è accoppiata con un modello a parametri concentrati che riproduce la dinamica valvolare. Tale modello è ottenuto da un bilancio locale di forze agenti sulla valvola, che comprendono gli sforzi scambiati con il flusso sanguigno, l'elasticità associata alla curvatura dei foglietti valvolari ed effetti di smorzamento.

Il problema accoppiato è discretizzato tramite una formulazione a Elementi Finiti (FE) con stabilizzazione SUPG-PSPG (*Streamline Upwind Petrov-Galerkin - Pressure-Stabilizing Petrov-Galerkin*) e uno schema BDF (*backward differentiation formula*) in tempo.

Lo studio è applicato a due casi clinici. La corretta ricostruzione dell'arteria polmonare e l'appropriato posizionamento della valvola, nelle sue configurazioni chiusa ed aperta, sono di estrema importanza nel riprodurre l'emodinamica paziente-specifica.

I risultati mostrano l'adeguatezza del sistema nel rappresentare il movimento dei foglietti valvolari, il flusso sanguigno nella valvola polmonare e il gradiente netto di pressione in corrispondenza della valvola polmonare.

Parole chiave: Dinamica della valvola cardiaca; Fluidodinamica computazionale; Interazione fluido-struttura; Circolazione polmonare.

Contents

1 | Introduction

In this chapter we provide a description of the cardiovascular system, focusing on the pulmonary circulation. We explain the importance of the computational methods in hemodynamics, especially with respect to the cardiac pathologies of the pulmonary valve. A section is devoted to the tetralogy of Fallot, which affects the patients we are considering, and the surgical treatment, the Ross procedure and the prosthetic valve implant. We examine, by means of a literature review, the principal methods to study the fluid-structure interaction between the blood flow and the valve and we mention some of the most representative contributions to the numerical hemodynamics of the pulmonary circulation. Finally, the purpose and the organization of the thesis are presented.

1.1. Overview of the cardiovascular system

The cardiovascular system is a closed circuit whose main task is the transport of blood. It consists of elastic vessels, which bring blood in all the regions of the organism, two circulatory loops, with the aim of carrying oxygenated and non-oxygenated blood, and an organ, the heart, which powers all the system, acting as a pump.

The first of the two circulatory loops is the **systemic circulation**. It is made of arteries, vessels with the aim of carrying oxygenated blood from the left heart to the living tissues, veins, which let, instead, non-oxygenated blood to return to the right heart and the microvasculature, that allows the exchange of nutrients and regulates the blood flow due to the high resistance, which entails the decrease of fluid pressure.

The second loop is the **pulmonary circulation**, in which non-oxygenated blood, ejected by the right heart, flows in the pulmonary arteries towards the lungs, where it becomes oxygenated and goes back to the left heart through the pulmonary veins.

The route of the blood is reported in Figure 1.1.

The **heart** is a hollow, highly evolved organ that combines structural and functional heterogeneity to attain its primary function as a pump. Both the right and the left side consist of two chambers, an atrium and a ventricle. Upper left (LA) and right (RA) atria collect the blood from the veins and lower left (LV) and right (RV) ventricles contract
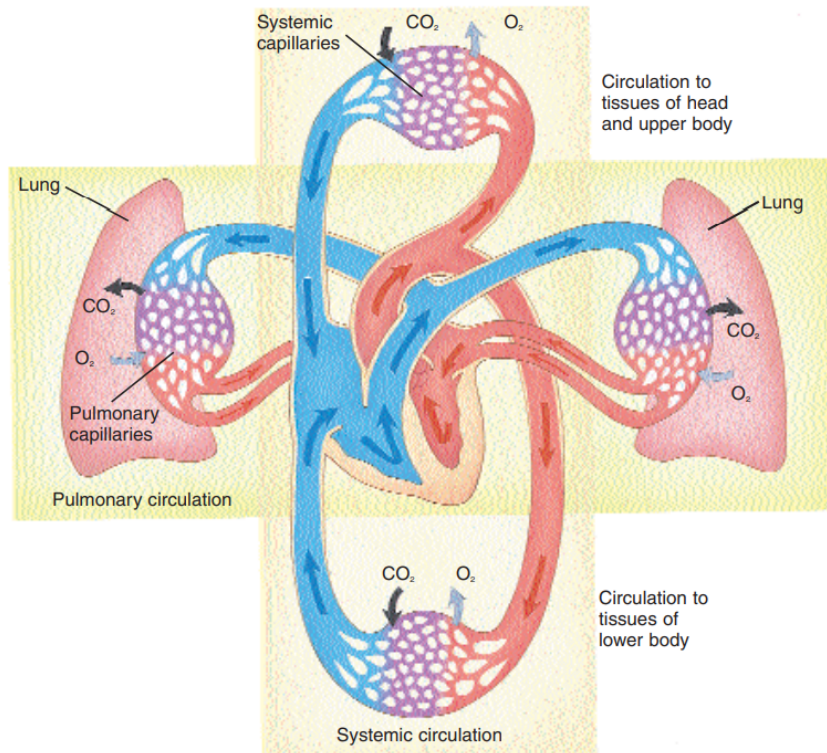
Figure 1.1: Circulatory system. Oxigenated blood is red, non-oxygenated blood is blue [66].

to propel the blood into the systemic and pulmonary arteries. The two ventricles share a septum, which separates the heart into the left and right sides and does not allow the transfer of blood, whereas the atria and the ventricles are connected by the atrioventricular valves (tricuspid valve in the right heart, mitral valve in the left heart) that either allow or prevent the blood transfer from the atria to the ventricles depending on their position, open or closed, respectively. In particular, they open when the atrial pressure is higher than the ventricular pressure and close as soon as the blood flow rate becomes negative, i.e. when the blood flow, which normally goes from the atrium to the ventricle, comes back into the atrium. The papillary muscles, located in the ventricles, attach to the cusps of these valves via the chordae tendineae, preventing their inversion (prolapse) during the closure. All four chambers are connected to the circulatory system: the left ventricle through the aorta, the right ventricle through the pulmonary artery, the left atrium through the pulmonary veins, and the right atrium through the superior and inferior venae cavae. The ventricles are separated from the circulatory system by two further valves, the aortic valve on the left side and the pulmonary valve on the right side, whose opening/closure mechanism is similar to that of the atrioventricular valves, namely they open when the pressure is higher in the ventricle with respect to the corresponding connected artery, whereas they close when the flow rate becomes negative, i.e. going

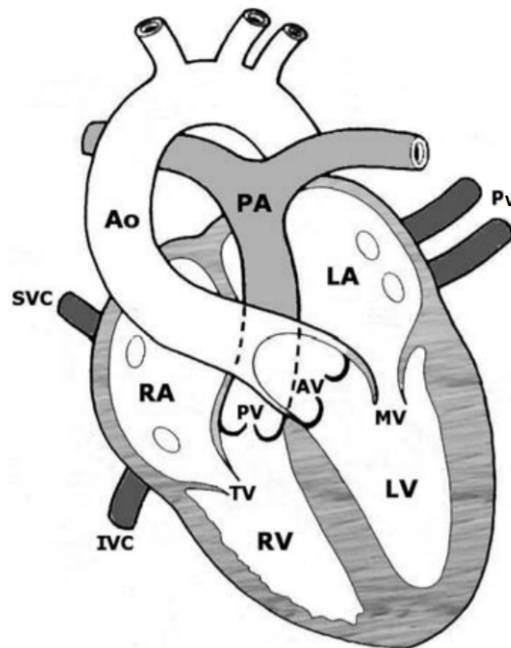Figure 1.2: Schematic representation of the heart. Chambers: LA left atrium, LV left ventricle, RA right atrium, RV right ventricle. Vessels: Ao aorta, PA pulmonary artery, SVC superior vena cava, IVC inferior vena cava, Pv pulmonary veins. Valves: TV tricuspid valve, AV aortic valve, PV pulmonary valve, MV mitral valve [36].

from the artery to the ventricle. The aortic valve and the pulmonary valve are semilunar valves which do not require muscular support since the three cusps support each other when the valves are closed; the significant contact surface is called the coaptation zone. Moreover they have smooth ventricular and wavy arterial faces. The free edge is indented, with the Arantius nodule for the aortic valve and the Morgagni nodule for the pulmonary valve, characterised by a high concentration of collage fibres in its thicker middle part. All the cardiac valves are sheets of connective tissue covered by an endothelium and are composed of intramural cells (smooth muscle cells, fibroblasts and myofibroblasts), reinforced by collagen and elastic bundles. No valves are located between the atria and the corresponding terminal veins, thus it is difficult to distinguish where the veins end and the atria begin [36, 72]. In Figure 1.2 a sketch of the anatomy of the heart is reported. The heartbeat is a two stages pumping action over a period of about $0.8\ s$. The heart, in order to pump the blood in the circulatory system through the aorta and the pulmonary artery, needs to exceed the resistance in the arteries where the blood has a non-null pressure, due to the reaction of the elastic vessel wall to the deformation induced by the blood inside. The **cardiac cycle** is defined as a sequence of alternating contraction and relaxation of atria and ventricles in order to pump blood throughout the body. Each cardiac cycle has

a sistolic phase, in which the myocardium contracts and the blood is ejected from the ventricle, and a diastolic phase, the period when the myocardium is relaxing. At rest diastole occupies approximately two thirds of the cardiac period. Considering as starting point of the cardiac cycle the time instant in which the ventricles have just ejected the blood and the pulmonary and aortic valves are closed, the cardiac phases are the following:

- isovolumetric relaxation: no changes in the ventricular volume and fast decrease of the ventricular pressure;

- relaxation period: the pressure drops below the atrial one, the atrioventricular valves open and the blood starts to flow into the ventricles. All four chambers are in diastole;

- atrial systole: the atria spontaneously contract and the ventricular filling ends;

- isovolumetric contraction: the ventricles pressure becomes higher than the atrial pressure, a retrograde flow is generated, causing the closure of the atrioventricular valve leaflets. No changes in the ventricular volume and fast increase of the ventricular pressure;

- ventricular systole: when the left/right ventricle pressure becomes higher than the aortic/pulmonary trunk one, the aortic/pulmonary valve opens and the blood flows into the aorta/pulmonary artery.

Afterwards the inversion of the sign of the pressure gradient occurs and the blood decelerates, until the velocity is negative and the semilunar valves close and the cardiac cycle restarts [23, 72, 85].

1.2.   Pulmonary circulation

Pulmonary circulation includes the right side of the heart, the pulmonary arteries, the pulmonary veins, the tricuspid and pulmonary valves, the lungs and it ends in the left atrium.
The main pulmonary artery arises from the right ventricular outflow tract and courses posteriorly and superiorly to the left of and posterior to the aorta. Below the aortic arch, it bifurcates into the right and left pulmonary arteries at the level of the carina, as shown in Figure 1.3. The right and left pulmonary arteries divide into two lobar branches each, and subsequently into segmental and sub segmental branches. Segmental and sub segmental pulmonary arteries are named according to the bronchopulmonary segments that they feed [49]. The main pulmonary artery, or pulmonary trunk, is the only artery

arising from the right ventricle that carries non-oxygenated blood into the lungs [62]. In normal subjects, the pulmonary trunk is about 5 cm long and it has a diameter of about 2.70-3 cm [28, 42]; instead, the two pulmonary arteries have a diameter of about 1.70-1.90 cm [21]. The right pulmonary artery is generally a bit longer and larger than the left branch. In healthy patients the pulmonary arteries pressure is 8-20 $mmHg$ at rest. In the right ventricle a normal systolic pressure is 20-30 $mmHg$ and a normal diastolic pressure is 3-7 $mmHg$ [59]. The characteristic velocity of blood through the pulmonary valve is approximately 75 cm/s [47]. Both the pressure and velocity ranges inside the pulmonary circulation are lower than the correspondent ones inside the systemic circulation. Given the diameter of the pulmonary artery D, the mean blood velocity inside it U, and the density and viscosity of blood it is possible to compute the Reynolds number $Re = \rho DU/\mu$, a dimensionless number, that is large in the arteries, accounting for the predominance of inertial effects over viscous effects of the flow [36, 72].

The pulmonary valve is located between the pulmonary trunk and the right ventricle. It is composed of three semilunar, pocket-like cusps (the anterior, right and left leaflet), whose convex outer border is attached to the root of the pulmonary trunk. The free inner border is thickened in the middle to form the nodule on each side of which there is a small, thin crescent-like area (lunula). When the valve closes the nodules and lunulae are pressed together projecting upwards into the lumen of the pulmonary trunk, thus preventing blood from returning into the right ventricle [51, 91].
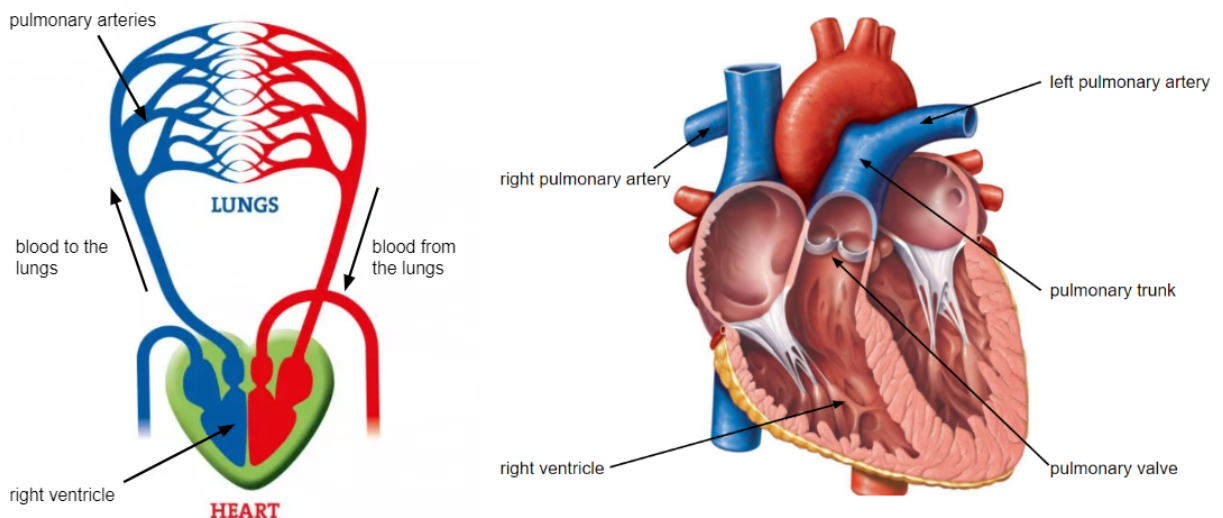

Figure 1.3: Pulmonary circulation (*left*) and schematic representation of the heart with highlighted the right ventricle, the pulmonary artery and the pulmonary valve (*right*).

The cardiac cycle detailed for the right heart is the following one.

- Non-oxygenated blood comes from the superior and inferior venae cavae and passes in the right atrium. When the atrium exceeds the ventricular pressure, the tricuspid valve opens and the blood starts flowing passively in the right ventricle, which relaxes and its volume increases. This is the relaxation period in which both the atrium and the ventricle are in diastole. In this period the first two steps of the diastolic phase of the right ventricle occur: an early rapid filling and a slow filling.

- The right atrium spontaneously contracts. During this period the last part of the diastolic phase of the right ventricle occurs. In Figure 1.4 the atrial contraction is represented by the a-wave on the atrial pressure waveform. The end-diastolic volume (EDV), i.e. the volume of blood within the right ventricle at the end of the atrial contraction, is 100-160 mL in healthy patients.

- After the atrial systole, the ventricular active contraction starts. This produces an increase in the ventricular pressure causing retrograde flow that accordingly closes the tricuspid valve. However, the ventricular pressure is still lower than the pressure inside the pulmonary trunk, so the pulmonary valve is also closed. The volume of the ventricle remains constant, but it undergoes a significant change in its shape as the myocardium continues to contract and the pressure in the ventricle increases rapidly. This phase is the isovolumetric contraction. In Figure 1.4, the c-wave represents the atrial pressure increase as a consequence of the tricuspid valve bulging into the right atrium due to the presence of retrograde flow.

- When the ventricle pressure becomes higher than the pulmonary artery one, the pulmonary valve opens and the blood is ejected into the pulmonary trunk. This is the ventricular systole. Initially, the blood flows through the pulmonary valve rapidly and after 0.15-0.2 s the strength of the contraction wanes.

- As time goes on, the ventricle pressure drops below the pulmonary artery one, the flow changes its direction and the pulmonary valve closes. The end-systolic volume (ESV), i.e. the volume of blood within the ventricle following valve closure, is 50-100 mL in healthy patients. After the closure of the pulmonary valve, the right ventricle relaxes again and the pressure falls below that of the right atrium (isovolumetric relaxation). Afterwards the atrial pressure starts to rise slowly again due to the blood coming from the superior and inferior venae cavae; this corresponds to the v-wave of the atrial pressure waveform in Figure 1.4.

We underline that the pulmonary trunk enters the lungs splitting into the right and the left pulmonary arteries. Here, they become arterioles carrying non-oxygenated blood to the pulmonary alveoli, where the blood releases carbon dioxide and receives the oxygen

introduced with breathing. Successively the pulmonary venules carry the oxygenated blood to the pulmonary veins and finally to the left atrium where the cardiac cycle restarts [23, 57, 72, 85, 90].
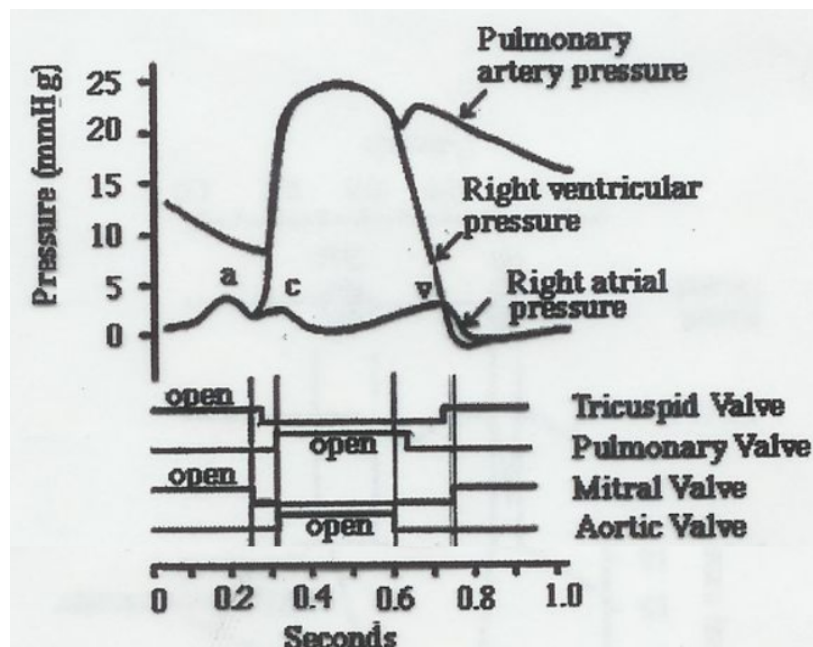
Figure 1.4: Wiggers diagram for the right circulation.

1.3.   Cardiac pathologies

One of the most common pathologies of the pulmonary circulation is the pulmonary hypertension (PAH). It is characterized by an elevated pressure in the pulmonary artery, in mean greater than 25 $mmHg$ at rest or 30 $mmHg$ during exercise [24]. The increase in pressure and pulmonary vascular resistance leads to right ventricle hypertrophy, dilation, and eventual failure and death [20].

Our main focus are the pathologies related to the pulmonary valve. In healthy conditions, as all the other cardiac valves, it has the main task of allowing unidirectional blood flow without causing obstruction or regurgitation or excessive mechanical stress in the cusps and leaflets. Moreover it is responsible for improving the chamber washout, orienting the jets and affecting the coherent vortex structures of the flow, thanks to its shape and motion. Abnormal conditions of the valves, as anatomical defects interesting the leaflets or the subvalvular apparatus, can cause cardiac pathologies [77]. The origins of heart valve pathologies can be classified in two main categories, depending on the age of the patient, they can either be congenital or acquired. In particular, the pulmonary valve can present anatomic variations, for example a different number of cups, or be affected by stenosis or

regurgitation.

The valvular stenosis implies the incomplete opening of the leaflets, because they are thicken, stiffen or fuse together. The presence of a narrower orifice is responsible for the reduced blood flow which can pass over the valve. This causes a pressure overload of the right ventricle, resulting in increased contractility and dilation, and leading to increased wall stress and compensatory right ventricular hypertrophy. Increased muscle mass allows for the right ventricle to maintain a normal cardiac output. Right ventricular hypertrophy may cause a decrease in ventricular compliance and results in increased right ventricular end-diastolic pressures and increased right atrial pressures. Stenosis is primarily a congenital condition; acquired cases can also occur, but are considerably less common. The latter etiologies include infectious endocarditis, carcinoid heart disease, rheumatic heart disease and iatrogenic causes. One of the most common causes of a valve stenosis is the calcification of the valve, where the deposit of calcium on the valve structure causes its stiffening.

The pulmonary valve regurgitation, instead, occurs when the leaflets do not close completely and it results in the leakage of the valve. In this pathologic condition some blood is allowed to stream backward from the pulmonary artery to the ventricle early in diastole. As for the stenosis, it can have primary and secondary causes. Primary causes have considerable overlap with etiologies of stenosis, including iatrogenic regurgitation, congenital anomalies, infectious endocarditis, rheumatic disease and carcinoid heart disease. While iatrogenic pulmonary stenosis itself is not a very common condition, iatrogenic pulmonary regurgitation is the most common cause of severe regurgitation. Secondary causes are the result of pulmonary arterial dilation, either idiopathic or resulting from pulmonary arterial hypertension in patients who have morphologically normal valves.

Both pathologies, if untreated, can lead to heart failure and death of the patient. Usually the solution is valve replacement or surgical repair [30, 74].

Finally the pulmonary valve can be affected by or involved in anomalies and syndromes [91]. An example of congenital anomaly is the tetralogy of Fallot.

1.3.1.   Tetralogy of Fallot

Tetralogy of Fallot is the most common form of cyanotic congenital heart disease.

It was first described by the Danish anatomist and naturalist Niels Stenson in 1671, although its precise anatomical description was elegantly illustrated by William Hunter at St. Georges Hospital Medical School in London in 1784: "...the passage from the right ventricle into the pulmonary artery, which should have admitted a finger, was not so wide as a goose quill; and there was a hole in the partition of the two ventricles, large enough

The normal heart

Tetralogy of Fallot

Aorta

Pulmonary valve

Narrowing beneath
pulmonary valve

Narrowed pulmonary valve

Ventricular septal defect

Left ventricle
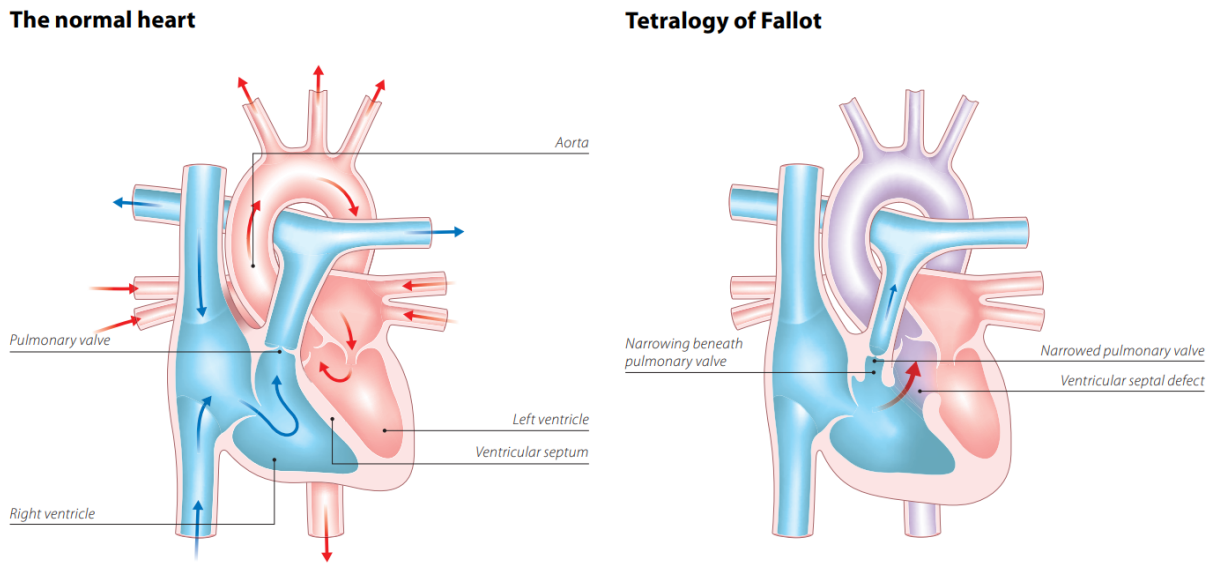
Ventricular septum

Right ventricle

Figure 1.5: Comparison between normal heart and heart with tetralogy of Fallot [1].

to pass the thumb from one to the other. The greatest part of the blood in the right
ventricle was driven with that of the left ventricle into the aorta, or great artery, and
so lost all the advantage which it ought to have had from breathing" (Figure 1.5). His
description was refined by Étienne-Louis Fallot in 1888 in *L'anatomie pathologique de la
maladie bleue*, referring to a tetrad of ventricular septal defect (VSD), obstruction of the
right ventricular outflow tract, override of the ventricular septum by the aortic root, and
right ventricular hypertrophy (Figure 1.6) [13, 15]. Then the term tetralogy of Fallot
was used by Canadian Maude Abbott in 1924 in his *Atlas of Congenital Cardiac Disease*
[64]. Similar to many complex congenital heart diseases, tetralogy of Fallot is frequently
diagnosed during fetal life [13]. About 3.5% of all infants born with a congenital heart
disease have tetralogy of Fallot, corresponding to 3 of every 10.000 live births, with males
and females being affected equally [13, 15]. The aetiology is multifactorial, but reported
associations include untreated maternal diabetes, phenylketonuria, and intake of retinoic
acid. Associated chromosomal anomalies can include trisomies 21, 18, and 13, but recent
experience points to the much more frequent association of microdeletions of chromosome
22. The risk of recurrence in families is 3% [15]. Although an experienced paediatri-
cian or cardiologist usually suspects the diagnosis clinically, transthoracic cross-sectional
echocardiography provides a comprehensive description of the intracardiac anatomy [13].
Since the first procedures in the 1950s, advances in the diagnosis, perioperative and sur-
gical treatment, and postoperative care have been such that almost all those born with
tetralogy of Fallot can now expect to survive to adulthood. Since the first reported in-
tracardiac repair of tetralogy in 1955, the age of patients receiving primary corrective
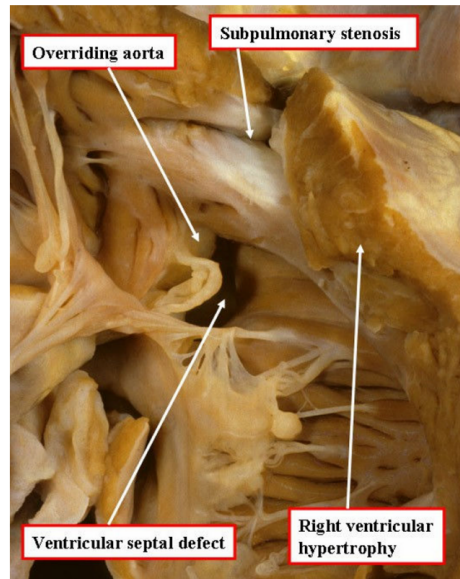
Figure 1.6: Cardinal features of tetralogy of Fallot [15].

surgery has gradually decreased [13]. Some centres prefer to perform complete repairs in all neonates, while others palliate symptomatic neonates, and perform a complete repair in all patients at the age of 4 to 6 months. Palliation, which frequently does not require cardiopulmonary bypass, establishes a secure source of flow of blood to the lungs by construction of a systemic-to-pulmonary arterial shunt, balloon dilation, or placement of a stent in the right ventricular outflow. The most common type of aortopulmonary shunt is known as the modified Blalock-Taussig shunt. This consists of a communication between a subclavian and pulmonary artery on the same side. A complete repair, always performed under cardiopulmonary bypass, consists of closing the interventricular communication with a patch channeling the left ventricle to the aortic root, relief of the subpulmonary obstruction, and reconstruction, if necessary, of the pulmonary arteries [13, 15].

Studies of immediate and long-term follow-up in tetralogy of Fallot reveal excellent outcomes. Chronic issues that face the current population of adults subsequent to their surgical repair include the hemodynamic manifestations of chronic pulmonary regurgitation, recurrent or residual pulmonary stenosis, and ventricular arhythmias. As for all patients with congenitally malformed hearts, the management of the patient with tetralogy of Fallot does not end at the time of complete repair. Follow-up by cardiologists trained in congenital cardiac disease will remain a lifelong experience [15].

One possible treatment is the Ross procedure first, in pediatric age range, and then the implant of a prosthetic valve.

1.3.2.   Ross procedure

The Ross procedure is a cardiac surgery procedure in which the diseased aortic valve, in our case due to aortic overriding, is replaced with the patient's own pulmonary valve (autograft valve) and a right ventricle (RV) to pulmonary artery conduit is placed in the pulmonary position [58, 65]. Aortic valve replacement in children is associated with distinct clinical and technical problems. Those problems are especially common in the smallest children owing to the lack of suitable small size prostheses and subsequent early and late problems related to compression of adjacent cardiac structures by the relatively large prosthesis, rapid prosthesis degeneration, lack of growth and poor compliance with anticoagulation regimen. There is no ideal valve substitute and all options are associated with major limitations; the Ross procedure is no exception [11]. This has the advantages of neo-aortic (autograft) valve growth and avoidance of anticoagulation [65]. After the operation the patient is left in a condition of severe pulmonary insufficiency. A donated human pulmonary valve (pulmonary homograft/allograft) or a prosthetic valve is used to replace the pulmonary valve [4].

1.3.3.   Prosthetic valve implant

In order to be successful, the prosthetic valve must mimic the static and dynamic characteristics of the natural human valve and the mechanics of flow through it. It should not produce turbulence, flow stagnation or excessive shear stress, which can cause haemolysis, i.e. the damaging of blood cells [36].
The No-React® Injectable BioPulmonic Prosthesis (Bio Integral Surgical, Inc., Mississauga, ON, Canada) combines a minimalized invasive procedure with the advantages of surgical pulmonary valve replacement. It is a xenograft prosthetic valve consisting of a porcine PV covered with a No-React®-treated bovine pericardium sleeve and mounted on a self-expandable Nitinol stent, a tube-like medical device. Stent hooks lock the device by grasping the surrounding pulmonary trunk tissue (Figure 1.7). Both the porcine valve and the pericardium are affixed with glutaraldehyde and then detoxified with a proprietary process called No-React®, which eliminates any free residual aldehyde from surfaces [40]. Xenografts have the advantage that they are biological material, but they must be treated so that they are not rejected by the immune system and this treatment limits their lifetime [36]. The diameter of the prosthesis ranges from 15 to 31 mm. The device is fully MRI-compatible. It has the European Conformity mark certification so it can be freely implanted in Europe. It has not been approved by the US Food and Drug Administration so it can be implanted in patients in the USA only for compassionate use

Figure 1.7: No-React® Injectable BioPulmonic valve prosthesis [40].

or in authorized clinical trials. An injectable valve prosthesis can be implanted both with a beating heart and on cardiopulmonary bypass. The surgical procedure is performed through a median sternotomy in all patients [40].

1.4.   Computational hemodynamics

Cardiovascular diseases represent more than 30% of all global deaths [55]. The increasing impact of cardiovascular diseases in our lives is the driving motivation of the remarkable interest from both the mathematical and bioengineering communities over the past 25 years [72].

Computational hemodynamics represent a powerful tool for gaining insight into cardiovascular disease progression, providing essential metrics of blood flow that are otherwise immeasurable. Both in academic research and in clinical settings, virtual simulations of the cardiovascular system have applications to treatment and surgical planning since they can be used to rapidly assess complex multivariable interactions between blood vessels, blood flow, and the heart [52]. Their non-invasiveness has become a major requisite, because it allows to investigate on physiological and pathological real cases, and to follow the temporal evolution of the vascular pathology.

The study of blood dynamics with a rigorous mathematical approach starts to increase in the early 90s thanks to the development of the high-resolution imaging systems (computed tomography, magnetic resonance and angiographic techniques) which allowed the visualization of blood vessels in a non invasive way. Moreover, using the image segmentation process it became possible also to reconstruct accurate patient-specific 3D geometry models of blood vessels from clinical images [36].

Papers about pulmonary circulation are very few in literature with respect to the sys-

temic one, making the hemodynamics in the pulmonary vasculature largely unexplored [52]. The importance of the pulmonary circulation is largely increased in the last years, since it is the respiratory system itself to be mainly attacked by the coronavirus COVID19 disease. Anyway the pulmonary vasculature is susceptible to a wide range of pathologies, that directly impact and are affected by the hemodynamics, as anticipated in Section 1.3, and consequently the ability to develop numerical models of pulmonary blood flow can be inestimable to the clinical scientist. In particular, the pulmonary valve plays a crucial role. Due to its importance, a computational model aiming at reproducing and analyzing cardiac hemodynamics requires to include valves geometry and dynamics.

1.5. Fluid-valve interaction: State of the art

Both the geometry and the dynamics of the cardiac valves have to be included in a computational model with the aim of accurately describe the cardiac hemodynamics, as already discussed in Section 1.4. In literature many methods and approaches have been proposed to model the fluid-structure interaction (FSI) between the blood flow and the valve dynamics. Here we report the most important ones, by discussing them in a decreasing order with respect to the dimension of the valve problem, while the blood has always a 3D description.

1.5.1. 3D-3D models

One of the possible techniques to face the FSI problem is the Arbitrary Lagrangian Eulerian (ALE). The **ALE formulation** is the most common boundary-conforming method: the computational mesh is deformed dynamically to always conform to the boundaries of the computational domain. It can be used both with structured and unstructured grids but its usefulness is limited to problems with relatively simple geometries and moderate deformations, since it may require a frequent remeshing of the domain to deal with large mesh deformation and topology changes. In the fluid-structure problem arising between blood and heart valve leaflets, this approach is not much used, since, due to the large displacements of the leaflets, the fluid mesh becomes highly distorted, producing severely stretched mesh elements and thus requiring a frequent remeshing of the grid [31, 72, 88]. An example of application of the ALE formulation can be found in [32].

More suited techniques in the context of valve-fluid interaction are the **immersed boundary** and **fictitious domain** methods. They are non boundary- conforming methods: there is no need for the grid to conform to moving boundaries and as such are inherently applicable to cardiovascular flow problems. Moreover they both belong to the category

of diffused-interface methods. In both immersed boundary and fictitious domain methods the leaflets are represented in a Lagrangian framework regarded as part of the fluid, represented in an Eulerian framework, and exerting internal localized forces on the latter [72]. In other words, the fluid is discretized in a fixed computational domain, while the valve structure is discretized in a separate body-fitted mesh with the coupling accounted either explicitly or implicitly by adding suitable forces at the fluid/solid interface [31]. In particular, in the immersed boundary method, proposed by Peskin [68], the appropriate forces are explicitly added to the fluid equation and distributed over all nodes of the fluid mesh through a smoothed Dirac delta function. An evolution of this method, that is no longer first order, but it is formally second-order accurate and combines adaptive mesh refinement to increase resolution in the vicinity of immersed boundaries has also proposed by Griffith *et al.* [44]. In the fictious domain method the coupling between the fluid and the solid problem is made through Lagrange multipliers. An example of application of this method can be found in [45]. A major limitation of diffused-interface methods is the computational cost associated with carrying out simulations at physiologic Reynolds numbers due to the large numbers of grid nodes required to accurately resolve the wall shear stress on diffused immersed boundaries [87]. For that reason such methods are more recently used in conjunction with local mesh refinement, see e.g. [44].

To remedy the difficulties inherent with diffused interface methods, a class of sharp-interface immersed boundary methods, which treat the immersed boundary as a sharp interface, still belonging to the non-boundary conforming methods, has been developed [88]. In the so-called **cut-cell** methods [86] the shape of grid cells in the vicinity of the boundary is modified to produce a locally boundary-fitted mesh. The Cut-FEM approach allows to handle an internal interface cutting the mesh in an arbitrary way and writing two weak formulations of the problem at hand, one for each of the two subdomains generated by the presence of the interface, and then sum them up. In this case, the meshes of the two subdomains are fixed. For the mesh elements that are cut by the interface, their contribution is split into two parts and the jump between the normal stresses at the interface is determined by the physical interaction with the interface, as happens for the blood/valve interaction. To guarantee the satisfaction of the interface continuity conditions, a common choice is the discontinuous Galerkin (DG) mortaring, which prescribes interface conditions in a weak sense, thus allowing a great degree of flexibility of the solution at the interface. Since the cut elements can be polygonal elements, the Extended Finite Element method (X-FEM) is commonly used: the Finite Element space is suitably enriched in order to make the treatment of the cut elements easy, duplicating the variables in the cut elements and using the basis functions of the original triangle in both subdomains, to represent the Finite Element solution and to compute the integrals [72].

Examples of applications can be found in found in [10, 94]. An alternative sharp-interface formulation readily applicable to arbitrarily complex flow domains is the **curvilinear immersed boundary** developed in [41]. This method is a hybrid formulation, integrating structured curvilinear boundary fitted grids with the sharp-interface immersed boundary methodology.

All of these aforementioned methods require a full 3D representation of the valve geometry and of its mechanics solver. Thus they require a high computational cost. For these reasons, full 3D FSI models are nowadays mostly restricted to study valves in simplified configurations.

1.5.2.   3D-2D models

In FSI simulations of biological tissues, such as heart valve leaflet interaction with blood flow, it is crucial to use a relevant and efficient structural model that is able to realistically represent the deformation of the tissue under loads imposed by the pulsatile blood flow. Biological tissues of leaflets are normally thin and they exhibit significant bending. Therefore, to study the cardiac valves, it is possible to use the Koiter's shell model [53], which is a well known two-dimensional model for elastic shells. Example of applications to the tricuspid valve and the pulmonary valve can be found in [80] and [81] respectively.

1.5.3.   3D-0D models

In order to provide reliable information on the valve dynamics with reduced computational cost, without neglecting its interaction with the blood flow, lumped-parameter models have been introduced.

These models can be grouped into two main categories. In the first one, which includes the majority of works, the valve hemodynamic effects are represented by means of a phenomenological relationship between the pressure jump across the leaflets and the flow rate passing through them [19, 56]. The single parameters appearing in the equations do not have a precisely quantifiable physical meaning and consequently the model becomes highly dependent on the specific application of interest. In the second one, instead, the reduced model is derived from a momentum balance at the leaflets; the inertia and stiffness of the leaflets can be neglected, as in [27], or considered, e.g. in a linear ordinary differential equation, as in [78]. In the first paper the geometry of the mitral valve is described by a one degree of freedom, parametric model. The flow-valve interaction is expressed in integral terms based on the conservation of mass without the need of defining the material characteristic of the valve tissue. The difference between the densities of blood and

tissue is assumed negligible since the basic idea is that the mitral valve motion is almost completely driven by the blood dynamics. The second paper, instead, has the aim of studying the flow physics of transvalvular flows in the aorta, both with a normal and a abnormal valve. The valve model employed is based on the prescribed mode shape of the movement of the leaflets, but the dynamics of the leaflets is determined by the equation of motion with the integrated hemodynamic force on the leaflets as well as the inertia and the stiffness parameters. By prescribing the mode shape, the degree of freedom can be reduced and the equation of motion is reduced to an ordinary differential equation, and this enables the efficient FSI simulations of the transvalvular flows, while the status of leaflet can be controlled with the model parameters (inertia and stiffness).

Fedele *et al.* [31] proposed a reduced fully coupled 3D-0D FSI model for the interactions between the fluid and the aortic valve leaflets, belonging to the first category. Blood dynamics is described by incompressible Navier-Stokes equations, and the hemodynamics effect of the valve's kinematics are accounted for by the Resistive Immersed Implicit Surface method (RIIS), by adding a penalty term to the fluid momentum equation. It is based on the Resistive Immersed Surface (RIS) method, that lays in the immersed boundary/fictitious domain framework and it is characterized by a fundamentally negligible computational overhead in computational fluid dynamics (CFD) simulations. The dynamics of the valve between its closed and open position is modeled using the 0D model proposed by Korakianitis and Shi [56] based on a second-order ordinary differential equation (ODE) with the leaflets angle as the unique, dependent variable. The valve opening angle depends on the pressure jump and the flow rate across the valve.

Another lumped-parameter structure model for the aortic valve, coupled with a Navier-Stokes-RIIS fluid dynamics, that instead belongs to the second category, is proposed in the work of work of Fumagalli *et al.* [39]. The aim of this work is to enrich the description of the valve dynamics while preserving a low computational effort, lower than the one of fully 3D FSI systems. In this case the model for the dynamics of the valve is derived from the balance of forces at the leaflet, which relates the elasticity of the leaflets to its curvature. This approach allows to automatically account for the specific valve geometry and to relate it directly with the flow-induced forces to which the leaflets are subject. Based on this mechanical model, a reduced 3D-0D fluid-structure interaction (FSI) system is introduced, modeling the interplay between the 3D blood flow in the aorta and the aortic valve dynamics.

1.5.4.   3D-image-based models

Computational hemodynamics based on dynamic medical images, which provide the vessel or myocardial displacement, represents an effective tool to provide quantitative insights about cardiovascular diseases and useful indications to design clinical practices. This is true mainly for the reconstructions of the motion of vessels and ventricles, but also for the reconstruction of the cardiac valve kinematics. For example in [38] the motion of the mitral leaflets is reconstructed from cine magnetic resonance imaging (cine-MRI) data. This strategy allows to reduce the computational effort, avoiding the complex structure of the mitral valve including the subvalvular apparatus, and the demanding calibration of the valve rheological properties. In this work the presence of the mitral valve in the fluid problem is accounted for by the Resistive Immersed Implicit Surface (RIIS) method, already discussed in the previous section (Section 1.5.3).

1.6.   State of the art of computational studies for the right circulation

As already mentioned in Section 1.4, the pulmonary circulation is scarcely studied, in particular with respect to the systemic one.

Most works about the hemodynamics in the pulmonary artery concern pathological conditions, in particular the pulmonary hypertension. In [52] the authors provide a clinical overview of pulmonary hypertension with a focus on the hemodynamics, current treatments, and their limitations. Moreover they present a review of the tasks involved in developing a computational model of pulmonary blood flow, namely vasculature reconstruction, meshing, and boundary conditions. In [92] the pulmonary arterial hypertension is detected by vascular wall stiffness and hemodynamic parameters that represent potential biomechanical markers. In [89] the authors provide a comparison with respect to the normal pulmonary blood flow, in terms of local hemodynamics, especially wall shear stress, energy loss and streamlines. Another comparison between the PAH and the healthy case in terms of velocity and wall shear stress can be found in [84].

On the other hand some papers consider phisiological conditions. For example in [60] a computational fluid-structure interaction study for a healthy patient-specific pulmonary arterial tree is presented, using the unified continuum and variational multiscale formulation. In [55], instead, a highly parallel algorithm is developed and studied for solving a monolithically coupled fluid-structure system for the modeling of the interaction of the blood flow and the arterial wall. Another parallel algorithm, scalable and based on domain decomposition methods, is examined in [54] to investigate an unsteady model with

patient-specific pulsatile waveforms as the inlet boundary condition. Instead in [83] the three-dimensional hemodynamics in the human pulmonary arteries is analyzed, in particular comparing resting and exercise conditions.

Also for what concerns the pulmonary valve, as it happens for the pulmonary artery, in literature we can find papers concerning both valve defects and physiological behavior. In [29], for example, an approach for optimal leaflet shape design based on Finite Element simulation of a mechanically anisotropic, elastomeric scaffold for pulmonary valve replacement is proposed. In [76] the authors provide a description of the anatomy of the pulmonary valve and related structures at CT and MR imaging and some imaging examples of pathologic findings in different diseases, such as pulmonary regurgitation. Another work which focuses on the imaging is [43], in which a complete and modular patient-specifc valve model based on 4D cardiac computed tomography data is discussed. In [79], instead, a geometrical model of the pulmonary valve in its fully open position, according to its structure and physiological features, is presented.

1.7.   Aims of the work

The goal of this work is to apply for the first time the reduced 3D-0D fluid-structure interaction model proposed in Fumagalli *et al.* [39], for the aortic valve, to the pulmonary valve. This thesis is innovative since a 3D-0D model has not been applied to the right heart yet. The model has to be properly calibrated, since, considering the pulmonary circulation instead of the systemic one, not only the pressure and velocity ranges but also the geometry of the artery and of the valve are different. We are interested in analyzing if the FSI model, after the calibration, well represents the physiological behavior of both the blood inside the pulmonary artery and the pulmonary valve or if some further assumptions are needed.

The work consists of two main steps.

- The first step is to arrange the 3D model of the pulmonary artery, already reconstructed in a previous work [69], for the numerical simulations and to position the pulmonary valve. The reconstruction procedures have been performed starting from the data and the tomographic images of two patients with the pulmonary prosthetic valve, provided by the Division of Cardiovascular Surgery of the Department of Cardiology of Niguarda Hospital, Milan. The pulmonary valve is not reconstructed from the computed tomography (CT), but a generic model of the valve, in this case the one provided by Zygote [9], is adapted to each patient specific geometry, both in its open and closed configuration. This valve positioning procedure is a very challenging

and important aspect in numerical models for cardiac valves, since the geometrical configuration of the valve greatly influences the hemodynamics. The choice of the Zygote valve model is dictated by the fact that the cardiac valve reconstruction from the CT is usually demanding since the low resolution of the tomographic data makes the leaflets not detectable.

- The second step is devoted to the calibration of the model and to the numerical simulations, performed in order to characterize the hemodynamics inside the pulmonary artery, by analyzing the meaningful quantities.

Both steps are performed for each patient.

The thesis is organized as follows.

After the first introductory chapter, the second chapter concerns the description of the mathematical and numerical models. In particular the blood flow is modeled by the Navier Stokes equations with the addition of a resistive penalty term which takes into account the presence of the immersed valve, while the dynamics of the valve is described by a lumped-parameters model. The resulting reduced fluid-structure interaction problem has a computational cost that is comparable with the solution of a prescribed-motion fluid dynamics problem. A stabilized Finite Element method with a BDF (backward differentiation formula) time scheme is adopted for the discretization of the coupled problem. For what concerns the boundary conditions they are derived from the 0D model of the whole cardiovascular system. This model will be additionally the object of a sensitivity analysis.

The third chapter is dedicated to all the steps that are needed to set up the computational domain, both the artery and the valve.

Finally the fourth chapter contains the calibration of the model, the numerical simulations and the post-processing of the results.

2 | Mathematical models and numerical methods

In this chapter we introduce the reduced model representing the fluid-structure interaction between the blood flow in the pulmonary artery and the pulmonary valve leaflets.

After having provided in Section 2.1 a description of the blood modeling, in Section 2.2 we discuss the fluid dynamics model, with the valve effects modeled by a resistive method. Then, the reduced structure model for the valve dynamics is derived in Section 2.3, and the FSI coupling is detailed in Section 2.4. Finally Section 2.5 is devoted to the numerical approximation of the fully coupled model.

At the end of the chapter, in Section 2.6, we provide a description of the lumped-parameters model of the whole cardiovascular system, from which we extract the boundary conditions for the fluid problem.

2.1. Blood modeling

Blood is composed of plasma (about 55% of its total volume) and living cells.

The plasma contains $\simeq 92\%$ water with the rest being made up of proteins, small molecules and ions. The diameter of blood cells is approximately 10^{-3} cm, whereas that of the smallest arteries and veins is about 10^{-1} cm.

Thus, blood is commonly modeled as an homogeneous, incompressible fluid, with uniform density $\rho = 1.06 \cdot 10^3$ kg/m^3 and dynamic viscosity $\mu = 3.5 \cdot 10^{-3}$ $Pa \cdot s$. Moreover, in the systemic and pulmonary circulations, it is typically considered Newtonian, i.e. characterized by a linear relationship between internal forces and velocity gradients [35, 67]. In the smallest arteries, such as coronary arteries or in the presence of vessel narrowing (stenosis), instead, non-Newtonian blood rheology is more appropriate [25].

The Cauchy stress tensor for a Newtonian, incompressible and viscous fluid is

$$\boldsymbol{\sigma}(\mathbf{u}, p) = -p\mathbf{I} + 2\mu\mathbf{D}(\mathbf{u}) = -p\mathbf{I} + \mu(\nabla\mathbf{u} + (\nabla\mathbf{u})^T), \qquad (2.1)$$

where $\mathbf{D}(\mathbf{u})$ is the strain rate tensor, p and $\mathbf{u}$ are the pressure and the velocity of the fluid, respectively.

2.2. Fluid model and Resistive Immersed Implicit Surface method

The interaction of the valve dynamics with the fluid dynamics is accounted for by the Resistive Immersed Implicit Surface (RIIS) method. It is inspired by the Resistive Immersed Surface (RIS) approach, originally proposed in Fernández *et al.* [33] to study a porous interface immersed in a fluid, and lately extended in Astorino *et al.* [14] to model the aortic valve. It was successively employed in [38] in a clinical context for the mitral valve. In this method the presence of the valve is taken into account in the momentum equation of the Navier–Stokes system by adding a localized penalty term, specifically a resistive term, which weakly enforces the blood to adhere to the leaflets.
The fluid model is solved in an Eulerian formulation and in a fixed domain $\Omega \subset \mathbb{R}^3$. The movement of the leaflets does not modify the computational mesh since the computational mesh and the surface do not need to be conforming.

More in detail, the approach consists in representing the geometry of the moving valve Γ_t, in our case the pulmonary valve, as a surface immersed in the fluid domain Ω, for us the pulmonary artery (Figure 2.1). It is implicitly described at each time t by a level-set function $\varphi_t : \Omega \to \mathbb{R}$ [63], as

$$\Gamma_t = \{\mathbf{x} \in \Omega : \varphi_t(\mathbf{x}) = \mathbf{0}\}. \tag{2.2}$$

The function φ_t is assumed to be a signed distance function, i.e. it fulfills $|\nabla \varphi_t| = 1$, for any t.
The velocity $\mathbf{u}$ and pressure p of the blood satisfy the following formulation of the Navier-Stokes equations:

$$
\begin{cases}
\rho\partial_t\mathbf{u} + \rho(\mathbf{u}\cdot\nabla)\mathbf{u} - \nabla\cdot\boldsymbol{\sigma}(\mathbf{u},p) + \frac{R}{\epsilon}(\mathbf{u}-\mathbf{u}_\Gamma)\delta_{\Gamma,\epsilon} = \mathbf{0} & \text{in } \Omega,\ t\in(0,T], \\
\nabla\cdot\mathbf{u} = 0 & \text{in } \Omega,\ t\in(0,T], \\
\mathbf{u} = \mathbf{0} & \text{on } \Sigma_{wall},\ t\in(0,T], \\
\boldsymbol{\sigma}(\mathbf{u},p)\mathbf{n} = p_{in}\mathbf{n} & \text{on } \Sigma_{in},\ t\in(0,T], \\
\boldsymbol{\sigma}(\mathbf{u},p)\mathbf{n} = p_{out}\mathbf{n} & \text{on } \Sigma_{out},\ t\in(0,T], \\
\mathbf{u} = \mathbf{0} & \text{in } \Omega,\ t=0,
\end{cases}
\tag{2.3}
$$

where $\mathbf{u}_\Gamma$ is the velocity of the valve, which constitutes a datum for the fluid problem. The resistive penalty coefficient, added into the Navier-Stokes equations, is defined as the ratio between the resistance coefficient R and the half-thickness ϵ of the leaflets, and the resistive term enforces condition $\mathbf{u} = \mathbf{u}_\Gamma$ as $\epsilon \to 0$. Indeed, in that case $\frac{R}{\epsilon} \to \infty$, which forces $\mathbf{u}$ to be equal to the valve velocity. We underline that this method can be interpreted as a weak imposition of a no-slip condition on the immersed surface.

The resistive term has support in a narrow layer around Γ_t, represented by a smeared Dirac delta function $\delta_{\Gamma,\epsilon} : \Omega \to [0,+\infty)$ that approximates the Dirac distribution (rigorously, the codimension-1 Hausdorff measure), as follows:

$$
\delta_{\Gamma,\epsilon}(\mathbf{x}) = \begin{cases}
\dfrac{1 + \cos(\pi\varphi_t(\mathbf{x})/\epsilon)}{2\epsilon} & \text{if } |\varphi_t(\mathbf{x})| \le \epsilon, \\
0 & \text{if } |\varphi_t(\mathbf{x})| > \epsilon,
\end{cases}
\tag{2.4}
$$

where the half-thickness ϵ is the smoothing parameter.

In general, the reconstruction of $\mathbf{u}_\Gamma$ may be complex, possibly entailing numerical instabilities [31]. The prescribed leaflet velocity $\mathbf{u}_\Gamma$ may be provided in different ways, for example as the solution to an additional structural problem for the leaflets as in our case, by a reconstruction procedure based on clinical data or adopting a quasi-static approach, that is setting $\mathbf{u}_\Gamma = \mathbf{0}$. The computational costs are lower in the quasi-static approach and are higher if the valve velocity is reconstructed through an additional problem.

With regard to the boundary conditions, p_{in} and p_{out} are the pressure values imposed at the inflow and outflow boundaries Σ_{in} and Σ_{out}, respectively, while the boundary Σ_{wall} represents the artery wall. More in detail, Σ_{in} is the inlet of the artery, where the blood enters, ejected from the right ventricle; $\Sigma_{out} = \Sigma_{out}^1 \cup \Sigma_{out}^2$ consists in two outlets, corresponding to the left and right pulmonary artery (Figure 2.1). The pressure values come from a physiological simulation of circulation model, discussed in Section 2.6.
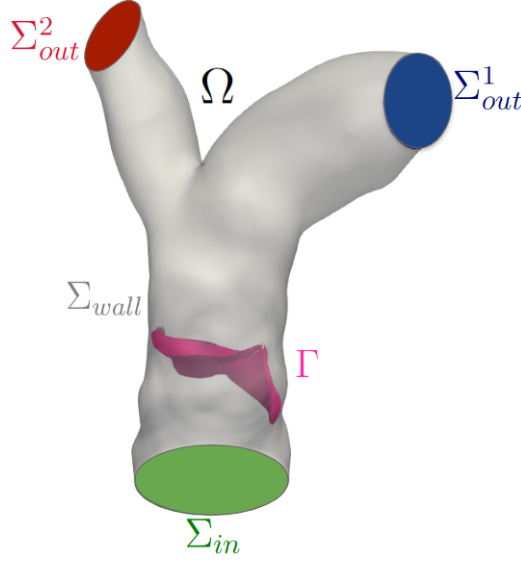
Figure 2.1: Computational domain Ω with its boundaries and the immersed valve Γ.

Starting from the strong formulation of the problem (2.3) and introducing the following functional spaces:

$$V = \{\mathbf{v} \in \left[\mathbf{H}^1(\Omega)\right]^3 : \mathbf{v}|_{\Sigma_{wall}} = \mathbf{0}\},$$
$$Q = L^2(\Omega),$$

we can write the weak formulation.

The idea is to take $\mathbf{v}$ and q as test functions for velocity and pressure respectively, belonging to the two correspondent functional spaces. Afterwards the momentum and continuity equations, respectively the first and the second equation of (2.3), have to be multiplied by the respective test function, integrating over the computational domain Ω and considering the Neumann boundary conditions from the strong formulation.

Taking into account the momentum equation, we multiply it by the test function $\mathbf{v} \in V$ and we integrate over Ω:

$$\int_\Omega \rho \partial_t \mathbf{u} \cdot \mathbf{v} \, d\Omega + \int_\Omega \rho(\mathbf{u} \cdot \nabla)\mathbf{u} \cdot \mathbf{v} \, d\Omega - \int_\Omega \nabla \cdot \boldsymbol{\sigma} \cdot \mathbf{v} \, d\Omega + \int_\Omega \frac{R}{\epsilon}(\mathbf{u} - \mathbf{u}_\Gamma)\delta_{\Gamma,\epsilon} \cdot \mathbf{v} \, d\Omega = \mathbf{0}.$$

If we consider the Cauchy stress tensor divergence integral, exploiting the definition in (2.1) firstly and then integrating by parts we obtain:

$$\int_\Omega \nabla \cdot \boldsymbol{\sigma} \cdot \mathbf{v}\, d\Omega = \int_\Omega -\nabla p \cdot \mathbf{v}\, d\Omega + \int_\Omega \mu \nabla \cdot (\nabla \mathbf{u} + (\nabla \mathbf{u})^T) \cdot \mathbf{v}\, d\Omega =$$

$$= \int_\Omega p \nabla \cdot \mathbf{v}\, d\Omega - \int_{\partial\Omega} p\mathbf{n} \cdot \mathbf{v}\, d\gamma - \int_\Omega \mu(\nabla \mathbf{u} + (\nabla \mathbf{u})^T) : \nabla \mathbf{v}\, d\Omega+ \quad (2.5)$$

$$+ \int_{\partial\Omega} \mu \frac{\partial \mathbf{u}}{\partial \mathbf{n}} \cdot \mathbf{v}\, d\gamma \qquad \forall \mathbf{v} \in V.$$

Relying on the Neumann boundary conditions from the strong formulation in (2.3) and substituting the Cauchy stress tensor divergence integral with the integral sum in (2.5), the weak formulation of the momentum equation is recovered:

$$\int_\Omega \rho \partial_t \mathbf{u} \cdot \mathbf{v}\, d\Omega + \int_\Omega \rho(\mathbf{u} \cdot \nabla)\mathbf{u} \cdot \mathbf{v}\, d\Omega - \int_\Omega p\nabla \cdot \mathbf{v}\, d\Omega + \int_\Omega \mu(\nabla \mathbf{u} + (\nabla \mathbf{u})^T) : \nabla \mathbf{v}\, d\Omega+$$

$$- \int_{\Sigma_{out}} p_{in}\mathbf{n} \cdot \mathbf{v}\, d\gamma - \int_{\Sigma_{out}} p_{out}\mathbf{n} \cdot \mathbf{v}\, d\gamma + \int_\Omega \frac{R}{\epsilon}(\mathbf{u} - \mathbf{u}_\Gamma)\delta_{\Gamma,\epsilon} \cdot \mathbf{v}\, d\Omega = \mathbf{0} \qquad \forall \mathbf{v} \in V.$$

Repeating the procedure for the continuity equation, multiplying for the test function $q \in Q$, the following identity is obtained:

$$\int_\Omega \nabla \cdot \mathbf{u}\, q\, d\Omega = 0 \qquad \forall q \in Q.$$

The weak formulation can be re-written by introducing the following forms and functionals:

$$\widetilde{a}(\mathbf{u}, \mathbf{v}) = a(\mathbf{u}, \mathbf{v}) + r(\mathbf{u}, \mathbf{v}) =$$

$$= \int_\Omega \mu(\nabla \mathbf{u} + (\nabla \mathbf{u})^T) : \nabla \mathbf{v}\, d\Omega + \int_\Omega \frac{R}{\epsilon}\mathbf{u}\delta_{\Gamma,\epsilon} \cdot \mathbf{v}\, d\Omega,$$

$$b(\mathbf{v}, q) = - \int_\Omega \nabla \cdot \mathbf{v}\, q\, d\Omega,$$

$$c(\mathbf{w}, \mathbf{u}, \mathbf{v}) = \int_\Omega \rho(\mathbf{w} \cdot \nabla)\mathbf{u} \cdot \mathbf{v}\, d\Omega,$$

$$F(\mathbf{v}) = \int_{\Sigma_{in}} p_{in}\mathbf{n} \cdot \mathbf{v}d\gamma + \int_{\Sigma_{out}} p_{out}\mathbf{n} \cdot \mathbf{v}d\gamma + \int_\Omega \frac{R}{\epsilon}\mathbf{u}_\Gamma\delta_{\Gamma,\epsilon} \cdot \mathbf{v}\, d\Omega.$$

The weak formulation reads as follows.

Find $\mathbf{u} \in V$ and $p \in Q$ for a.e. $t \in (0, T]$ such that $\forall \mathbf{v} \in V$ and $\forall q \in Q$:

$$\begin{cases} \rho(\partial_t \mathbf{u}, \mathbf{v}) + \widetilde{a}(\mathbf{u}, \mathbf{v}) + c(\mathbf{u}, \mathbf{u}, \mathbf{v}) + b(\mathbf{v}, p) = F(\mathbf{v}) \\ b(\mathbf{u}, q) = 0 \end{cases} \qquad (2.6)$$

where the duality in the first term of the momentum equation identifies an integral over

Ω with the following notation:

$$(\mathbf{u}, \mathbf{v}) = \int_{\Omega} \mathbf{u} \cdot \mathbf{v} \, d\Omega.$$

2.3. Lumped-parameters structure model

Aiming at providing the configuration and the velocity of the valve, represented by $\delta_{\Gamma,\epsilon}$ and $\mathbf{u}_{\Gamma}$ in the fluid problem (2.3), a structural model for the deformation of the surface Γ_t has to be presented.

In this section we provide the derivation of the reduced, lumped-parameters model which is able to describe the main features of cardiac valve dynamics, between its closed and open configurations, in a realistic manner, proposed in [39]. A schematic representation of the leaflet section is provided in Figure 2.2a.

Denoting by $\mathbf{d}_{\Gamma} : [0, T] \times \widehat{\Gamma} \to \mathbb{R}^3$ the displacement of the leaflet with respect to its reference configuration $\Gamma_0 = \widehat{\Gamma}$, we can represent the current configuration Γ_t as

$$\Gamma_t = \{\mathbf{x} \in \mathbb{R}^3 : \mathbf{x} = \mathbf{T}_t(\widehat{\mathbf{x}}) = \widehat{\mathbf{x}} + \mathbf{d}_{\Gamma}(t, \widehat{\mathbf{x}}) \text{ for some } \widehat{\mathbf{x}} \in \widehat{\Gamma}\}.$$

We assume that every point $\mathbf{x} \in \Gamma_t$ of the leaflet is subject, at each time t, both to an external force $\mathbf{f}(t, \mathbf{x})$ due to the surrounding fluid, and to an elastic force, that is related to the leaflet curvature $H(t, \mathbf{x})$. Both these contributions depend on the current configuration of Γ_t described by $\mathbf{d}_{\Gamma}(t, \widehat{\mathbf{x}})$. We assume that the curvature-induced elastic force acts only normally to the surface, as it happens for the free-surface tension. A schematic representation of the forces acting on the leaflet is provided in Figure 2.2b. Moreover we impose this elastic force to vanish on $\widehat{\Gamma}$, since it is generally observed that the resting state of the cardiac valve is its closed configuration. Finally we assume that the valve motion can be affected by some damping effect. In accordance to these assumptions we can formulate a local force balance as follows:

$$\rho_{\Gamma}\ddot{\mathbf{x}} + \beta\rho_{\Gamma}\dot{\mathbf{x}} = \mathbf{f}(t, \mathbf{x}) - \gamma[H(t, \mathbf{x}) - \widehat{H}(\widehat{\mathbf{x}})]\mathbf{n}_{\Gamma}(t, \mathbf{x}), \tag{2.7}$$

where ρ_{Γ} is the surface density of the valve, β is a damping coefficient, γ is an elasticity coefficient, and $\mathbf{n}_{\Gamma}$ is the normal to the surface Γ_t. The function $\widehat{H}(\widehat{\mathbf{x}})$ represents the total curvature of the surface $\widehat{\Gamma}$ in the position $\widehat{\mathbf{x}} = \mathbf{T}_t^{-1}(\mathbf{x})$ corresponding to $\mathbf{x}$. For the sake of simplicity, and in accordance to the common practice for biological tissues, the density valve leaflets can be considered to be the same of the blood. Based on these considerations, we get $\rho_{\Gamma} = 2\epsilon\rho$, where ϵ denotes the semi-thickness of the leaflet, and, by

RIIS representation, we can write the following consistency formula:

$$\int_{\Gamma_t} \rho_\Gamma d\Gamma \simeq \int_\Omega 2\epsilon\rho\delta_{\Gamma,\epsilon}d\Omega = \rho 2\epsilon|\Gamma_t|.$$

We underline that the parameter ρ_Γ can be tuned to different values, without loss of generality, in order to account for different inertial properties of the leaflets. In particular the inertia of the leaflets may be unknown in patient-specific settings or be affected by added-mass effects, see e.g. [22].

(a) Leaflet section and motion

(b) Forces acting on the leaflet
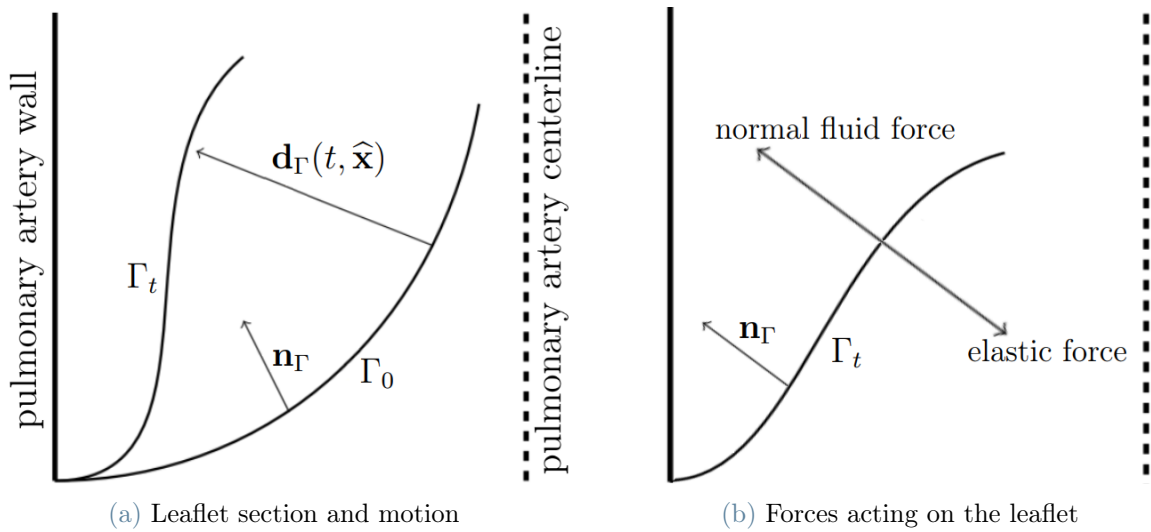
Figure 2.2: Schematic representation of a leaflet section and of the forces acting on it.

In order to reduce equation (2.7) to a 0D model, we assume that $\mathbf{d}_\Gamma$ can be decomposed as

$$\mathbf{d}_\Gamma(t,\widehat{\mathbf{x}}) = c(t)\mathbf{g}(\widehat{\mathbf{x}}), \tag{2.8}$$

where $\mathbf{g} : \widehat{\Gamma} \to \mathbb{R}^3$ is known and takes into account the spatial dependence of the displacement, while $c : [0,T] \to [0,1]$ has to be modeled. In particular, $\mathbf{g}$ represents the valve opening field, and it has to be provided. Indeed it reproduces the displacement of the valve between its closed and open positions, and it depends on the patient-specific model. On the other hand, c represents the valve opening coefficient and expresses the fraction of the valve opening: $c = 0$ corresponds to the valve in closed position, while $c = 1$ denotes the open valve. Moreover, we underline that $c \in [0,1]$, instead of $[-\infty, +\infty]$, since $\mathbf{g}$ is the total displacement from closed to open valve position. Taking into account these extremes, in particular $c = 0$, allows to guarantee a contact effect, at least at kinematic level, even without the presence of a contact force.

Therefore the local balance (2.7) can be re-written as

$$[\ddot{c}(t) + \beta\dot{c}(t)]\rho_\Gamma \mathbf{g}(\mathbf{T}_t^{-1}(\mathbf{x})) = \mathbf{f}(t, \mathbf{x}) - \gamma[H(t, \mathbf{x}) - \widehat{H}(\mathbf{T}_t^{-1}(\mathbf{x}))]\mathbf{n}_\Gamma(t, \mathbf{x}).$$

Taking the component along $\mathbf{n}_\Gamma(t, \mathbf{x})$ and integrating over Γ_t, the following ordinary differential equation for c is obtained:

$$\ddot{c}(t) + \beta\dot{c}(t) = \frac{\int_{\Gamma_t} \mathbf{f}(t, \mathbf{x}) \cdot \mathbf{n}_\Gamma(t, \mathbf{x})d\mathbf{x} - \gamma \int_{\Gamma_t}[H(t, \mathbf{x}) - \widehat{H}(\mathbf{T}_t^{-1}(\mathbf{x}))]d\mathbf{x}}{\int_{\Gamma_t} \rho_\Gamma \mathbf{g}(\mathbf{T}_t^{-1}(\mathbf{x})) \cdot \mathbf{n}_\Gamma(t, \mathbf{x})d\mathbf{x}}, \qquad (2.9)$$

where the dependence of the right hand side on c is implicit in its dependence from the curvature H. Indeed H is defined as $H = -\text{div}\mathbf{n}_\Gamma$ and the normal vector $\mathbf{n}_\Gamma$ can be computed in terms of the derivatives of the function $\mathbf{T}_t(\widehat{\mathbf{x}}) = \widehat{\mathbf{x}} + c(t)\mathbf{g}(\widehat{\mathbf{x}})$. This equation can be completed by proper initial conditions on c and $\dot{c}$, depending on the application of interest, in our case they are both 0, since the we consider the closed, fixed valve as initial configuration.

2.4. Coupling of the fluid and structure models

The 3D fluid model described in Section 2.2 and the 0D valve model introduced in Section 2.3 can be coupled in a reduced FSI model. The fluid-to-valve stress $\mathbf{f}$, appearing in equation (2.9), is computed from the 3D fluid model in terms of $\mathbf{u}$, p and the RIIS-related quantities, while the valve position and velocity are provided by the 0D valve model. We introduce some additional notation related to the representation of the immersed surface Γ_t. Being φ_t a signed distance function, the domain Ω can be partitioned into two regions:

$$\Omega_t^+ = \{\mathbf{x} \in \Omega : \varphi_t(\mathbf{x}) > 0\}, \qquad \Omega_t^- = \{\mathbf{x} \in \Omega : \varphi_t(\mathbf{x}) < 0\}. \qquad (2.10)$$

The definition of φ_t that we employ, as implemented in [8], yields that Γ_t, defined as in (2.2), is a subset of the interface $\overline{\Omega_t^+} \cap \overline{\Omega_t^-}$. Indeed such interface is partitioned into the actual leaflet Γ_t and the surface $(\overline{\Omega_t^+} \cap \overline{\Omega_t^-}) \setminus \Gamma_t$ where φ_t jumps from negative to positive values.

According to (2.10), any function f defined over Ω can be decomposed as $f = f^+ + f^-$, where $f^\pm = f|_{\Omega^\pm}$.

Moreover, the function φ_t allows to define $\widetilde{\mathbf{n}}_\Gamma$ and $\widetilde{H}$, that are the extensions to the whole

domain Ω of the surface normal $\mathbf{n}_\Gamma$ and its curvature H, respectively:

$$\widetilde{\mathbf{n}}_\Gamma = \frac{\nabla\varphi_t}{|\nabla\varphi_t|},$$

$$\widetilde{H} = -\mathrm{div}\widetilde{\mathbf{n}}_\Gamma = -\frac{\Delta\varphi_t}{|\nabla\varphi_t|} + \frac{\nabla^2\varphi_t : (\nabla\varphi_t \otimes \nabla\varphi_t)}{|\nabla\varphi_t|^3}, \tag{2.11}$$

with $\nabla^2\varphi_t$ denoting the Hessian matrix of φ_t. These quantities are actual extensions of the normal vector and curvature, since $\widetilde{\mathbf{n}}_\Gamma|_\Gamma = \mathbf{n}_\Gamma$, $\widetilde{H}|_\Gamma = H$. We remark that $\widetilde{\mathbf{n}}_\Gamma$ is such that it does not change its verse when passing through Γ_t.

We point out that in the definitions (2.11), we did not make the common assumption that $|\nabla\varphi_t| = 1$. Indeed it is not valid near $\partial\Gamma_t$, where φ_t is not continuous, but only in the neighborhood of internal points of Γ_t. We underline that the derivatives appearing in (2.11) are computed in Ω_t^+ and Ω_t^- separately, so that no contribution actually arises from the discontinuity of φ_t.

Moreover, this definition of $\widetilde{\mathbf{n}}_\Gamma$ ensures that the normal has unit magnitude also at the discrete level.

The quantities defined above represent the geometric description of the valve leaflets, we now introduce their kinematics and dynamics. Regarding the RIIS description of the surface, looking at a definition (2.8), the surface velocity can be expressed as

$$\mathbf{u}_\Gamma(t, \mathbf{x}) = \dot{c}(t)\widetilde{\mathbf{g}}(\mathbf{x}), \tag{2.12}$$

where $\widetilde{\mathbf{g}} : \Omega \to \mathbb{R}^3$ is the closest-point extension of $\mathbf{g} : \widehat{\Gamma} \to \mathbb{R}^3$.

The forces exerted by the fluid on the valve are related to the stress jump across Γ_t, thus

$$\mathbf{f} = [\boldsymbol{\sigma}\mathbf{n}_\Gamma]|_{\Gamma_t} = \boldsymbol{\sigma}^+|_{\Gamma_t}\mathbf{n}_\Gamma - \boldsymbol{\sigma}^-|_{\Gamma_t}\mathbf{n}_\Gamma.$$

Considering the surface smearing introduced by the smooth Dirac delta $\delta_{\Gamma,\epsilon}$ and the definitions (2.11), the integral term related to $\mathbf{f}$ that appears in (2.9) can be approximated as follows:

$$\int_{\Gamma_t} \mathbf{f} \cdot \mathbf{n}_\Gamma \simeq \int_\Omega \left(\boldsymbol{\sigma}\widetilde{\mathbf{n}}_\Gamma \cdot \widetilde{\mathbf{n}}_\Gamma \delta_{\Gamma,\epsilon}^+ - \boldsymbol{\sigma}\widetilde{\mathbf{n}}_\Gamma \cdot \widetilde{\mathbf{n}}_\Gamma \delta_{\Gamma,\epsilon}^- \right). \tag{2.13}$$

In analogous way, the other integrals of (2.9) can be approximated as follows:

$$\int_{\Gamma_t} \rho_\Gamma(\mathbf{g} \circ \mathbf{T}_t^{-1}) \cdot \mathbf{n}_\Gamma \simeq \int_\Omega \rho_\Gamma(\mathbf{g} \circ \mathbf{T}_t^{-1}) \cdot \widetilde{\mathbf{n}}_\Gamma \delta_{\Gamma,\epsilon},$$

$$-\gamma \int_{\Gamma_t} \left(H - \widehat{H} \circ \mathbf{T}_t^{-1} \right) \simeq -\gamma \int_\Omega \left(\widetilde{H} - \widehat{\widetilde{H}} \right) \delta_{\Gamma,\epsilon}, \tag{2.14}$$

with $\widehat{\widetilde{H}}$ denoting the RIIS representation of the pulled-back curvature $\widehat{H} \circ \mathbf{T}_t^{-1}$.

We notice that, since $\widetilde{\mathbf{n}}_\Gamma = 1$, if the strain component of the normal stress is assumed to be negligible with respect to the pressure term, the integral force in (2.13) reduces to

$$\int_{\Gamma_t} \mathbf{f} \cdot \mathbf{n}_\Gamma \simeq \int_\Omega \left(p\, \delta_{\Gamma,\epsilon}^+ - p\, \delta_{\Gamma,\epsilon}^- \right),$$

in accordance with other reduced models which are based on the pressure jump across the valve [19, 27, 56, 78].

Summarizing, the coupled problem is the following.

Given p_{in}, p_{out}, $\mathbf{g}$, $\widetilde{\mathbf{g}}$, find $\mathbf{u}$, p, c such that:

fluid problem
$$\begin{cases}
\rho \partial_t \mathbf{u} + \rho (\mathbf{u} \cdot \nabla)\mathbf{u} - \nabla \cdot \boldsymbol{\sigma}(\mathbf{u},p) + \frac{R}{\epsilon}(\mathbf{u} - \mathbf{u}_\Gamma)\delta_{\Gamma,\epsilon} = \mathbf{0} & \text{in } \Omega,\ t \in (0,T], \\
\nabla \cdot \mathbf{u} = 0 & \text{in } \Omega,\ t \in (0,T], \\
\mathbf{u} = \mathbf{0} & \text{on } \Sigma_{wall},\ t \in (0,T], \\
\boldsymbol{\sigma}(\mathbf{u},p)\mathbf{n} = p_{in}\mathbf{n} & \text{on } \Sigma_{in},\ t \in (0,T], \\
\boldsymbol{\sigma}(\mathbf{u},p)\mathbf{n} = p_{out}\mathbf{n} & \text{on } \Sigma_{out},\ t \in (0,T], \\
\mathbf{u} = \mathbf{0} & \text{in } \Omega,\ t = 0,
\end{cases}$$

structure problem
$$\begin{cases}
\ddot{c} + \beta \dot{c} = \dfrac{\int_{\Gamma_t} \mathbf{f} \cdot \mathbf{n}_\Gamma d\mathbf{x} - \gamma \int_{\Gamma_t} [H - \widehat{H}] d\mathbf{x}}{\int_{\Gamma_t} \rho_\Gamma \mathbf{g} \cdot \mathbf{n}_\Gamma d\mathbf{x}} & t \in (0,T], \\
c = 0,\ \dot{c} = 0 & t = 0,
\end{cases}$$

coupling
$$\begin{cases}
\Gamma_t = \widehat{\mathbf{x}} + c\, \mathbf{g}, \qquad \delta_{\Gamma,\epsilon} = F(\Gamma_t), \\
\mathbf{u}_\Gamma = \dot{c}\, \widetilde{\mathbf{g}}, \\
\mathbf{f} = [\boldsymbol{\sigma}(\mathbf{u},p)\mathbf{n}_\Gamma]|_{\Gamma_t} = \boldsymbol{\sigma}^+(\mathbf{u},p)|_{\Gamma_t}\mathbf{n}_\Gamma - \boldsymbol{\sigma}^-(\mathbf{u},p)|_{\Gamma_t}\mathbf{n}_\Gamma.
\end{cases}$$

The dependence of the smeared dirac function $\delta_{\Gamma,\epsilon}$ on the valve position Γ_t is achieved through equations (2.2) and (2.4). Indeed the valve position allows to compute the signed distance function φ_t and consequently $\delta_{\Gamma,\epsilon}$. The computation of φ_t allows to find also the valve curvature H and its normal $\mathbf{n}_\Gamma$, according to equations (2.11) and then restricting on Γ. The approximation of the integrals showing up in the structure problem is reported in equations (2.13), (2.14).

2.5. Numerical approximation

We focus on the numerical approximation of the fully coupled model, reported at the end of Section 2.4 . The fluid model is discretized in space using the stabilized Finite Element

(FE) method, for which the approximated velocity and pressure variables are build from Lagrangian polynomial basis functions of equal degree, and in time by means of backward differentiation formula (BDF) of order 1 and by adopting a semi-implicit treatment for the nonlinear term. The 0D structure problem, instead, is discretized with an explicit scheme.

2.5.1. Fluid model

Time discretization

We introduce a uniform partition of the time interval $[0, T]$ with step-size Δt and nodes $\{t^n\}_{n=0}^N$, where $\Delta t = \frac{T}{N}$. Accordingly, the time-discrete counterparts of all quantities, evaluated at time t^n, will be denoted by a superscript $\cdot^n$. We consider the time discretization by means of backward differentiation formula (BDF) of order 1 and by adopting a semi-implicit treatment for the nonlinear term.

In the following we explain the choice of a semi-implicit formulation, with respect to the advantages and disadvantages of an explicit or implicit one.

An explicit formulation allows the resolution of a linear system reducing the computational cost, but it imposes a restrictive stability condition, $\Delta t \lesssim h^2$, where h is the mesh discretization step. It is a restrictive condition, since in most fluid dynamics applications a refined grid is considered, with a small value of h.

On the other hand a fully implicit formulation generates an unconditionally stable method, but a onerous non-linear system must be solved at every time step.

The choice of a semi-implicit treatment allows to avoid, on one side, the expensive nonlinear system of a fully-implicit treatment, and, on the other side, the restrictive stability condition of an explicit approach. With the semi-implicit approach the non linear term is linearized and the stability condition is of the following type:

$$\Delta t \leq C \frac{h}{||\mathbf{u}^{n-1}||_{L^\infty}},$$

where C is a real constant. This condition is usually already satisfied in hemodynamics for accuracy purposes.

The time discretization of the problem (2.6) reads follows.

We assume known the boundary conditions values and the valve velocity.

Given $\mathbf{u}^0 = \mathbf{0}$, find $\mathbf{u}^n$, p^n for each $n = 1, .., N$ such that:

$$\begin{cases} \left(\rho \dfrac{\mathbf{u}^n - \mathbf{u}^{n-1}}{\Delta t}, \mathbf{v} \right) + \widetilde{a}^n(\mathbf{u}^n, \mathbf{v}) + c(\mathbf{u}^{n-1}, \mathbf{u}^n, \mathbf{v}) + b(\mathbf{v}, p^n) = F^n(\mathbf{v}) \\ b(\mathbf{u}^n, q) = 0 \end{cases}$$

The forms and functional are introduced in Section 2.2.

The dependence of $\widetilde{a}^n$ on n is highlighted with the apex and is due to the term $\delta_{\Gamma,\epsilon}^n$ showing up in the resistive contribution.

Spatial Finite Element discretization

Let $\mathcal{T}h$ be a hexahedral mesh for the domain Ω, such that $\Omega = \bigcup_{T \in \mathcal{T}_h} T$ and the space discretization step is defined as $h = \max\limits_{T \in \mathcal{T}_h} (\text{diam}(T))$. We introduce the Finite Element (FE) space

$$X_h^r = \{ v_h \in C^0(\bar{\Omega}) : v_h|_T \in \mathbb{Q}^r(T), \forall T \in \mathcal{T}_h \},$$

where $\mathbb{Q}^r$ denotes the space of polynomials of degree r with respect to each space coordinate.

The velocity and pressure discrete spaces are thus defined as

$$V_h^r = ([X_h^r]^3 \cap V), \ V_h^r \subset V, \ \dim(V_h^r) = N_h < \infty \ \forall h > 0,$$
$$Q_h^s = X_h^s \cap Q, \ Q_h^s \subset Q, \ \dim(Q_h^s) = M_h < \infty \ \forall h > 0.$$

The fully discretized problem reads as follows.

Given $\mathbf{u}_h^0 = \mathbf{0}$, find $\mathbf{u}_h^n \in V_h^r$, $p_h^n \in Q_h^s$ for each $n = 1, ..., N$ such that $\forall \mathbf{v}_h \in V_h^r$ and $\forall q_h \in Q_h^s$:

$$\left(\rho \frac{\mathbf{u}_h^n - \mathbf{u}_h^{n-1}}{\Delta t}, \mathbf{v}_h \right) + \widetilde{a}^n(\mathbf{u}_h^n, \mathbf{v}_h) + c(\mathbf{u}_h^{n-1}, \mathbf{u}_h^n, \mathbf{v}_h) + b(\mathbf{v}_h, p_h^n) - b(\mathbf{u}_h^n, q_h) = F^n(\mathbf{v}_h).$$

$$(2.15)$$

The continuity and coercivity on V_h^r of the bilinear form $\widetilde{a}(\cdot, \cdot)$ can be proved, taking into account the added resistive term:

- continuity

$$\widetilde{a}(\mathbf{u}_h, \mathbf{v}_h) = \int_\Omega \mu (\nabla \mathbf{u}_h + (\nabla \mathbf{u}_h)^T) : \nabla \mathbf{v}_h \, d\Omega + \int_\Omega \frac{R}{\epsilon} \mathbf{u}_h \delta_{\Gamma,\epsilon,h} \cdot \mathbf{v}_h \, d\Omega \leq$$
$$\leq \left(\mu + \frac{R}{\epsilon^2} \right) ||\mathbf{u}_h||_{H^1} ||\mathbf{v}_h||_{H^1} \qquad \forall \mathbf{u}_h, \mathbf{v}_h \in V_h^r,$$

- coercivity

$$\widetilde{a}(\mathbf{v}_h, \mathbf{v}_h) = \int_\Omega \mu(\nabla \mathbf{v}_h + (\nabla \mathbf{v}_h)^T) : \nabla \mathbf{v}_h \, d\Omega + \int_\Omega \frac{R}{\epsilon} \mathbf{v}_h \delta_{\Gamma,\epsilon,h} \cdot \mathbf{v}_h \, d\Omega \geq$$

$$\geq \frac{\mu}{1 + C_\Omega^2} ||\mathbf{v}_h||_{H^1}^2 \qquad \forall \mathbf{v}_h \in V_h^r.$$

We have used the equivalence between the H^1 semi-norm and the H^1 norm:

$$\frac{1}{\sqrt{1 + C_\Omega^2}} ||\mathbf{v}||_{H^1} \leq ||\nabla \mathbf{v}||_{L^2} \leq ||\mathbf{v}||_{H^1},$$

thanks to the Poincaré inequality:

$$||\mathbf{v}||_{L^2} \leq C_\Omega ||\nabla \mathbf{v}||_{L^2}.$$

For the resistive term we have exploited the definitions of the infimum and the supremum of the smooth Dirac function:

$$\inf_{\psi \in \mathbb{R}^+} \delta_{\Gamma,\epsilon}(\psi) = 0, \qquad \sup_{\psi \in \mathbb{R}^+} \delta_{\Gamma,\epsilon}(\psi) = \frac{1}{\epsilon}.$$

Regarding the bilinear form $b(\cdot, \cdot)$, to account for coercivity, it has to satisfy the so-called inf-sup condition:

$$\exists \beta_h > 0 : \inf_{\substack{q_h \in Q_h^s \\ q_h \neq 0}} \sup_{\substack{\mathbf{v}_h \in V_h^r \\ \mathbf{v}_h \neq \mathbf{0}}} \frac{b(\mathbf{v}_h, q_h)}{||\mathbf{v}_h||_{H^1} ||q_h||_{L^2}} \geq \beta_h > 0 \qquad \forall h > 0. \qquad (2.16)$$

Typically, the constant β_h should be independent of h. If it is not the case and for instance $\beta_h \to 0$ as $h \to 0$, the convergence properties of the method may be affected.

If the inf-sup condition is violated, i.e. if

$$\inf_{\substack{q_h \in Q_h^s \\ q_h \neq 0}} \sup_{\substack{\mathbf{v}_h \in V_h^r \\ \mathbf{v}_h \neq \mathbf{0}}} \frac{b(\mathbf{v}_h, q_h)}{||\mathbf{v}_h||_{H^1} ||q_h||_{L^2}} = 0,$$

then there exists at least a function $q_h^* \in Q_h^s$ such that

$$\sup_{\substack{\mathbf{v}_h \in V_h^r \\ \mathbf{v}_h \neq \mathbf{0}}} \frac{b(\mathbf{v}_h, q_h^*)}{||\mathbf{v}_h||_{H^1} ||q_h^*||_{L^2}} = 0$$

and therefore

$$\frac{b(\mathbf{v}_h, q_h^*)}{||\mathbf{v}_h||_{H^1}||q_h^*||_{L^2}} = 0 \qquad \forall \mathbf{v}_h \in V_h^r.$$

Thus, if $(\mathbf{u}_h, p_h)$ is a solution of (2.15), also the pair $(\mathbf{u}_h, p_h + q_h^*)$ is solution, entailing that the solution of the problem is not unique anymore. Elements as q_h^* are called spurious pressure modes, leading to numerical instabilites as the inf-sup condition is violated.

The inf-sup condition is satisfied if the FE spaces are inf-sup compatible, otherwise the problem has to be stabilized. In this work, in order to limit the computational burden of the spatial discretization, for the FE spaces V_h^r and Q_h^s, we choose equal order $r = s = 1$. Therefore the two spaces are not inf-sup stable and require a suitable stabilization.

Stabilization

As already mentioned, the discrete spaces V_h^r and Q_h^s have been chosen of the same order, equal to 1, to reduce the computational effort, but this choice requires a suitable stabilization since the pair is not stable. Moreover a relevant source of numerical instabilities is associated to the fact that the flow regime is highly advective, especially in the region of the valve. For these reasons, in order to deal with the two aforementioned sources of instabilities, we employ the Streamline Upwind Petrov-Galerkin and the Pressure-Stabilizing Petrov-Galerkin (**SUPG-PSPG**) approach. We introduce the stabilization term s (2.17). As proposed in [37] for time discretization based on the BDF scheme, we set the SUPG parameters in a straightforward way following the variational multiscale (VMS) concept, see [16].

$$
\begin{aligned}
s(\mathbf{u}_h^n, \mathbf{u}_h^{n-1}, p_h^n; \mathbf{v}_h, q_h) &= \sum_{T \in \mathcal{T}_h} (\tau_M(\mathbf{u}_h^{n-1}) \mathbf{r}_M^n(\mathbf{u}_h^n, p_h^n), \rho \mathbf{u}_h^{n-1} \cdot \nabla \mathbf{v}_h + \nabla q_h)_T + \\
&+ \sum_{T \in \mathcal{T}_h} (\tau_C(\mathbf{u}_h^{n-1}) \mathbf{r}_C^n(\mathbf{u}_h^n), \nabla \cdot \mathbf{v}_h)_T
\end{aligned}
\tag{2.17}
$$

$(\cdot, \cdot)_T$ denoting the L^2 inner product over a mesh element T. The two terms $\mathbf{r}_M^n(\mathbf{u}_h^n, p_h^n)$ and $\mathbf{r}_C^n(\mathbf{u}_h^n)$ represent the residuals of the momentum and continuity equations and are defined as

$$
\begin{aligned}
\mathbf{r}_M^n(\mathbf{u}_h^n, p_h^n) &= \rho \frac{\mathbf{u}_h^n - \mathbf{u}_h^{n-1}}{\Delta t} - \mu \Delta \mathbf{u}_h^n + \rho \mathbf{u}_h^{n-1} \cdot \nabla \mathbf{u}_h^n + \nabla p_h^n + \frac{R}{\epsilon} \delta_{\Gamma, \epsilon, h}^n (\mathbf{u}_h^n - \mathbf{u}_{\Gamma, h}^n), \\
\mathbf{r}_C^n(\mathbf{u}_h^n) &= \nabla \cdot \mathbf{u}_h^n,
\end{aligned}
$$

and the stabilization parameters τ_M and τ_C are

$$\tau_M = \left(\frac{\rho^2}{\Delta t^2} + \rho^2 \mathbf{u}_h^{n-1} \cdot \mathbf{G} \mathbf{u}_h^{n-1} + C_r \mu^2 \mathbf{G} : \mathbf{G} + \frac{R^2}{\epsilon^2} (\delta_{\Gamma,\epsilon,h}^n)^2 \right)^{-1/2},$$

$$\tau_C = (\tau_M \mathbf{g} \cdot \mathbf{g})^{-1}.$$

The quantity $C_r = 60 \cdot 2^{r-2}$, while $\mathbf{G} = J^{-T} J^{-1}$ and $\mathbf{g} = J^{-T} \mathbf{I}$ denote the metric tensor and vector, respectively, depending on the Jacobian J of the element map $\mathbf{M}_T : \widehat{T} \to T$, for $T \in \mathcal{T}_h$, mapping the reference element $\widehat{T}$ to the current one T.
It is strongly consistent method since the truncation error of the added term is zero for every value of the space discretization parameter h.

For what concerns the boundaries, the **backflow stabilization** is applied to the ones on which Neumann conditions are imposed and through which inflow occurs, in this case both the inlet and the outlet. Indeed a typical issue of the hemodynamics simulations is the instability of the artificial Neumann boundaries because of the backflow that arises [71]. The instability is due to the convective term that makes the energy balance unstable when the velocity and the normal of the boundary have opposite directions. Further details can be found in [17]. It is possible to correct these instabilities by introducing the stabilization term e:

$$e(\mathbf{u}_h^n, \mathbf{u}_h^{n-1}; \mathbf{v}_h) = (\beta \rho (\mathbf{u}_h^{n-1} \cdot \mathbf{n})_- \mathbf{u}_h^n, \mathbf{v}_h)_{\Gamma_N},$$

where $\Gamma_N = \Sigma_{in} \cup \Sigma_{out}$, $\beta \in (0, 1]$ and

$$(\mathbf{u} \cdot \mathbf{n})_- = \begin{cases} 0 & \text{if } \mathbf{u} \cdot \mathbf{n} \geq 0 \\ -(\mathbf{u} \cdot \mathbf{n}) & \text{if } \mathbf{u} \cdot \mathbf{n} < 0. \end{cases}$$

We underline that the time discretization of the stabilization term must be consistent to that used for the convective term [17].

The fully discretized and stabilized problem reads as follows.
Given $\mathbf{u}_h^0 = \mathbf{0}$, find $\mathbf{u}_h^n \in V_h^r$, $p_h^n \in Q_h^r$ for each $n = 1, ..., N$ such that $\forall \mathbf{v}_h \in V_h^r$ and $\forall q_h \in Q_h^r$:

$$\left(\rho \frac{\mathbf{u}_h^n - \mathbf{u}_h^{n-1}}{\Delta t}, \mathbf{v}_h \right) + \widetilde{a}^n(\mathbf{u}_h^n, \mathbf{v}_h) + c(\mathbf{u}_h^{n-1}, \mathbf{u}_h^n, \mathbf{v}_h) + b(\mathbf{v}_h, p_h^n) +$$
$$+ s(\mathbf{u}_h^n, \mathbf{u}_h^{n-1}, p_h^n; \mathbf{v}_h, q_h) + e(\mathbf{u}_h^n, \mathbf{u}_h^{n-1}; \mathbf{v}_h) - b(\mathbf{u}_h^n, q_h) = F^n(\mathbf{v}_h).$$

(2.18)

Algebraic formulation

The algebraic formulation is derived by introducing the scalar basis functions $\{\varphi_k(\mathbf{x})\}_{k=1}^{M_h}$ for the discrete space Q_h^r and the vectorial basis functions $\{\boldsymbol{\phi}_j(\mathbf{x})\}_{j=1}^{N_h}$ for V_h^r. Regarding the vectorial ones, they are defined introducing the basis functions of X_h^r, $\{\phi_j(\mathbf{x})\}_{j=1}^{K_h}$, where $3K_h = N_h$, such that a basis of V_h^r can be built as:

$$\left\{ \begin{bmatrix} \phi_1 \\ 0 \\ 0 \end{bmatrix}, \begin{bmatrix} \phi_2 \\ 0 \\ 0 \end{bmatrix}, ..., \begin{bmatrix} \phi_{K_h} \\ 0 \\ 0 \end{bmatrix}, \begin{bmatrix} 0 \\ \phi_1 \\ 0 \end{bmatrix}, \begin{bmatrix} 0 \\ \phi_2 \\ 0 \end{bmatrix}, ..., \begin{bmatrix} 0 \\ \phi_{K_h} \\ 0 \end{bmatrix}, \begin{bmatrix} 0 \\ 0 \\ \phi_1 \end{bmatrix}, \begin{bmatrix} 0 \\ 0 \\ \phi_2 \end{bmatrix}, ..., \begin{bmatrix} 0 \\ 0 \\ \phi_{K_h} \end{bmatrix} \right\}.$$

The total number of degrees of freedom is: $N_{tot} = N_h + M_h = 3K_h + M_h$.

The solution of the discrete problem can be written as linear combination of the basis functions:

$$\mathbf{u}_h^n(\mathbf{x}) = \sum_{j=1}^{N_h} u_j^n \boldsymbol{\phi}_j(\mathbf{x}) =$$

$$= \sum_{j=1}^{K_h} u_j^n \begin{bmatrix} \phi_j(\mathbf{x}) \\ 0 \\ 0 \end{bmatrix} + \sum_{j=1}^{K_h} u_{K_h+j}^n \begin{bmatrix} 0 \\ \phi_j(\mathbf{x}) \\ 0 \end{bmatrix} + \sum_{j=1}^{K_h} u_{2K_h+j}^n \begin{bmatrix} 0 \\ 0 \\ \phi_j(\mathbf{x}) \end{bmatrix},$$

$$p_h^n(\mathbf{x}) = \sum_{k=1}^{M_h} p_k^n \varphi_k(\mathbf{x}),$$

where the coefficients $\{u_j^n\}_{j=1}^{3K_h}$ and $\{p_k^n\}_{k=1}^{M_h}$, for $n = 1, ..., N$, have been introduced.

In the problem (2.18) we take $\mathbf{v_h} = \boldsymbol{\phi}_i$ and $q_h = \varphi_l$, $\forall i = 1, ..., N_h$ and $\forall l = 1, ..., M_h$ and we sostitute the above expressions.

Let us introduce the vectors $\mathbf{U}^n = [u_1^n, ..., u_{N_h}^n]^T$, $\mathbf{P}^n = [p_1^n, ..., p_{M_h}^n]^T$ and $\mathbf{F}^n = [F^n(\boldsymbol{\phi}_1(\mathbf{x})), ..., F^n(\boldsymbol{\phi}_{N_h}(\mathbf{x}))]^T$.

Subsequently, the following matrices are built:

- the mass matrix $M \in \mathbb{R}^{N_h \times N_h}$: $M_{ij} = \int_\Omega \boldsymbol{\phi}_j \cdot \boldsymbol{\phi}_i$,

- the stiffness matrix $A \in \mathbb{R}^{N_h \times N_h}$: $A_{ij} = a(\boldsymbol{\phi}_j, \boldsymbol{\phi}_i)$,

- the resistive matrix $R^n \in \mathbb{R}^{N_h \times N_h}$: $R_{ij}^n = r^n(\boldsymbol{\phi}_j, \boldsymbol{\phi}_i)$,

- the convective matrix $N \in \mathbb{R}^{N_h \times N_h}$: $[N(\mathbf{U}^{n-1})]_{ij} = c(\mathbf{u}_h^{n-1}, \boldsymbol{\phi}_j, \boldsymbol{\phi}_i)$,

- the matrix $B \in \mathbb{R}^{M_h \times N_h}$: $B_{lj} = b(\boldsymbol{\phi}_j, \varphi_l)$.

In order to introduce the SUPG-PSPG stabilization matrix, we rewrite the contributions of equation (2.17):

$$
\begin{aligned}
s_{11} =& \tau_M\left[\left(\rho\frac{\mathbf{u}_h^n}{\Delta t}, \rho\mathbf{u}_h^{n-1}\cdot\nabla\mathbf{v}_h\right)_T - (\mu\Delta\mathbf{u}_h^n, \rho\mathbf{u}_h^{n-1}\cdot\nabla\mathbf{v}_h)_T + (\rho\mathbf{u}_h^{n-1}\cdot\nabla\mathbf{u}_h^n, \rho\mathbf{u}_h^{n-1}\cdot\nabla\mathbf{v}_h)_T + \right. \\
& \left. + \left(\frac{R}{\epsilon}\delta_{\Gamma,\epsilon,h}^n\mathbf{u}_h^n, \rho\mathbf{u}_h^{n-1}\cdot\nabla\mathbf{v}_h\right)_T\right] + \tau_c(\nabla\cdot\mathbf{u}_h^n, \nabla\cdot\mathbf{v}_h)_T; \\
s_{12} =& \tau_M(\nabla p_h^n, \rho\mathbf{u}_h^{n-1}\cdot\nabla\mathbf{v}_h)_T; \\
s_{21} =& \tau_M\left[\left(\rho\frac{\mathbf{u}_h^n}{\Delta t}, \nabla q_h\right)_T - (\mu\Delta\mathbf{u}_h^n, \nabla q_h)_T + (\rho\mathbf{u}_h^{n-1}\cdot\nabla\mathbf{u}_h^n, \nabla q_h)_T + \left(\frac{R}{\epsilon}\delta_{\Gamma,\epsilon,h}^n\mathbf{u}_h^n, \nabla q_h\right)_T\right]; \\
s_{22} =& \tau_M(\nabla p_h^n, \nabla q_h)_T; \\
f_u =& \tau_M\left[\left(\rho\frac{\mathbf{u}_h^{n-1}}{\Delta t}, \rho\mathbf{u}_h^{n-1}\cdot\nabla\mathbf{v}_h\right)_T + \left(\frac{R}{\epsilon}\delta_{\Gamma,\epsilon,h}^n\mathbf{u}_{\Gamma,h}^n, \rho\mathbf{u}_h^{n-1}\cdot\nabla\mathbf{v}_h\right)_T\right]; \\
f_p =& \tau_M\left[\left(\rho\frac{\mathbf{u}_h^{n-1}}{\Delta t}, \nabla q_h\right)_T + \left(\frac{R}{\epsilon}\delta_{\Gamma,\epsilon,h}^n\mathbf{u}_{\Gamma,h}^n, \nabla q_h\right)_T\right].
\end{aligned}
$$

For the sake of clearness, the sum over the hexahedral mesh has been omitted.

These terms give rise to the following correspondent algebraic contributions:

$s_{11} \to \Sigma_{11}\mathbf{U}^n,\ \Sigma_{11}\in\mathbb{R}^{N_h\times N_h}, \quad s_{12}\to\Sigma_{12}\mathbf{P}^n,\ \Sigma_{12}\in\mathbb{R}^{N_h\times M_h},$

$s_{21}\to\Sigma_{21}\mathbf{U}^n,\ \Sigma_{21}\in\mathbb{R}^{M_h\times N_h}, \quad s_{22}\to\Sigma_{22}\mathbf{P}^n,\ \Sigma_{22}\in\mathbb{R}^{M_h\times M_h};$

$f_u\to\mathbf{F}_u^n, \quad f_p\to\mathbf{F}_p^n.$

On the other hand, the backflow stabilization matrix is the following:

$E\in\mathbb{R}^{N_h\times N_h}: \ [E(\mathbf{U}^{n-1})]_{ij} = (\beta\rho(\mathbf{u}_h^{n-1}\cdot\mathbf{n})_-\boldsymbol{\phi}_j, \boldsymbol{\phi}_i)_{\Gamma_N}.$

The algebraic counterpart of the problem (2.18) reads:

$$
\begin{cases}
\rho\dfrac{M}{\Delta t}\mathbf{U}^n + A\mathbf{U}^n + R^n\mathbf{U}^n + N(\mathbf{U}^{n-1})\mathbf{U}^n + \Sigma_{11}\mathbf{U}^n + \Sigma_{12}\mathbf{P}^n + E(\mathbf{U}^{n-1})\mathbf{U}^n + B^T\mathbf{P}^n = \\
\quad = \mathbf{F}^n + \mathbf{F}_u^n \\
B\mathbf{U}^n + \Sigma_{21}\mathbf{U}^n + \Sigma_{22}\mathbf{P}^n = \mathbf{F}_p^n \\
\mathbf{U}^0 = \mathbf{0}
\end{cases}
$$

where $(\mathbf{F}^n)_i = \left(\rho\dfrac{M}{\Delta t}\mathbf{U}^{n-1}\right)_i + \int_{\Sigma_{in}}p_{in}^n\mathbf{n}\cdot\boldsymbol{\phi}_i d\gamma + \int_{\Sigma_{out}}p_{out}^n\mathbf{n}\cdot\boldsymbol{\phi}_i d\gamma + \left(\frac{R}{\epsilon}\mathbf{u}_{\Gamma,h}^n\delta_{\Gamma,\epsilon,h}^n, \boldsymbol{\phi}_i\right).$

In order to simplify the notation, we set:

$K = \rho\frac{M}{\Delta t} + A + R^n + N(\mathbf{U}^{n-1}) + \Sigma_{11} + E(\mathbf{U}^{n-1});$

$\widetilde{\mathbf{F}}^n = \mathbf{F}^n + \mathbf{F}_u^n.$

Summarizing, the fully discretized and stabilized problem written in compact algebraic

form is the following.

Given $\mathbf{U}^0 = \mathbf{0}$, find $\mathbf{U}^n$, $\mathbf{P}^n$ for each $n = 1, ..., N$ such that:

$$\begin{bmatrix} K & \Sigma_{12} + B^T \\ B + \Sigma_{21} & \Sigma_{22} \end{bmatrix} \begin{bmatrix} \mathbf{U}^n \\ \mathbf{P}^n \end{bmatrix} = \begin{bmatrix} \widetilde{\mathbf{F}}^n \\ \mathbf{F}_p^n \end{bmatrix}.$$

It is important to discuss the importance of the choice of ϵ, strictly connected to the condition number. We remark that, if ϵ increases, the matrix condition number decreases, but the valve becomes thicker and thicker. Our aim is to reproduce physiological value of the valve thickness. The importance of ϵ will be also analyzed in the following.

2.5.2. Structure model

For what concerns the geometric quantities valve related, we consider a FE description, even if, since they appear only inside integrals, we do not need all of them to actually belong to a FE space.

In particular, the distance function is approximated by $\varphi_h^n \in X_h^s$ at each time t^n, with a polynomial degree $s \geq 2$ that is in general different from r, and $\delta_{\Gamma,\epsilon,h}^n$ is defined accordingly. We underline again the importance of the half-thickness ϵ. As already mentioned at the end of Section 2.5.1, ϵ has to be sufficiently small in order to reproduce physiological values. However, it must be at least 1.5 times larger than h, in order for $\delta_{\Gamma,\epsilon,h}^n$ to be correctly resolved by the mesh. As a general guideline, the mesh has to be fine in the valvular region in order to set a sufficiently small ϵ [31].

Denoting by $\{\psi_l\}_{l=1}^{N_h^s}$ the basis functions spanning X_h^s, the distance function reads:

$$\varphi_h^n = \sum_{l=1}^{N_h^s} \varphi_l^n \psi_l,$$

and the leaflets extended normal and curvature are then defined as follows:

$$\widetilde{\mathbf{n}}_{\Gamma,h}^n = \frac{\sum_{l=1}^{N_h^s} \varphi_l^n \nabla \psi_l}{\left| \sum_{l=1}^{N_h^s} \varphi_l^n \nabla \psi_l \right|},$$

$$\widetilde{H}_{\Gamma,h}^n = -\text{div } \widetilde{\mathbf{n}}_{\Gamma,h}^n =$$

$$= -\frac{\sum_{l=1}^{N_h^s} \varphi_l^n \Delta \psi_l}{\left| \sum_{l=1}^{N_h^s} \varphi_l^n \nabla \psi_l \right|} + \frac{\sum_{l=1}^{N_h^s} \varphi_l^n \nabla^2 \psi_l : \left(\sum_{l=1}^{N_h^s} \varphi_l^n \nabla \psi_l \otimes \sum_{l=1}^{N_h^s} \varphi_l^n \nabla \psi_l \right)}{\left| \sum_{l=1}^{N_h^s} \varphi_l^n \nabla \psi_l \right|^3} =$$

$$= -\frac{\sum_{l=1}^{N_h^s} \varphi_l^n \Delta \psi_l}{\left| \sum_{l=1}^{N_h^s} \varphi_l^n \nabla \psi_l \right|} + \frac{\sum_{l,m,k=1}^{N_h^s} \varphi_l^n \varphi_m^n \varphi_k^n \nabla^2 \psi_l : (\nabla \psi_m \otimes \nabla \psi_k)}{\left| \sum_{l=1}^{N_h^s} \varphi_l^n \nabla \psi_l \right|^3}.$$

In order to represent the leaflet velocity at the discrete level, we apply a first-order approximation of (2.12):

$$\mathbf{u}_{\Gamma,h}^n = \frac{c^n - c^{n-1}}{\Delta t} \widetilde{\mathbf{g}}_h.$$

Regarding the solution of the ODE equation (2.9) describing the valve dynamics it is based on an explicit, fourth-order Runge-Kutta method (see Appendix A).

2.5.3. Reduced 3D–0D FSI model

The fluid and structure models are then weakly coupled at each time-step. In particular, at each time step the fluid exchanges with the valve the stress, expressed in terms of the fluid velocity and pressure, and receives from the valve model the position and the velocity of the leaflets. More in detail, the solution of the 0D valve model is the opening coefficient which allows to compute the valve displacement, its configuration and consequently its velocity. On the other hand the blood velocity and pressure are computed by solving the 3D fluid problem. The normal vector to the valve and its curvature are assembled from the signed distance function.

Thus, we have the following scheme:

Algorithm 1: Solution scheme for the 3D-0D FSI model

Given $\mathbf{u}_h^n$, p_h^n, c^n for $n = 0$, and computed the functions φ^n, $\widetilde{\mathbf{n}}_\Gamma^n$, $\widetilde{H}^n$
   corresponding to the surface Γ^n for $n = 0$

for $n = 1$ *to* N **do**

    1. Compute the integrals that make up (2.9), in terms of
        $\mathbf{u}_h^{n-1}$, p_h^{n-1}, Γ^{n-1}, φ^{n-1};

    2. Find c^n by advancing the 0D equation (2.9) with a step
        of an explicit fourth-order Runge-Kutta method;

    3. Move the immersed surface to its new configuration Γ^n
        described by $\mathbf{d}_\Gamma^n = c^n \mathbf{g}$ and compute $\mathbf{u}_\Gamma^n = \dfrac{c^n - c^{n-1}}{\Delta t} \widetilde{\mathbf{g}}$;

    4. Compute the new signed distance function φ^n w.r.t. Γ^n and
        assemble the normal and curvature fields $\widetilde{\mathbf{n}}_\Gamma^n$ and $\widetilde{H}^n$;

    5. Find $(\mathbf{u}_h^n, p_h^n) \in V_h^r \times Q_h^r$ by solving the linear problem (2.18).

end

2.6.   Lumped-parameters model of the cardiovascular system

As boundary conditions at the inlet and outlet sections of the domain we impose the pressure values obtained from the lumped circulation. In particular, solving stand-alone the lumped-parameters model which represent the whole cardiovascular system, including the pulmonary artery and the pulmonary valve, allows to derive the pressure values that are imposed as boundary conditions of the fluid problem. We point out that the lumped-parameters model of the cardiovascular system, object of this section, does not receive any condition from the fluid model and thus we are proceeding in "one-way".

Solving the whole cardiovascular system with a 3D system is currently not affordable because of the complexity of the computational domain composed by a large number of vessels and the multitude of different length scales required to accurately represent the flow in the various regions of the cardiovascular system. Moreover, the huge amount of data that would be generated by such simulations is costly to process, of difficult clinical interpretation and it is not necessary, since a detailed description of the microscopic behavior of the hemodynamics variables is requested only in the domain of interest [36, 72]. However, it is possible to devise simplified models exploiting specific features of blood flow. Even though these models are highly simplified with respect to the local dynamics, they can provide reliable numerical results at a low computational cost. Interpretation is much straightforward, thus making them ideal as an everyday tool for use in clinical practice. Moreover, these models are well-suited for describing systemic dynamics such as feedback mechanisms that play an important role in the correct working of the vascular system. These dynamics typically involve mechanical and biochemical phenomena that can be hardly described in terms of complete 3D models [36].

In many applications, reduced-dimensional models are used, either as stand-alone models or coupled with the 3D ones [72]. We consider the 0D model as a stand-alone model to obtain the boundary conditions for the 3D fluid model in our domain of interest, i.e. the pulmonary artery.

In the 0D (or lumped-parameters) model the space dependence is lost and consequently the variables are only time-dependent. The 0D model is based on the concept of compartment. A compartment is a set of vascular districts that is appropriate to regard as a unit for the application at hand; the behavior of the blood is described in terms of flow rate and pressure averaged over the compartment length [71, 72]. On a compartment, the features of the vessels are lumped in a few parameters set on physiological measured data.

The associated mathematical model is typically based on differential algebraic equations (DAE), often represented in terms of hydraulic or electric networks [36]. Blood flow in the circulatory system and electric conduction in a circuit have much similarity: blood pressure gradient in the circulatory loop drives the blood to flow against the hydraulic impedance; similarly, voltage gradient in a circuit drives current to flow against the electric impedance. Hydraulic impedance represents the combined effect of the frictional loss, vessel wall elasticity and blood inertia in the blood flow, whilst electric impedance represents the combination of the resistance, capacitance and inductance in the circuit [82]. Systemic and pulmonary circulations are modeled with resistance-inductance-capacitance (RLC) circuits, one for the arterial part and the other one for the venous part. In Table 2.1 we summarize the hydraulic/electric analogy.

The heart is a special "compartment" of the vascular system that needs a specific representation in the lumped-parameters framework [34]. The four chambers are modeled by time-varying elastance elements, whereas the four valves are represented as non-ideal diodes [73].

HYDRAULIC	ELECTRIC
Pressure	Voltage
Flow rate	Current
Blood viscosity	Resistance R
Blood inertia	Inductance L
Wall compliance	Capacitance C

Table 2.1: Analogy between electric and hydraulic networks.

The analytical expression of the valve resistance is defined as $R = 10^c$, where c is:

$$c = log_{10}R_{min} + (log_{10}R_{max} - log_{10}R_{min}) \cdot \left[\frac{1}{2} + \frac{1}{\pi}\arctan\left(\frac{k\pi}{2}(P_2 - P_1)\right)\right],$$

where R_{max} is the resistance when the valve is closed and R_{min} corresponds to the resistance when the valve is open; P_1 and P_2 are the pressures ahead and behind the valve, respectively. In Figure 2.3, the evolution of R, in which we have set $k = 200$, is plotted.
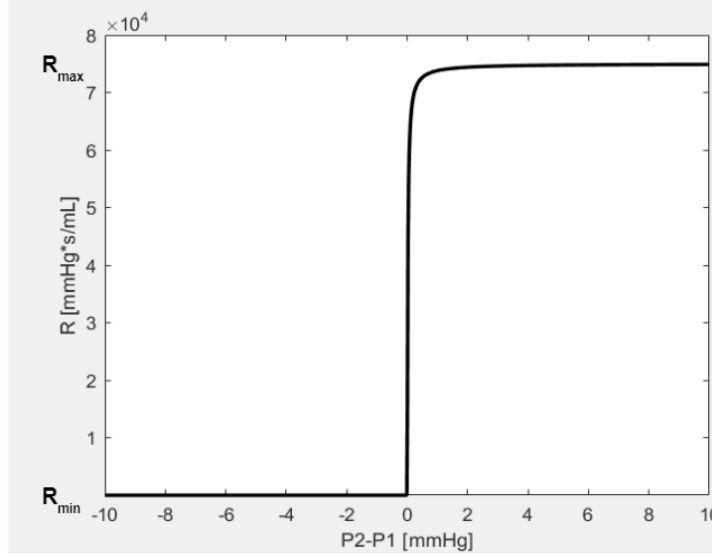
Figure 2.3:   Evolution of the valve resistance R.

The considered circuital scheme is illustrated in Figure 2.4 [73]. The variables, showing up in Figure 2.4, are the following:

- p_{LA}, p_{LV}, p_{RA}, p_{RV} are the pressures of the left atrium, left ventricle, right atrium and right ventricle, respectively;

- $p_{AR,SYS}$, $p_{VEN,SYS}$, $p_{AR,PUL}$, $p_{VEN,PUL}$ are the pressures in the systemic arterial system, in the systemic venous system, in the pulmonary arterial system and in the pulmonary venous system, respectively;

- $Q_{AR,SYS}$, $Q_{VEN,SYS}$, $Q_{AR,PUL}$, $Q_{VEN,PUL}$ are the flow rates in the systemic arterial system, in the systemic venous system, in the pulmonary arterial system and in the pulmonary venous system, respectively;

- Q_{MV}, Q_{AV}, Q_{TV}, Q_{PV} are the flow rates through the mitral, aortic, tricuspid and pulmonary valve, respectively;

- E_{LA}, E_{LV}, E_{RA}, E_{RV} are the elastances of the left atrium, left ventricle, right atrium and right ventricle, respectively;

- $R_{AR,SYS}$, $R_{VEN,SYS}$, $R_{AR,PUL}$, $R_{VEN,PUL}$, $R_{UP,SYS}$, $R_{UP,PUL}$ are the resistances in the systemic arterial system, in the systemic venous system, in the pulmonary arterial system and in the pulmonary venous system, upwind the systemic and pulmonary circulations, respectively;

- R_{MV}, R_{AV}, R_{TV}, R_{PV} are the resistances of the mitral, aortic, tricuspid and pul-

monary valve, respectively;

- $L_{AR,SYS}$, $L_{VEN,SYS}$, $L_{AR,PUL}$, $L_{VEN,PUL}$ are the inductances in the systemic arterial system, in the systemic venous system, in the pulmonary arterial system and in the pulmonary venous system, respectively;

- $C_{AR,SYS}$, $C_{VEN,SYS}$, $C_{AR,PUL}$, $C_{VEN,PUL}$ are the capacitances in the systemic arterial system, in the systemic venous system, in the pulmonary arterial system and in the pulmonary venous system, respectively.

Other variables, non reported in the figure, are:

- V_{LA}, V_{LV}, V_{RA}, V_{RV} are the volumes of the left atrium, left ventricle, right atrium and right ventricle, respectively.

The elastances, resistances, inductances and capacitances have to be prescribed and properly tuned, see e.g. [3].
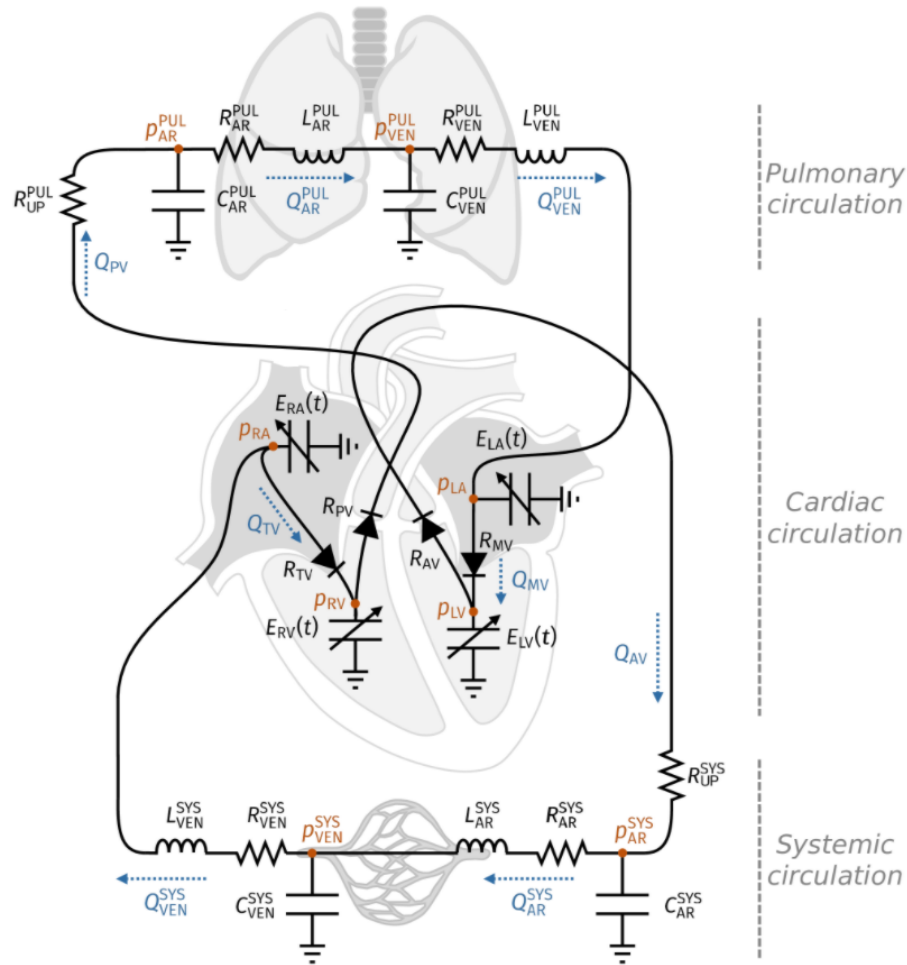
Figure 2.4: Circuital scheme of the full 0D circulation model [3].

The compact form of the complete 0D problem is the following. Find $\mathbf{c}_1$, $\mathbf{c}_2$, for any $t \in (0, T]$, such that:

$$
\begin{cases}
\dfrac{d\mathbf{c}_1(t)}{dt} & = \mathbf{D}(t, \mathbf{c}_1(t), \mathbf{c}_2(t)) \\
\mathbf{c}_2(t) & = \mathbf{W}(t, \mathbf{c}_1(t)) \\
\mathbf{c}_1(0) & = \mathbf{c}_{1,0}
\end{cases}
\tag{2.19}
$$

where $\mathbf{c}_1(t)$ is the vector of state variables and $\mathbf{c}_2(t)$ is the vector of algebraic variables:

$$
\begin{aligned}
\mathbf{c}_1(t) =& (V_{LA}(t), V_{LV}(t), V_{RA}(t), V_{RV}(t), p_{AR,SYS}(t), p_{VEN,SYS}(t), p_{AR,PUL}(t), p_{VEN,PUL}(t), \\
& Q_{AR,SYS}(t), Q_{VEN,SYS}(t), Q_{AR,PUL}(t), Q_{VEN,PUL}(t))^T, \\
\mathbf{c}_2(t) =& (p_{LV}(t), p_{LA}(t), p_{RV}(t), p_{RA}(t), Q_{MV}(t), Q_{AV}(t), Q_{TV}(t), Q_{PV}(t))^T.
\end{aligned}
$$

Details can be found in [73].

The time discretization of the lumped-parameters model (2.19) is achieved by means of the classical 4th order Runge-Kutta explicit method (see Appendix A). At the end of the discretization procedure we find out p_{RV}^n and $p_{AR,PUL}^n$, that can be interpreted as the inlet and outlet pressure, p_{in}^n and p_{out}^n respectively, showing up in the discretized fluid problem.

3 | Pre-processing and mesh generation

In this chapter we focus on the first step of our work, i.e. the set up of the computational domain for the numerical simulations. Starting from the clinical images, provided by the Division of Cardiovascular Surgery of the Department of Cardiology of Niguarda Hospital, Milan, some technical steps have to be performed in order to obtain the computational domain.

To achieve this goal the softwares used have been vmtk, ParaView and MatLab.

Vmtk (The Vascular Modeling ToolKit) [7] is a collection of scripts and classes for image segmentation, geometric characterisation and processing, mesh generation and post-processing for vascular modeling. Paraview [6] is a software useful to visualize and post-process the results of the numerical experiments and also to analyze the data using qualitative and quantitative techniques. Finally Matlab (Matrix Laboratory) [5] is a numerical computing and statistical analysis environment. It is based on the use of the C language applied to matrix calculation, which allows to manipulate functions and data, draw graphs or implement algorithms that can interface with other programs and software.

We consider data of two different patients of the Niguarda Hospital. Since they are anonymous, we distinguish data and results by naming Patient 1 and Patient 2.

The **clinical image acquisition** is executed by the hospital, with a computed tomography (CT) technology with constrast agent (Figure 3.1).

The CT is a computerized x-ray imaging procedure in which a narrow beam of x-rays is aimed at the patient and quickly rotated around the body, producing signals that are processed by the machine computer to generate cross-sectional images, or "slices", of the body. Once a number of successive slices is collected, they can be digitally "stacked" together to form a three-dimensional image of the patient that allows for easier identification and location of basic structures [48].

Contrast agents are indispensable to more clearly differentiate anatomic structures and to detect and characterize abnormalities [75], thanks to their iodine content, an element
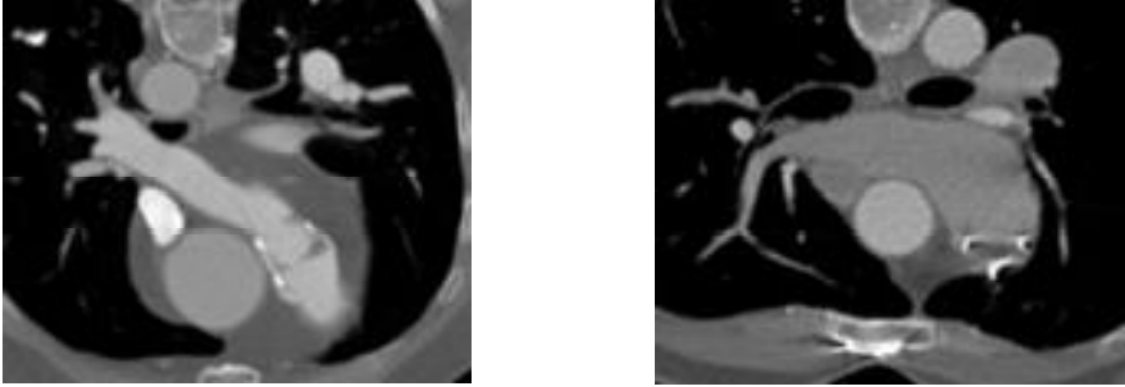
Figure 3.1: CT of Patient 1 (*left*) and Patient 2 (*right*) provided by Niguarda Hospital.

able to absorb radiations. The result of a CT is a series of greyscale images given by the structure of bones and organs. The greyscale changes in relation to the radiological density: as the density increases, the color approaches white. The scale used to describe the radiodensity is the Hounsfield (HU). The pulmonary arteries have a radiological density between 200 HU and 450 HU [46].

Since the medical images are often affected by noise and artifacts that may interfere with the quality of the final results of the pre-processing step, an **imaging enhancement** is usually performed [72].

Then the hospital images are converted from DICOM format, standard for all CT images, into the mhd (MetaImage Header) format, suitable for modern software for image-based modeling of blood vessels.

3.1.   Pulmonary artery

After the image acquisition and imaging enhancement steps, the image undergoes the **segmentation** process. This step was already performed in a previous work [69]. The goal of the segmentation step is to extract the region of interest, in our case the pulmonary artery. The separation between anatomical districts is identified thanks to a sudden variation of grey. Using this procedure, the vessel wall, the valve leaflets and the metallic stent are not reconstructed since they have a different scale.

After the segmentation process, the surface appears rough and irregular, principally due to the presence of noise in the clinical images. Thus, in order to perform consistent simulations, the quality of the surface and of the boundaries must be improved. In particular, since the central portion of the pulmonary trunk, in correspondence of the valve, appears very irregular, it is improved by deforming and adapting a cylinder to the desired morphology, applying an iterative procedure with ParaView and vmtk. Indeed

this irregularity, caused by the fact that the software has as input also the greyscale correspondent to the blood and it reconstructs the morphology of the vessel thanks to the volume occupied by the fluid, does not reflect the smooth vessel wall and has to be corrected. Moreover also the circular contours, where the boundary conditions are applied, are regularized. The final arteries, reconstructed in [69], can be observed in Figure 3.2. In [69] it is also present the construction of a reference system in the vessel (function *phi*), in which the values 0 and 1 are imposed in correspondence of the inflow and the outflow respectively (Figure 3.2). Moreover in that work, using the command *polyfit* of Matlab, the authors have generated the function *edgelength* (Figure 3.2), that describes the characteristic length h, relating it to the reference system *phi* (Figure 3.3).

Patient 1

Patient 2
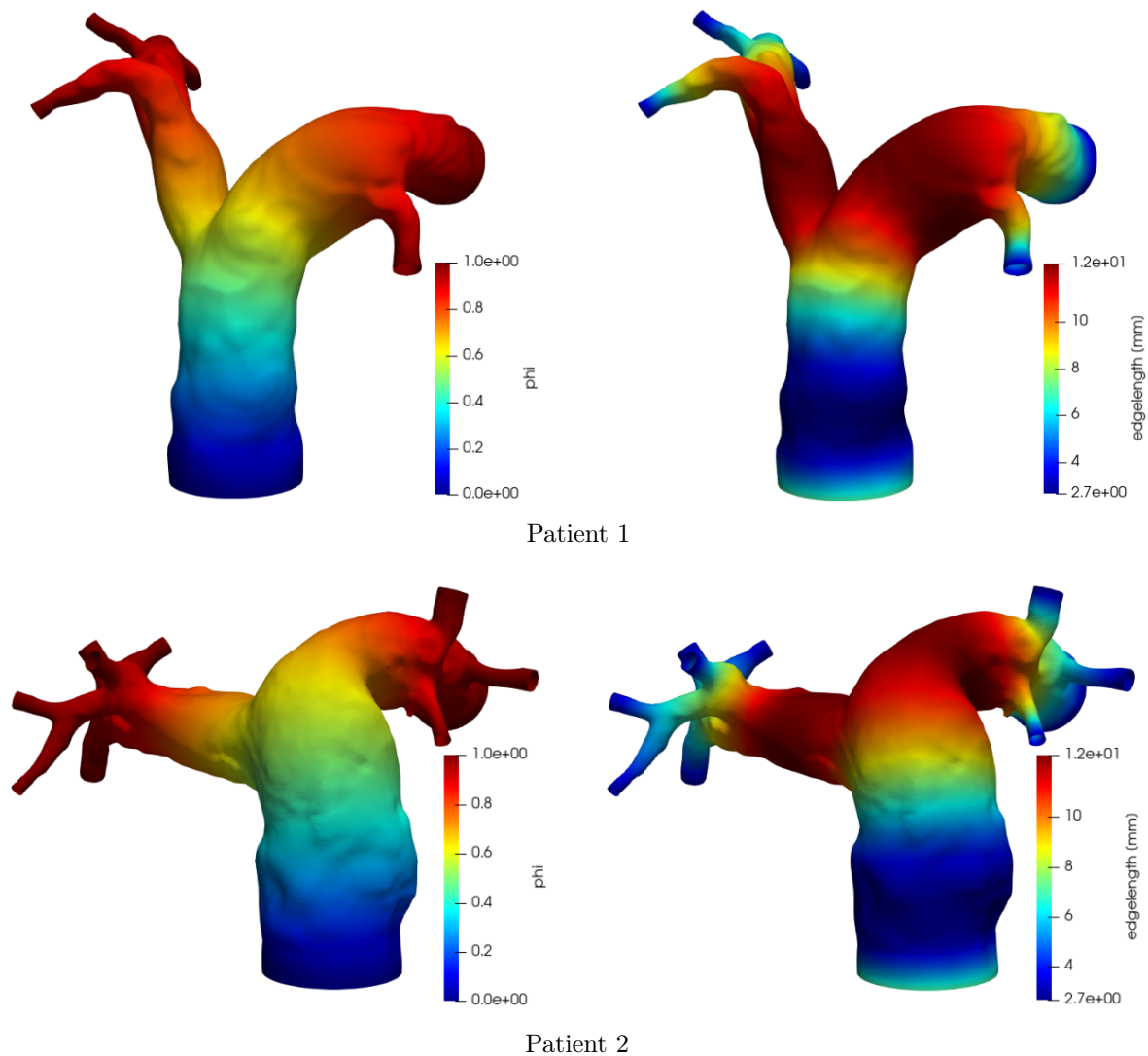
Figure 3.2: Functions *phi* (*left*) and *edgelength* (*right*).

In our work, in order to simplify the imposition of the boundary conditions, we consider
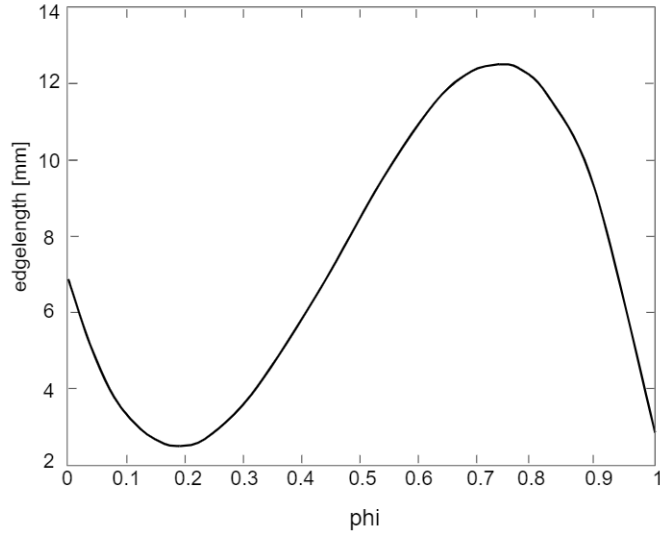
Figure 3.3: Function *edgelength* with respect to the independent variable *phi*.

two outlets only, the right and the left pulmonary arteries, making them of almost the same length, cutting, with ParaView, the geometry just before the secondary branches. Finally the boundaries are capped, applying the command `vmtksurfacecapper` of vmtk, and the surface is smoothed (Figure 3.4).

In the last step of the computational domain reconstruction pipeline the focus is on the generation of a **computational volumetric mesh**. The aim is to obtain a hexahedral non-uniform mesh, with low characteristic length in correspondence of the valve, our region of interest, to ensure higher accuracy. For this purpose we have started from the two aforementioned functions *phi* and *edgelength*. We remark that these functions are relative to the geometry considered in [69], that means before the cutting and capping steps.

Thus, to obtain a detailed description, the values of *edgelength* have be manipulated in order to obtain $h \simeq 3.6 \ mm$ and $h \simeq 8 \ mm$ in correspondence of the valve and of the bifurcation, respectively. Then using the command `vmtksurfaceprojection` we have projected the *edgelength* from the initial geometries onto the cut ones (Figure 3.5). Finally we have used the command `vmtksurfaceremeshing` to generate the surface mesh, with the average characteristic length contained in the array *edgelength*.

For each one of these steps the output file extension is *.vtp*.

Patient 1

Patient 2
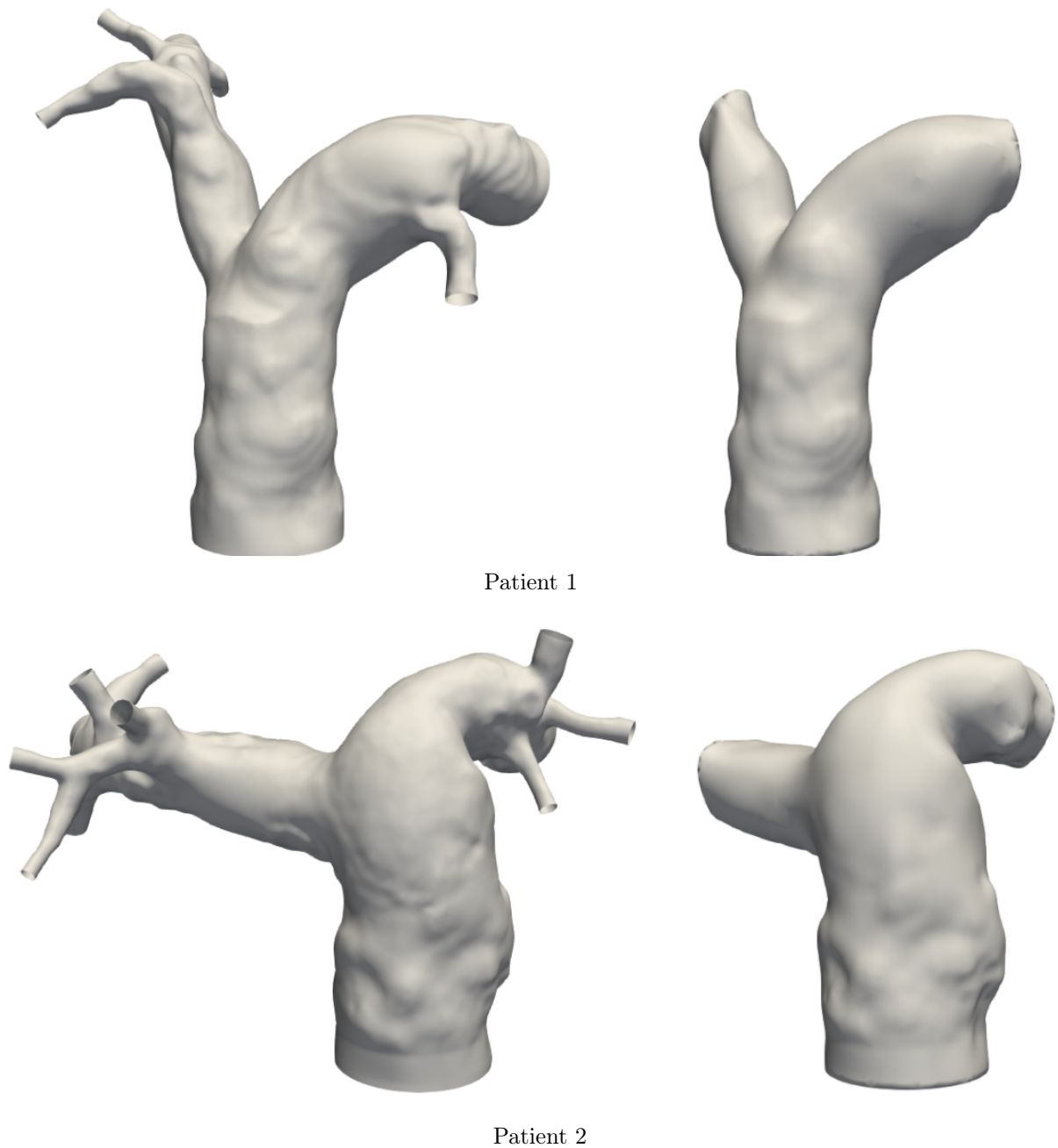
Figure 3.4: Pulmonary artery reconstructed by [69] (*left*) and after the cutting and capping procedures (*right*).

The next step consists in filling the volume by means of tetrahedral elements. This is achieved with the command `vmtkmeshgenerator`. In this case the output file is in the *.vtu* format, suitable for a volumetric geometry with unstructured grid. In vmtk the tetrahedral elements are generated on the Tetgen algorithm allowing to create a Delaunay high-quality tetrahedralization. A detailed description of the algorithm can be found in [12].

Since Life^x works with hexahedral elements, the tetrahedral mesh is converted into a hexahedral one. The command `vmtkmeshtethex` provides a hexahedral mesh, by splitting each tetrahedron (volume mesh element) in four hexahedra and each triangle (surface mesh element) in three quads. The surface quads have approximately half of the characteristic length with respect to the correspondent starting triangles. The output file extension is still *.vtu*. Finally the mesh file is exported and written into the disk in the format *.msh* with the command `vmtkmeshwriter`.

Patient 1
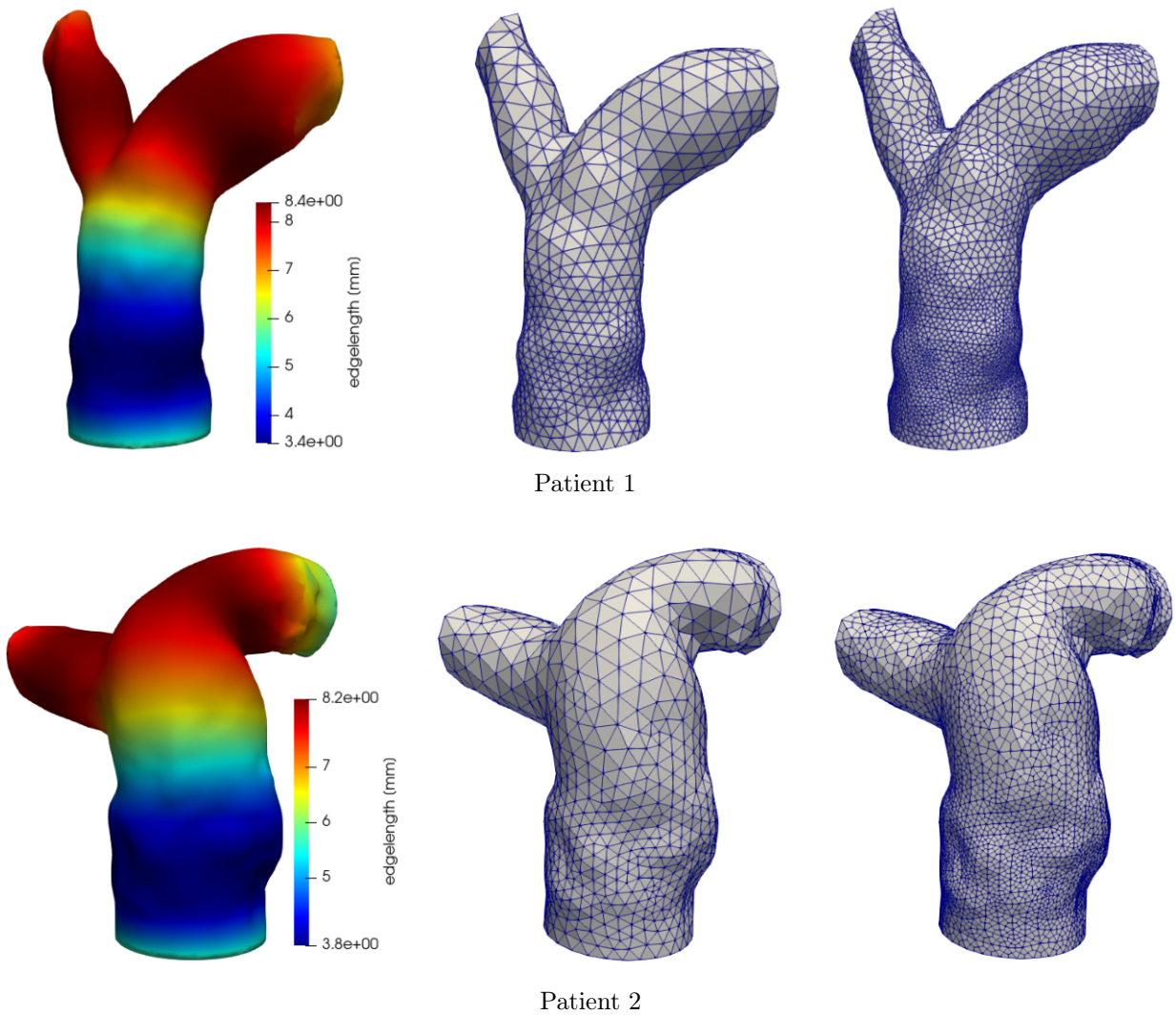
Patient 2

Figure 3.5: *edgelength* (*left*), tetrahedral mesh (*center*) and hexahedral mesh (*right*).

All these steps have been performed to produce for the two patients a similar cell diameter, both the average and especially the minimum value (Table 3.1). These values allow to have enough accuracy and they are consistent with those used in other works.

	Patient 1	Patient 2
Number of degrees of freedom	235988	276676
Number of active cells	51752	61036
Maximum cell diameter [m]	0.00779642	0.00697939
Minimum cell diameter [m]	0.00121902	0.00121843
Average cell diameter [m]	0.00280893	0.00292343

Table 3.1: Hexahedral mesh.

3.2. Pulmonary valve

For the purpose of a correct hemodynamic simulation, it is needed not only the segmentation of the vessel, but also the reconstruction of the internal structures that can affect the flow, in our case the valve. Indeed, since the flow field strongly depends on the pulmonary valve function, the latter should be necessarily included in our model. The valve has to be first reconstructed and then correctly positioned in the artery, by considering the location of the valve sinuses, the commissures (the area where the valve leaflets abut one another) and the orientation of the valve itself. We are interested in both the open and closed configurations of the valve. These steps are of utmost importance since the hemodynamics is greatly affected by the geometrical configuration of the valve.

3.2.1. Reconstruction

The valve leaflets are not recognizable from the CT, due to the low resolution of the tomographic data, as already discussed in Section 1.7. This critical issue has been solved by using a model of valve provided by MOX Laboratory of Politecnico di Milano in the iHEART project, starting from a model developed by Zygote [9] (Figure 3.6).

3.2.2. Positioning

The valve has to be first correctly oriented and then properly rotated.
As first step we have extracted a ring on the artery wall just after the sinuses, i.e. towards the outlet. Thanks to the command `vmtkimageseeder` we have selected the points of the CT corresponding to the six vertices of the hexagonal stent and then we have joined them in ParaView (Figure 3.7). The ring and the circumference passing through the six vertices are useful to define the valve scaling, since they allow to calculate the enlargement or reduction factor of the model.
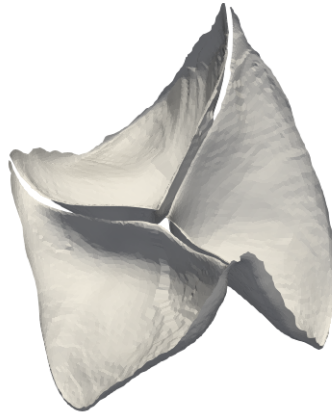
Figure 3.6: Zygote valve model.

Afterwards a rigid registration of the ring to the stent is applied through the Iterative Closest Point (ICP) algorithm proposed by Besl [18]. Registration is the process of transforming different sets of data into one coordinate system. According to the ICP algorithm, one point cloud, the reference, is kept fixed, while the other one, the source, is transformed to best match the reference. The algorithm needs to find for each point in the source point cloud the nearest point in the reference point cloud, so that all 3D source coordinates can be correctly matched. In vmtk the distance computation is performed by applying the command `vmtkicpregistration` and by selecting the ring as reference and the stent as source surface. The next step consists in translating the valve leaflets, applying the command `vmtksurfacetransform`. The input matrix that contains the information needed to transform the surfaces is provided by the distance computed in the previous step.

Once the valve is correctly oriented, it must undergo a planar rotation to make the commissures conforming to those extracted from the CT (Figure 3.7). This is achieved thanks to ParaView and to the same vmtk commands.

Finally the valve has to be resized, first according to the reduction/enlargement factor previously found and then to correctly match the artery dimensions. For what concerns the latter, the aim is to keep fixed the internal points of the valve and to translate the most extreme ones. Using ParaView we have generated a function such that the points belonging to the central part of the valve have value 0, the perimetric ones have value 1 and the other points have values ranging from 0 to 1 starting from the interior and approaching the perimeter (Figure 3.8). We have computed the minimum pointwise vectorial distance between the valve and the artery wall with the command `vmtksurfacedistance` and multiplied it for the aforementioned function. Then we have translated each point of the valve by the result quantity (Figure 3.9) with ParaView. Finally the surface has been smoothed (Figure 3.9).

These steps have to be repeated for both patients due to the patient-specificity of the model.

<div align="center">Patient 1   Patient 2</div>
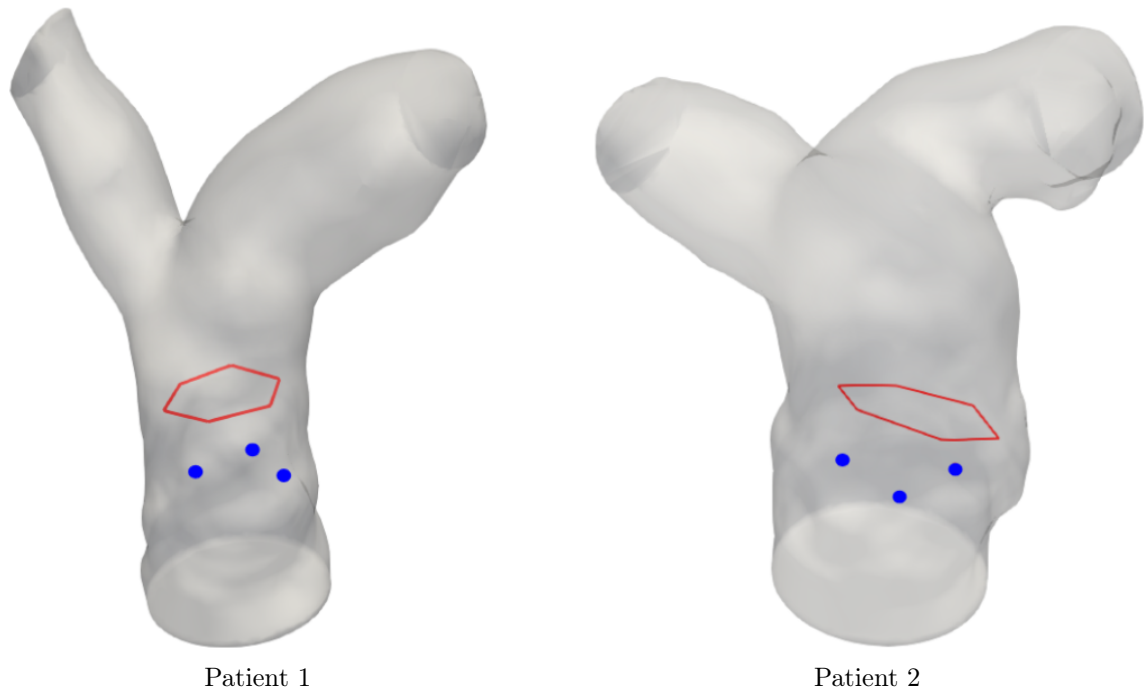
Figure 3.7: Stent (*in red*) and commissures (*in blue*).
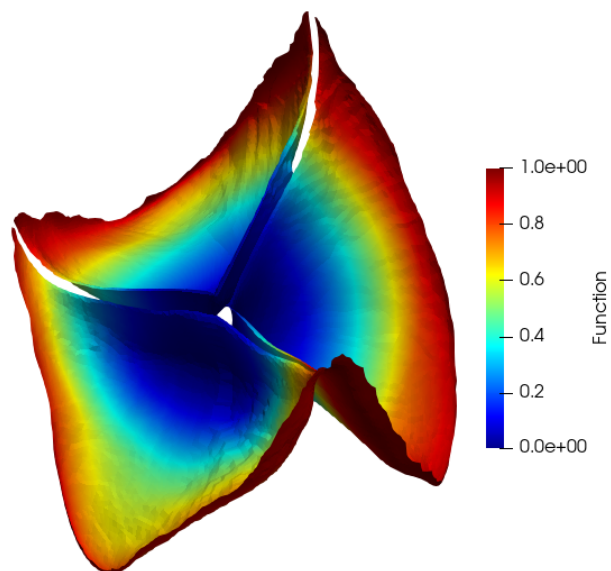
Figure 3.8: Valve resizing function. The internal points have value 0, the perimetric ones have value 1.
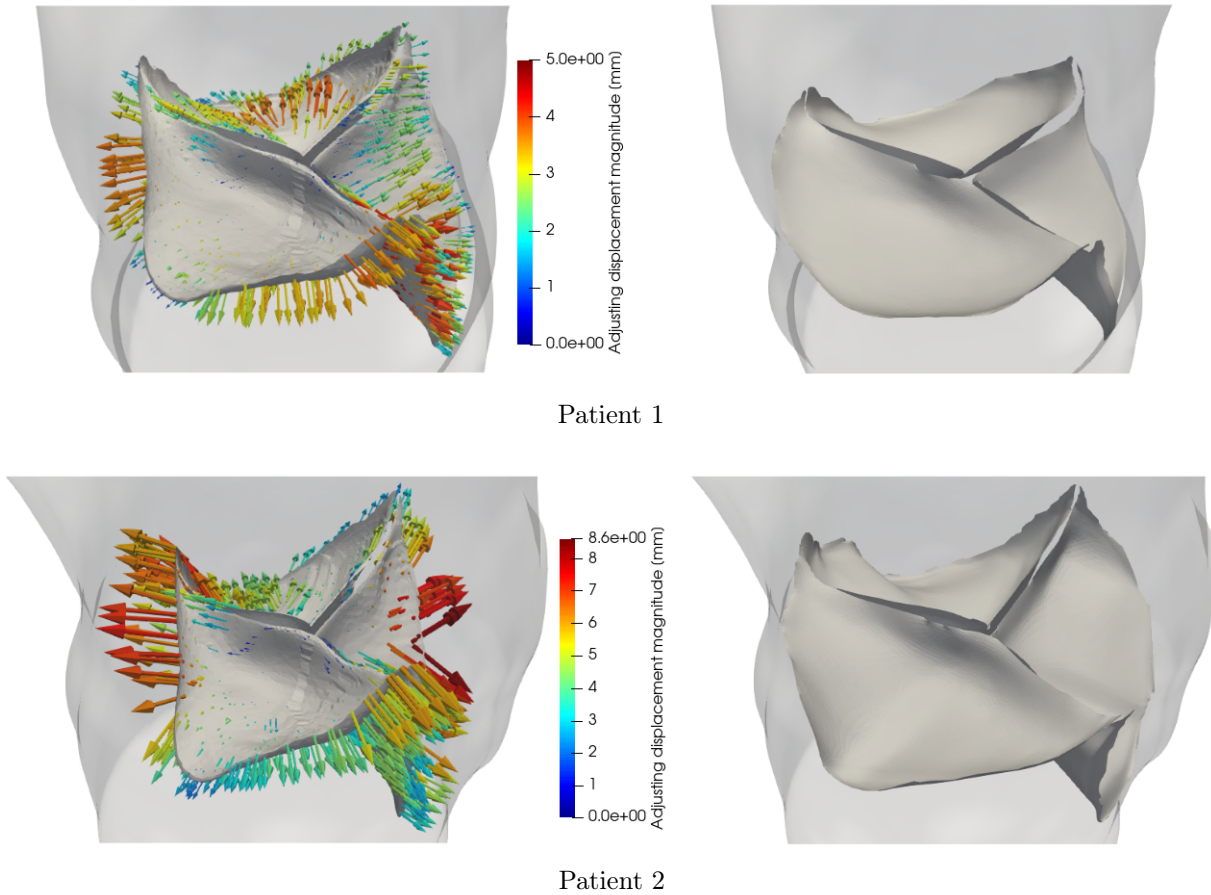
Patient 1

Patient 2

Figure 3.9: Adjusting displacement array (*left*) and closed valve configuration (*right*). In order to obtain the final closed configuration, such that the perimetric points of the valve adhere to the artery wall, each point has to be translated by the adjusting displacement array.

3.2.3.   Open and closed configurations

Starting from the closed configuration of the valve, we have adapted the open one, already provided by MOX Laboratory, to our geometry. The open configuration is geometrically reconstructed from the closed one. In particular, each point of the valve in the closed position has to be translated in order to obtain the open one. This step is performed trying to construct an open valve such that the leaflets adhere as much as possible to the artery wall. The displacement array joining the closed with the open configuration (Figure 3.10) has been smoothed with the command `vmtksurfacearraysmoothing`.
The displacement array, together with the closed position, are provided to the valve model, which reproduces the movement of the valve between the open and closed configurations. The open configuration is not solution of the 3D-0D FSI model, but it is given to the model as datum being obtained by translating each point of the closed valve by the displacement

array.

The open configurations of the pulmonary valve for Patient 1 and Patient 2 are reported in Figure 3.10.

We remark, also in this case, the importance of repeating the procedure for both patients due to the dependence of the open position of the valve on the geometrical configuration of the artery.

In Figure 3.11 it is possible to observe the pulmonary valve in both its closed and open configurations, immersed in the pulmonary artery, for Patient 1 and Patient 2.
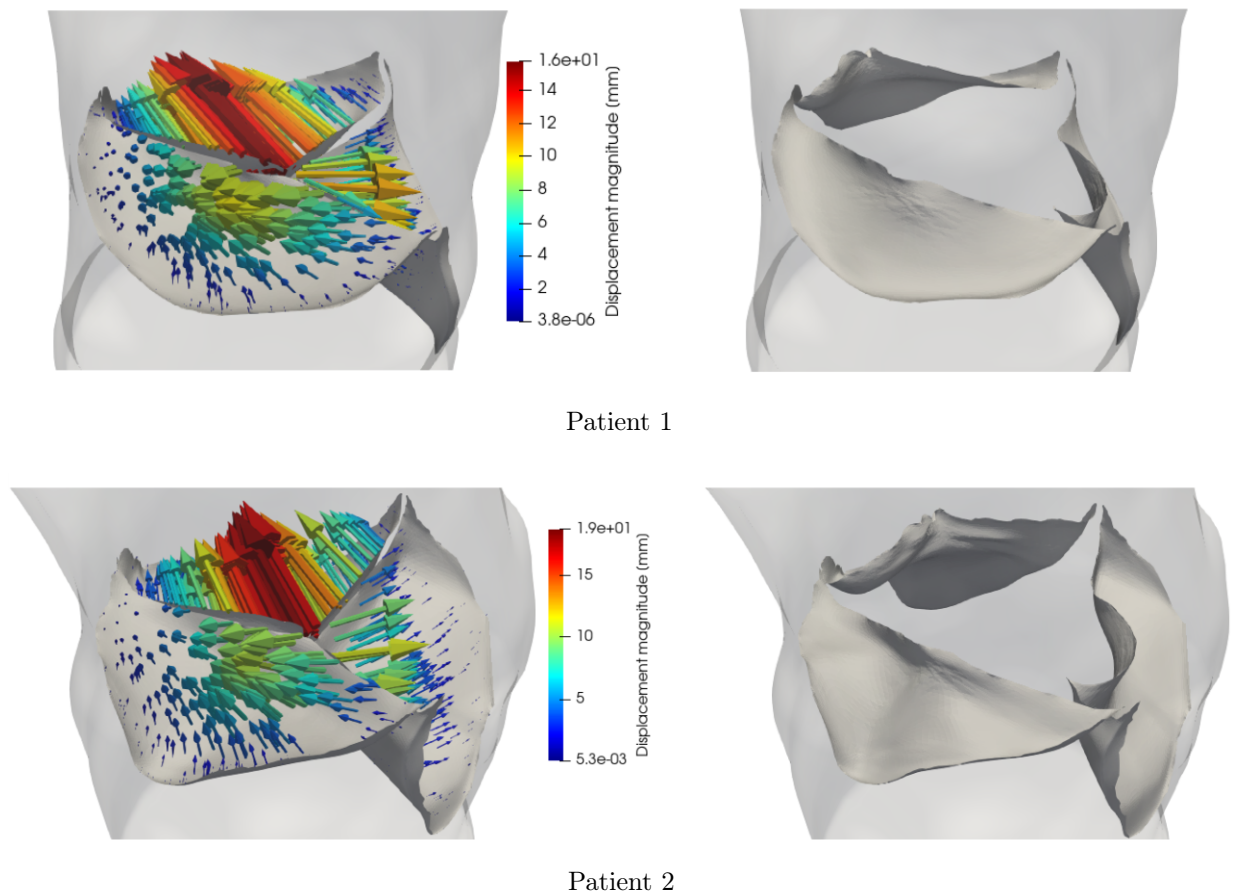
Patient 1

Patient 2

Figure 3.10: Displacement array which joins each point of the closed valve with the open valve (*left*) and open valve configuration (*right*).
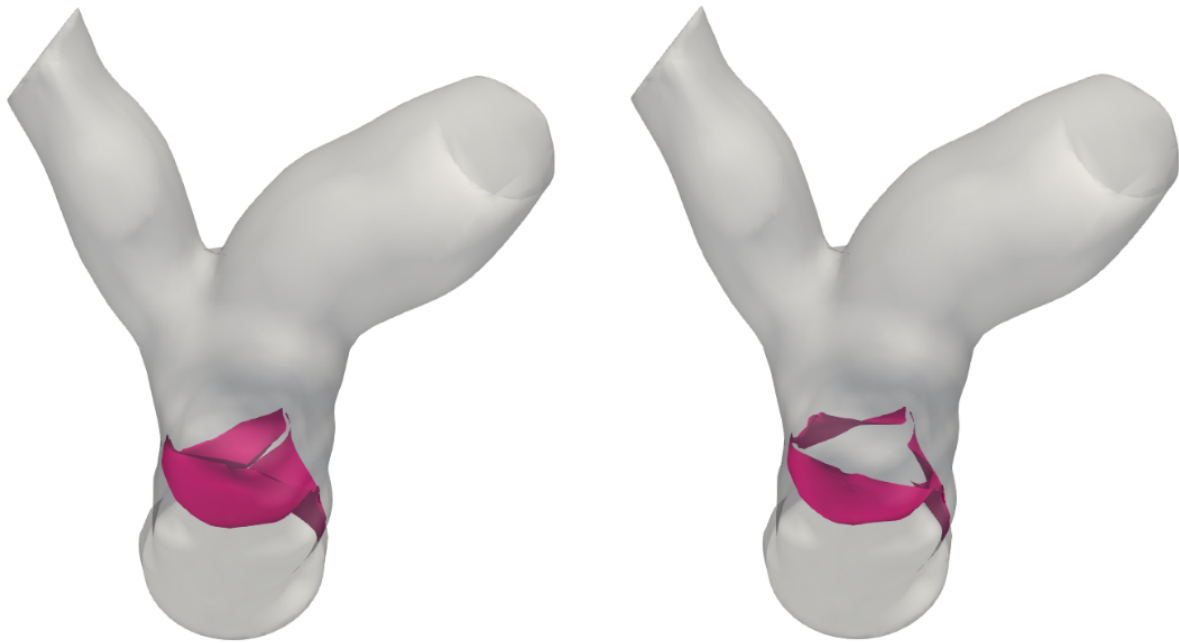
Patient 1
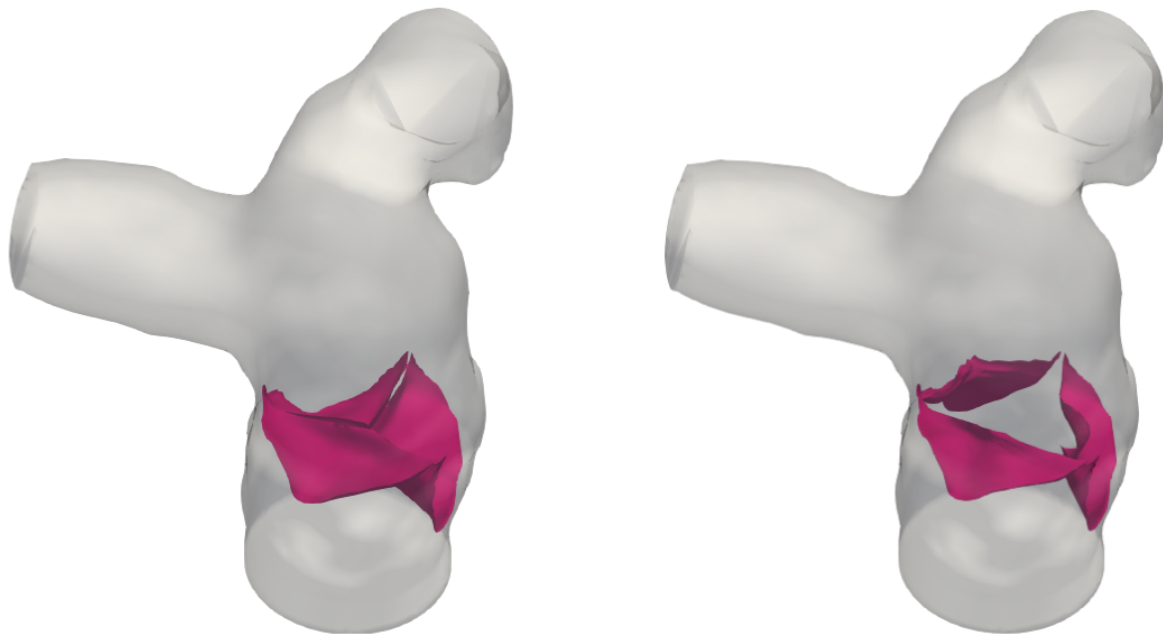
Patient 2

Figure 3.11: Pulmonary valve (*in pink*) in its closed (*left*) and open (*right*) configurations.

4 | Numerical results

This chapter is devoted to the results of the hemodynamic simulations of the problem arising from the fluid-structure interaction between the blood flow in the pulmonary artery and the pulmonary valve.

First of all, in Section 4.1 we report some information about the cluster and the numerical and physiological parameters of the simulations.

Section 4.2 is dedicated to the imposition of the boundary conditions of the fluid problem, that are obtained by a simulation of the whole 0D cardiovascular system. The validity of the parameters concerning the pulmonary valve is proved by a sensitivity analysis. We recall that the 0D model of the whole cardiovascular system is solved independently, not receiving any condition from the 3D fluid model, as already highlighted in Section 2.6. Afterwards we analyze two different scenarios:

- Scenario *Trial*: we address preliminarily, in Section 4.3, the case in which the valve motion law is prescribed;

- Scenario *Full FSI*: the valve motion is described by the lumped-parameters valve model, introduced in Section 2.3. We detail the calibration procedure of the model parameters in Section 4.4 and we present the hemodynamic results by means of visualizations of velocity, pressure, wall shear stress and Q-criterion in Section 4.5.

Finally in Section 4.6 we collect the main achievements of our study.

4.1. Setting of the numerical simulations

The numerical problem is solved through Life^x [3], a high-performance Finite Element library, written in C++ and based on the deal.II Finite Element core [2]. It is developed by the laboratory for modeling and scientific computing of Politecnico di Milano, the MOX Laboratory, in the iHEART project. It is focused on the mathematical models and numerical methods for cardiac applications, concerning, for instance, elastodynamics, electrophysiology or fluid dynamics. The numerical simulations have been performed in parallel, on the clustered computational resources of Politecnico di Milano, in the queue

gigatlong on a processor relying on 5 nodes with 160 cores 4x Xeon E5-4610 v2 (2.3GHz) 1.2TB RAM. The simulations have been performed with 32 cores selected.

In order to perform the hemodynamic simulations concerning the interaction between the blood flow and the valve, some input parameters are modified in a parameters file, a script in the *.prm* format. It contains the needed information related to the numerical and physiological parameters and the addressed tags of the domain boundary to impose boundary conditions, in addition to the path of the computational mesh and the valve surface.

We report the parameters which are commons to all simulations:

Blood flow parameters

- blood density: $\rho = 1.06\ 10^3\ \frac{Kg}{m^3}$;

- blood dynamic viscosity: $\mu = 3.5\ 10^{-3}\ Pa \cdot s$.

Numerical parameters

- time step: $\Delta t = 10^{-4}\ s$;

- heartbeat period: $T = 0.8\ s$;

- BDF time scheme order $= 1$;

- velocity FE space degree $= 1$;

- pressure FE space degree $= 1$;

- SUPG-PSPG stabilization;

- backflow stabilization on Neumann boundaries with $\beta = 1$;

- the linear system is solved by means of the generalized minimum residual (GMRES) algorithm:

    - Maximum number of iterations $= 1000$;

    - Tolerance $= 1e$-5;

    - SIMPLE preconditioner (Semi-Implicit Method for Pressure Linked Equations).

For time-independency, we find that when the chosen time step is halved, the results are not affected by appreciable changes.

RIIS parameters

- $R = 10000\ \frac{kg}{m\ s}$;

- $\epsilon = 0.0025 \ m$.

The value of the resistance R is chosen to weakly enforce the no-slip condition on the valve leaflets, even in case a high pressure gradient occurs across them.

We underline that the value of the half-thickness of the pulmonary valve surface ϵ is imposed relying on the mesh size in the region of the valve. Indeed, in order to capture correctly the valve motion in the fluid domain, the value of ϵ needs to be sufficiently large.

4.2. Boundary conditions

The fluid problem has Neumann boundary conditions both in inlet and in outlet. By recalling the notation of Section 2.2, $p_{in}(t)$ and $p_{out}(t)$ are the pressure functions prescribed according to physiological values. In particular they represent the pressure inside the right ventricle $p_{RV}(t)$ and the pressure inside the pulmonary artery $p_{AR,PUL}(t)$, respectively, as already discussed in Section 2.6. These pressure profiles are derived from a simulation of the whole cardiovascular system, presented in Section 2.6. The simulations of the 0D model of the whole cardiovascular system have been performed imposing a time step $\Delta t = 10^{-4} \ s$ and a heartbeat period $T = 0.8 \ s$. The values of the parameters showing up in the model are the default ones present in [3]. The pressure plots that we obtain are reported in Figure 4.1.

We underline that the choice of an inlet pressure boundary condition is necessary to properly model the evolution of the pressure in the domain along the whole cardiac cycle and particularly the pressure jump across the closed leaflets at diastole.

$$p_{in} = p_{RV}, \ p_{out} = p_{AR,PUL} \qquad \Delta p = p_{in} - p_{out} = p_{RV} - p_{AR,PUL}$$
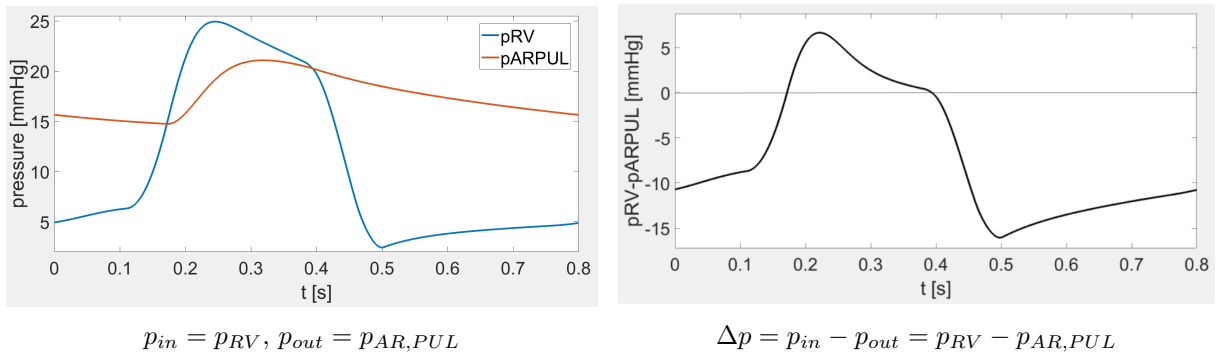
Figure 4.1: Boundary conditions. The pressure functions are obtained from the 0D circulation model of the whole cardiovascular system, stand-alone solved, and are imposed as boundary conditions of the 3D fluid problem.

The values of the resistances characterizing the diodes that represent the cardiac valves in

the 0D circulation model are set to the default ones present in [3], R_{max}=75006.2 $mmHg$ s mL^{-1} and R_{min}=0.0075 $mmHg$ s mL^{-1}, according to the notation of Section 2.6.

The validity of these values have been proved by performing a Sensitivity Analysis of the fluid dynamics of the pulmonary artery with respect to the diode parameters R_{min} and R_{max} of the pulmonary valve.

Sensitivity Analysis

The goal is to modify the default values of R_{min} and R_{max} of the pulmonary valve and to study how these variations affect the profiles of p_{RV} and $p_{AR,PUL}$ and afterwards the 3D fluid dynamics of the pulmonary artery.

The first step of this analysis consists in performing simulations of the 0D model of the whole cardiovascular system for different values of R_{min} and R_{max} of the pulmonary valve, then we extract the values of the pressure in the right ventricle and in the pulmonary artery and finally we impose them as inlet and outlet conditions of the 3D model of the pulmonary artery. We assume that the pulmonary valve leaflets, immersed in the pulmonary artery, have a prescribed dynamics. In particular the valve opening and closing phases are instantaneous: the leaflets open when p_{RV} gets higher than $p_{AR,PUL}$ and close to avoid backflow, reproducing the physiological behavior. Moreover we consider the valve dynamics characterized by the so-called on-off behavior: the surface appears and disappears instantaneously in time, it does not move but disappears as soon as it reaches half of the total opening.

The geometry of the pulmonary artery considered belongs to Patient 2.
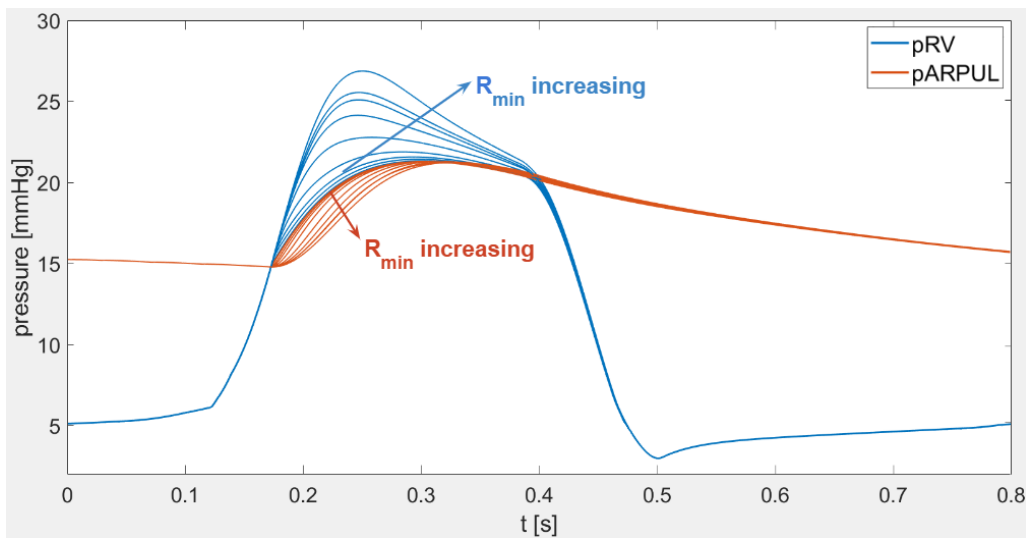
Figure 4.2: Pressure plots for different values of R_{min}.

First we have kept R_{max} fixed to the default value, R_{max}=75006.2 $mmHg$ s mL^{-1}, and we have varied $R_{min} \in \{0, 0.0001, 0.0005, 0.001, 0.002, 0.004, 0.006, 0.0075, 0.008, 0.1\}$ $mmHg$ s mL^{-1}. The behavior of the pressure profiles, arising from the 0D model of the whole cardiovascular system, is the following one. As R_{min} increases, the distance between the pressure curves increases, in particular p_{RV} increases, as highlighted in Figure 4.2. If $R_{min} > 0.008$ $mmHg$ s mL^{-1}, p_{RV} belongs to the characteristic range of values of the Pulmonary Arterial Hypertension; if $R_{min} < 0.006$ $mmHg$ s mL^{-1} the pressure values are again no longer physiological. Moreover the first pressure gradient inversion always occurs in the same time instant ($t = 0.1718$ s), while the second one occurs later in time for larger values of R_{min} (Figure 4.3).
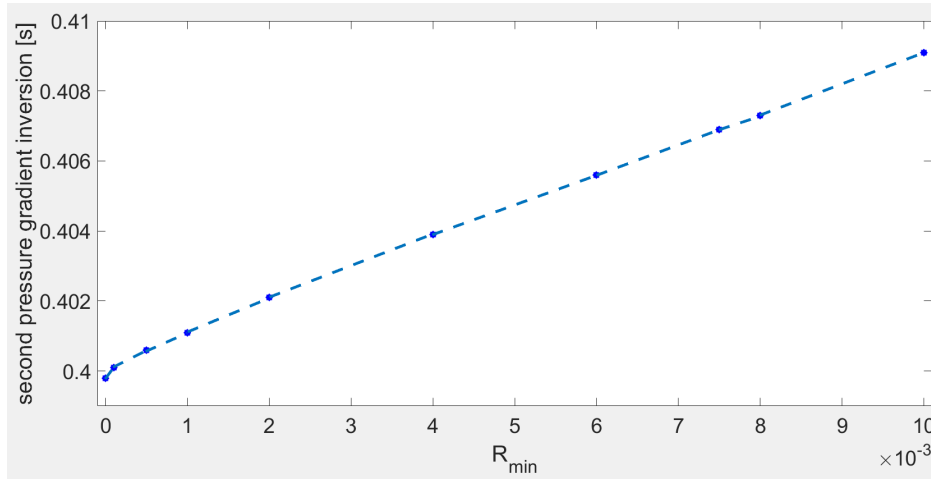
Figure 4.3: Dependence of the second pressure gradient inversion instant on R_{min}.

The fluid dynamics of the pulmonary artery is influenced as follows. As R_{min} increases the inlet flow rate, or equivalently the inlet velocity, increases too (Figure 4.4). This is in accordance to the presence of a larger pressure gradient between inlet and outlet.
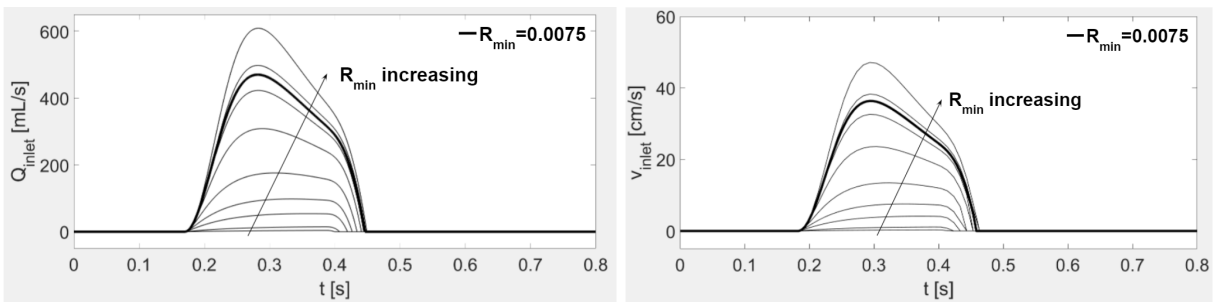
Figure 4.4: Inlet flow rate (*left*) and inlet velocity (*right*) for different values of R_{min}.

If $R_{min} < 0.006$ mmHg s mL^{-1} or $R_{min} > 0.008$ $mmHg$ s mL^{-1} the values of flow rate and

velocity are not physiological. The inlet flow rate, or the inlet velocity, becomes positive in the same time instant for all cases, while it reverses later in time for larger values of R_{min} (Figure 4.4). This is consistent with what happens for pressures.

Afterwards we have kept R_{min} fixed to the default value, R_{min}=0.0075 $mmHg\ s\ mL^{-1}$, and we have varied $R_{max} \in \{1000, 3000, 4000, 5000, 10000, 75006.2, 80000, 100000, 500000\}$ $mmHgsmL^{-1}$. From Figure 4.5, where we have reported the pressure plots for some values of R_{max}, we observe that if R_{max} is sufficiently large ($R_{max} > 10000\ mmHg\ s\ mL^{-1}$) the pressure values are physiological. On the contrary, if R_{max} is not sufficiently large there are two possibilities: if $3000 < R_{max} \leq 10000\ mmHg\ s\ mL^{-1}$ the pressure plots show some oscillations, while if $R_{max} \leq 3000\ mmHg\ s\ mL^{-1}$ the pressure values are n.a.n.. We also notice that, for $3000 < R_{max} \leq 10000\ mmHg\ s\ mL^{-1}$, as R_{max} decreases the first pressure gradient inversion occurs before in time and the second one later in time (Figure 4.6).
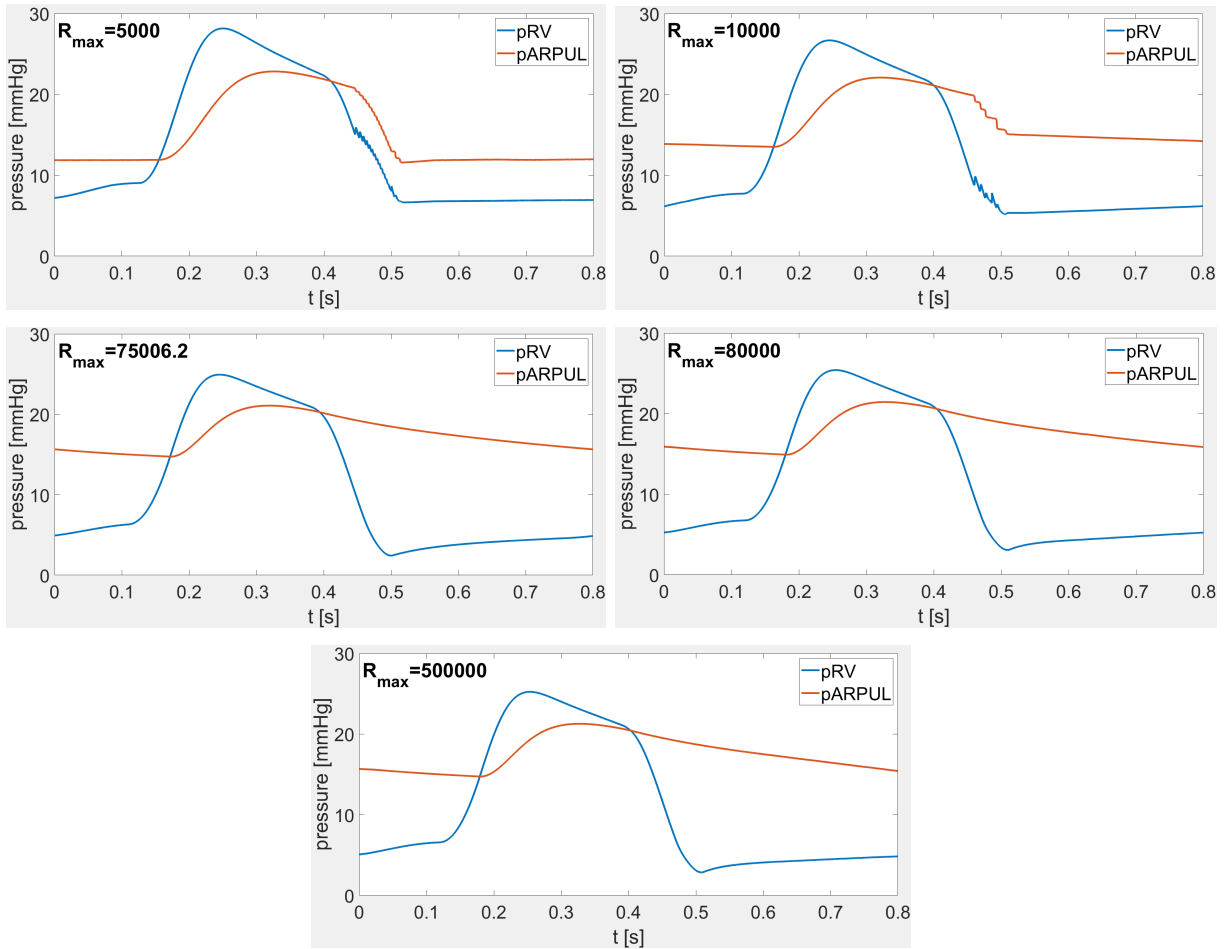
Figure 4.5: Pressure plots for different values of R_{max}.

In Figure 4.7 we can observe the 3D fluid dynamics of the artery: if R_{max} is sufficiently large $(R_{max} > 10000 \; mmHg \; s \; mL^{-1})$ the inlet flow rate, or equivalently the inlet velocity, shows physiological values; if R_{max} is too small, but still the pressures are not n.a.n., the values of the inlet flow rate, or the inlet velocity, are not physiological.
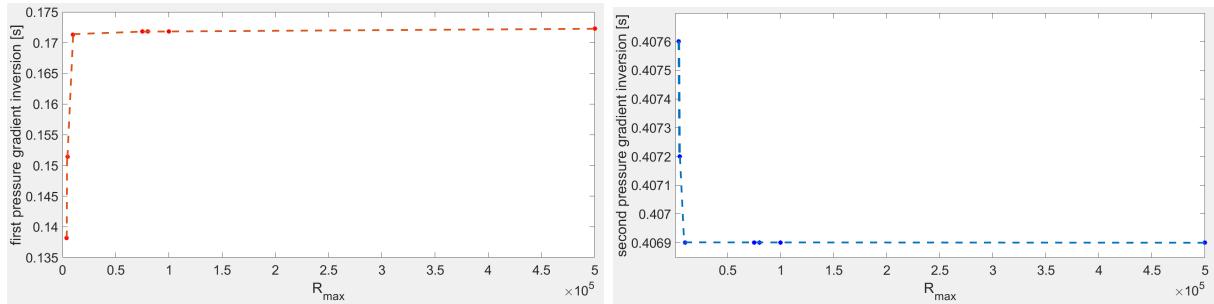
Figure 4.6: Dependence of the first (*left*) and second (*right*) pressure gradient inversion instants on R_{max}.

Moreover as R_{max} decreases, the inlet flow rate, or the inlet velocity, becomes positive before in time and it reverses later in time, consistently with the behavior of inlet and outlet pressures.
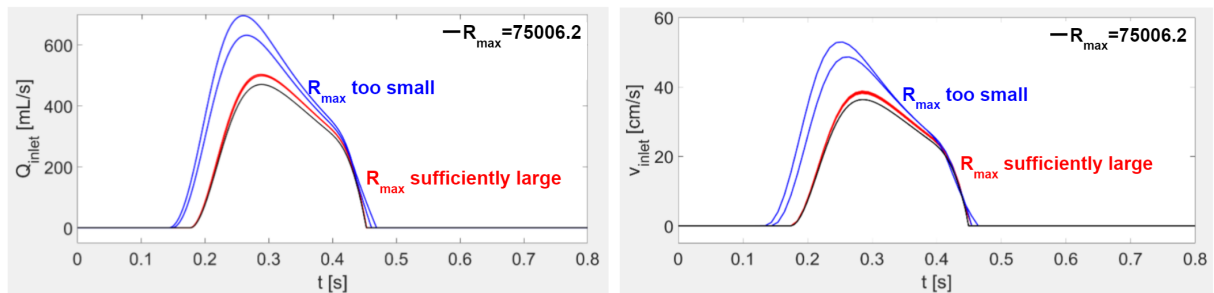
Figure 4.7: Inlet flow rate (*left*) and inlet velocity (*right*) for different values of R_{max}.

Summing up, R_{min} has to be large in order to allow an adequate pressure difference between outlet and inlet and a sufficiently high inlet velocity, in accordance with literature values, but not too large to end up in the Pulmonary Arterial Hypertension pressure range. Furthermore if R_{max} is small, pressure and inlet velocity values do not belong to the physiological ranges or even there are numerical instabilities.

The default values for R_{min} and R_{max} belong to the physiological range and can be appropriately tuned to possibly obtain better results depending on the application of interest.

A recap of all the possible cases is reported in Table 4.1.

	$R_{min} < 0.006\ mmHg\ s\ mL^{-1}$	not physiological
$R_{max}{=}75006.2\ mmHg\ s\ mL^{-1}$	$0.006\ mmHg\ s\ mL^{-1} \leq R_{min} \leq 0.008\ mmHg\ s\ mL^{-1}$	physiological
	$R_{min} > 0.008\ mmHg\ s\ mL^{-1}$	not physiological
	$R_{max} \leq 3000\ mmHg\ s\ mL^{-1}$	instability
$R_{min}{=}0.0075\ mmHg\ s\ mL^{-1}$	$3000\ mmHg\ s\ mL^{-1} < R_{max} \leq 10000\ mmHg\ s\ mL^{-1}$	not physiological
	$R_{max} > 10000\ mmHg\ s\ mL^{-1}$	physiological

Table 4.1: Sensitivity Analysis of fluid dynamics in the pulmonary artery with respect to the diode parameters R_{min} and R_{max} of the pulmonary valve.

4.3. Scenario *Trial*

In this section we do not consider the lumped-parameters model for the valve dynamics, but a prescribed valve motion law.

This simplified valve dynamics allows to perform a preliminary analysis in order to verify that the pre-processing and mesh generation steps have been performed correctly. This condition is achieved through the comparison between our results and the physiological ones, specifically benchmark quantities of velocity and pressure.

We focus on the systolic phase, starting our simulations just before the valve opening, when the valve is still closed, and on the first part of the diastole, when the valve comes back to its closed configuration.

As for the lumped-parameters valve model of Section 2.3, also in this case the displacement of the leaflets $\mathbf{d}_\Gamma$ can be decomposed into two contributions (equation (2.8)): the opening field $\mathbf{g}$, which is a datum and accounts for the spatial dependence, and the opening coefficient c, which considers the temporal dependence. However, here the opening coefficient c is not solution of a structure problem for the valve, as in the lumped-parameters model, but it is decided a priori in order to simulate the physiological behavior. In particular, by recalling the notation of Section 2.3, a proper opening field $\mathbf{g}$ has been introduced on the leaflets, i.e. the displacement array of Section 3.2.3, so that the surface $\Gamma_{open} = \{\mathbf{x} = \widehat{\mathbf{x}} + \mathbf{g}(\widehat{\mathbf{x}}),\ \widehat{\mathbf{x}} \in \widehat{\Gamma}\}$, corresponding to an opening coefficient $c = 1$, represents the physiological open valve configuration. In order to simulate the physiological behavior we impose the time instants in which the valve opens and successively closes (Table 4.2). The valve leaflets motion between the closed/open and open/closed configurations is linear and occurs in one time step. More in detail, the valve opening and closing stages are instantaneous: the valve leaflets open when p_{RV} becomes higher than $p_{AR,PUL}$ and close to avoid backflow. The instantaneous opening and closing stages neglect the transitory, intermediate effects between the two configurations.

	Patient 1	Patient 2
opening valve time instant	0.1718 s	0.1718 s
closing valve time instant	0.4505 s	0.4474 s

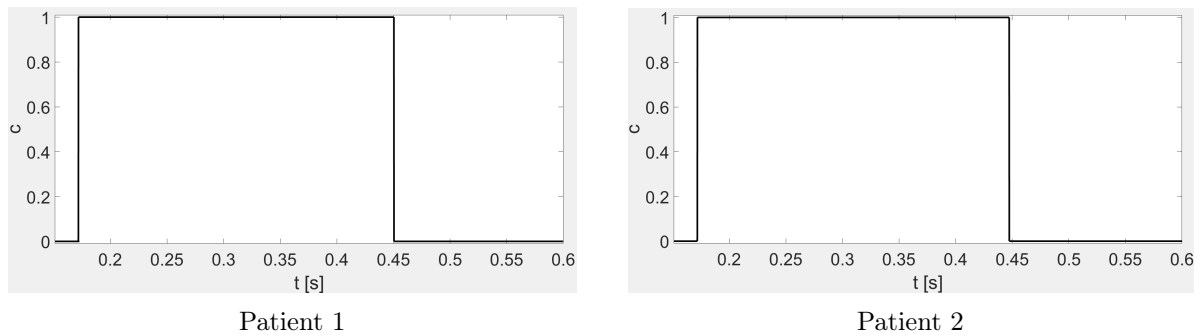Table 4.2: Prescribed opening and closing valve time instants in Scenario *Trial*.

Patient 1   Patient 2

Figure 4.8: Prescribed opening coefficient c in Scenario *Trial*.

The opening coefficient plots reproduce the physiological behavior (Figure 4.8). Indeed both the duration of the systole and the delay of the valve closing (see Table 4.2) with respect to pressure gradient inversion ($t = 0.4069\ s$) are consistent with the valve modeling literature.

As benchmark quantities we analyze, for both patients, the maximum velocity magnitude on a slice positioned just upwind the valve leaflets and the average pressure in a spherical control volume in correspondence of the artery bifurcation (Figure 4.9). The values obtained are comparable with those present in literature, see e.g. [52] for the velocity values and [90] for the pressure ones, and confirm the success of the pre-processing and mesh generation steps.

The small differences between the two patients concerning both the closing valve time instant and the velocity and pressure values are due to their different geometrical configurations.
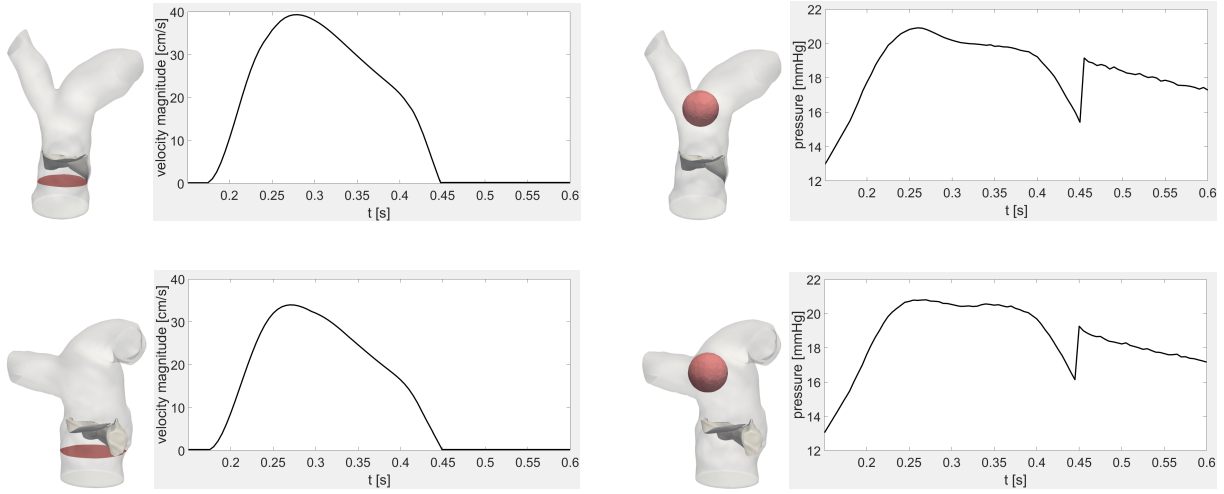
Figure 4.9: Maximum velocity magnitude on a slice upwind the valve (*left*) and pressure in a sphere at the artery bifurcation (*right*) of Patient 1 (*up*) and Patient 2 (*bottom*) in Scenario *Trial*.

4.4.   Calibration in the Scenario *Full FSI*

In this section we refer to the lumped-parameters model introduced in Section 2.3. In particular, the valve dynamics is described by equation (2.9), whose solution is the opening coefficient c.

As Section 4.3 we focus on the systolic phase and on the first part of the diastole, and we need the same definition of opening field $\mathbf{g}$ such that Γ_{open} corresponds to an opening coefficient $c = 1$ that represents the open valve.

In the following we will refer to the first contribution of the right hand side of equation (2.9) as the fluid stress jump term and to the second one as the elastic term. We recall the equation by highlighting the two terms in the boxes:

$$\ddot{c}(t) + \beta\dot{c}(t) = \boxed{\frac{\int_{\Gamma_t}\mathbf{f}(t,\mathbf{x})\cdot\mathbf{n}_\Gamma(t,\mathbf{x})d\mathbf{x}}{\int_{\Gamma_t}\rho_\Gamma\mathbf{g}(\mathbf{T}_t^{-1}(\mathbf{x}))\cdot\mathbf{n}_\Gamma(t,\mathbf{x})d\mathbf{x}}} - \boxed{\frac{\gamma\int_{\Gamma_t}[H(t,\mathbf{x}) - \widehat{H}(\mathbf{T}_t^{-1}(\mathbf{x}))]d\mathbf{x}}{\int_{\Gamma_t}\rho_\Gamma\mathbf{g}(\mathbf{T}_t^{-1}(\mathbf{x}))\cdot\mathbf{n}_\Gamma(t,\mathbf{x})d\mathbf{x}}}.$$

Our goal is to properly calibrate the model and successively to analyze the results of the computational hemodynamic simulations. The aim of the calibration procedure is to tune the parameters in order for the model to be able to reproduce the physiological behavior of the pulmonary circulation. We are first interested in obtaining the overall trend of valve motion: the initial configuration is the closed one, successively the leaflets show an opening phase, then they remain open and finally they close and maintain the closed configuration. In particular the valve leaflets open when the pressure upwind the

valve is higher than the pressure downwind and start closing as soon as the flow, after a decelerating phase, changes its direction. Moreover we want the opening and closing times and the duration of the systole to be comparable with those present in literature. We recall the valve modeling parameters, already discussed in Section 2.3, showing up in equation (2.9):

- damping β;

- elasticity γ.

Moreover we introduce two more parameters:

- density scaling factor;

- initial curvature term.

The first one takes into account the inertial properties of the leaflet and, representing the scaling between the valve leaflets density and the blood density, it is defined as the ratio between ρ_Γ and ρ; the second parameter is summed up to $\widehat{H}$ in order for the elastic force to always act in the same verse.
We have to properly tune both the value and the sign, that is related to the geometrical visualization of the leaflets.
We first study Patient 2 and afterwards we extend the obtained results to Patient 1.

4.4.1.   Patient 2

The first part of the calibration procedure for Patient 2 considers only the valve opening phase.
The correct trend of leaflets motion, already discussed in Section 4.4, is achieved by the identification of the correct sign of the parameters. On the other hand to obtain the correct times for the duration of the systole and the opening and closing stages we have to modify their values.
We discuss now the influence of each parameter on the opening phase:

- the presence of the damping term slows down the valve leaflets opening phase;

- an increasing of the elasticity parameter delays the opening phase: both the beginning and the end of the opening phase are delayed. See Figure 4.10a. Considering this result, we expect that an excessively large value makes the valve not able to open during systole;

- the density scaling factor has to be sufficiently large in absolute value in order to maintain the valve open after the opening phase. In other words the valve leaflets

must have a sufficient inertia to maintain the valve in its open configuration. If the
parameter value belongs to the appropriate range, we notice that as it increases, in
absolute value, the opening phase is slowed down. See Figure 4.10b;

- the initial curvature term is chosen in order for the elastic term to always have the
  same sign. Physically this means that the elastic force always acts in the same verse,
  that is pulling the leaflets to their closed configuration.
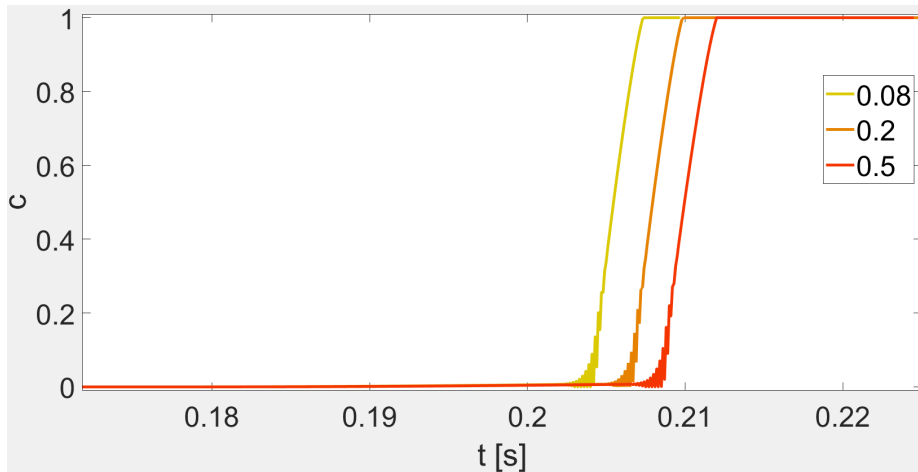
(a) elasticity
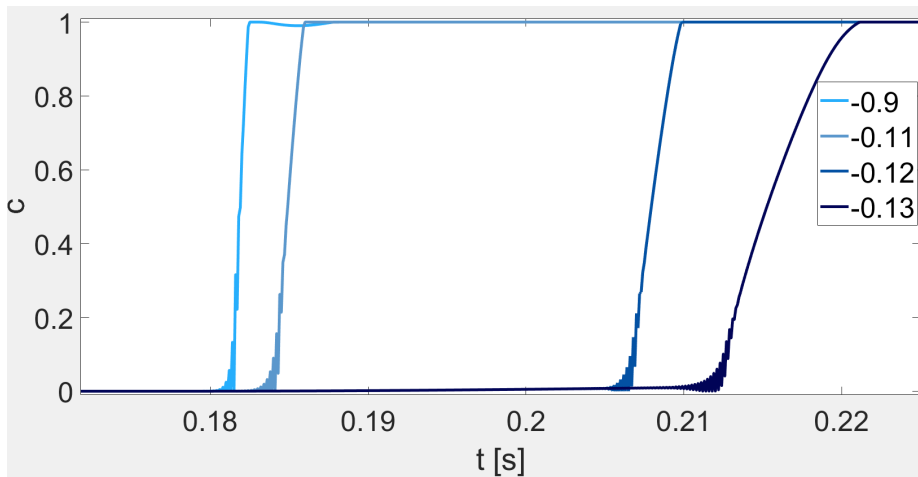
(b) density scaling factor

Figure 4.10: Sensitivity of the opening coefficient c with respect to the parameters elasticity
and density scaling factor for Patient 2.

The model is much sensitive to the elasticity parameter and to the density scaling factor,
small variations cause an appreciable difference in the opening coefficient c plot.
All these considerations are proceeded by a considerable number of simulations that sup-
port their validity.

In all cases we notice that the opening coefficient plot shows some oscillations that drive the actual opening stage. Indeed the opening stage can be divided into two parts: the first one, before the oscillations, very slow and the second one, after the oscillations, much faster.

Considering the values of the parameters that best reproduce the physiological valve opening phase (Table 4.3) we have simulated the whole systole.

damping	elasticity	density scaling factor	initial curvature term
$0.2\ s^{-1}$	$0.2\ N/m$	-0.12	$0.24\ m^{-1}$

Table 4.3: Model parameters calibrated for Patient 2.

The closing phase appears very slow (Figure 4.11, *blue curve*) and occurs when backflow is generated, violating the physiological behavior. Possible corrective strategies could be the adoption of an implicit coupling between fluid and valve models, instead of the explicit one considered in the present work, or the quasi-static approximation. The latter has been chosen in [31], in that case to avoid some numerical instability.

Thus, we consider the quasi-static approach, by imposing $\mathbf{u}_\Gamma = \mathbf{0}$. This approximation affects the fluid behavior since formally represents a violation of the physical adherence of the blood to the moving valve, but only in a limited manner, during the valve opening and closing stages. We do not observe any oscillations at all and the closing phase appears much faster such that the valve closes to avoid retrograde flow (Figure 4.11, *red curve*). In this case the absence of the oscillations allows the valve leaflets to maintain almost the same velocity along the whole opening phase. Physically, in the quasi-static approximation the flow perceives the valve as a bigger obstacle, with respect to the non approximated case. Indeed, in order to attain $\mathbf{u} = \mathbf{0}$ in the region where $|\varphi| < \epsilon$, the continuous function $\mathbf{u}$ must move from the flow values to $\mathbf{0}$ in a surrounding boundary layer, which thus artificially enlarges the effective obstacle that the leaflets represent to the flow.

Driven by the encouraging results obtained with the quasi-static approach, the idea was to consider also intermediate cases. This is achieved by modifying some lines of code in Life^x. The fluid velocity $\mathbf{u}$ in correspondence of the valve is the leaflets velocity $\mathbf{u}_\Gamma$, satisfying the no-slip condition, in the non approximated case; while it is $\mathbf{0}$ in the quasi-static approach. Between these two limit cases the fluid velocity $\mathbf{u}$ in correspondence of the valve can be approximated with a certain fraction of the leaflets velocity $\mathbf{u}_\Gamma$, velocity explicitly computed by the model. In particular, we consider a factor $\eta \in [0, 1]$ multiplying $\mathbf{u}_\Gamma$ in the fluid momentum equation. It could be thought as an extra parameter showing

up in the blood flow model. Moreover it could be interpreted as a re-calibration of the orifice area that in the other cases was overestimated or underestimated.

The leaflets velocity fraction, that allows to obtain good results in terms of opening and closing times (Table 4.4), is $\eta = 0.1$ (Figure 4.11, *brown curve*).
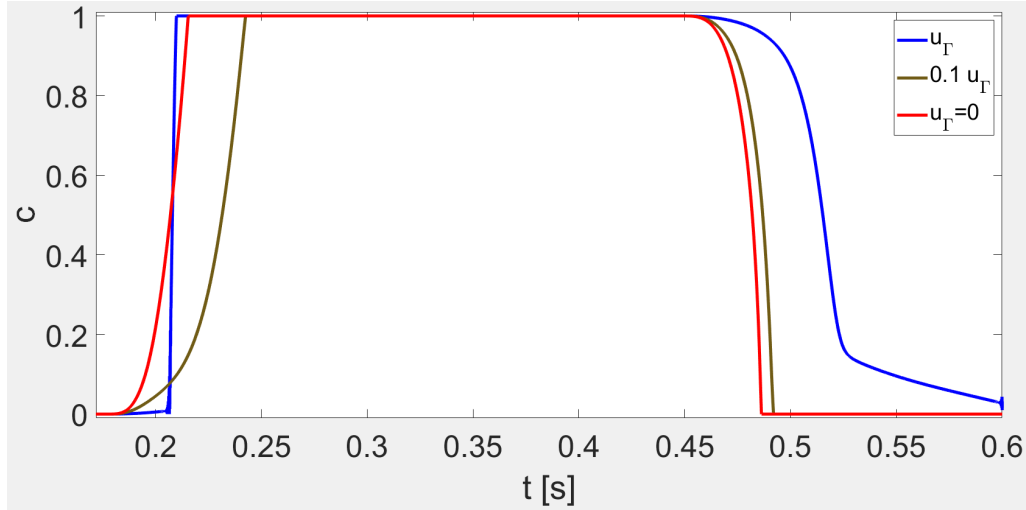

Figure 4.11: Opening coefficient c in Scenario *Full FSI* (Patient 2).

The opening and closing stages last 64 ms and 42 ms, respectively. We assume that they can be compared with the physiological times for the aortic valve, 76 ± 30 ms for the opening and 42 ± 16 ms for the closing [61], since the times concerning the pulmonary valve are not available, being until now not investigated.

valve opening time	$[0.1783\ s,\ 0.2426\ s]$
valve closing time	$[0.4496\ s,\ 0.4920\ s]$

Table 4.4: Opening and closing valve times in Scenario *Full FSI* (Patient 2).

The time evolution of the cross-valve pressure jump together with the pressure boundary conditions are reported in Figure 4.12. From Figure 4.11 and Figure 4.12 we observe that the leaflets remain closed until a minimal transvalvular pressure jump of about 1.6 $mmHg$ is developed. Successively they open up to their fully open position. In most part of the systole the valve remains in its fully open configuration, while the pressure jump progressively decreases. We notice that the pressure jump is definitely positive/negative during the opening/closing stage, whereas it remains below 2.5 $mmHg$ when the valve is fully open. Moreover the beginning of the closing phase at $t = 0.4496$ s is delayed with respect to the inversion of the macroscopic pressure jump, occurring at $t = 0.4069$ s. Such

behavior, consistent with the physiological one, is due to the inertia of both the blood flow and the valve, and it shows how the reconstruction of the local stress exchanged between the flow and the leaflets has a major impact on the valve dynamics. Indeed the closing phase starts when the fluid stress jump term returns negative (Figure 4.13).
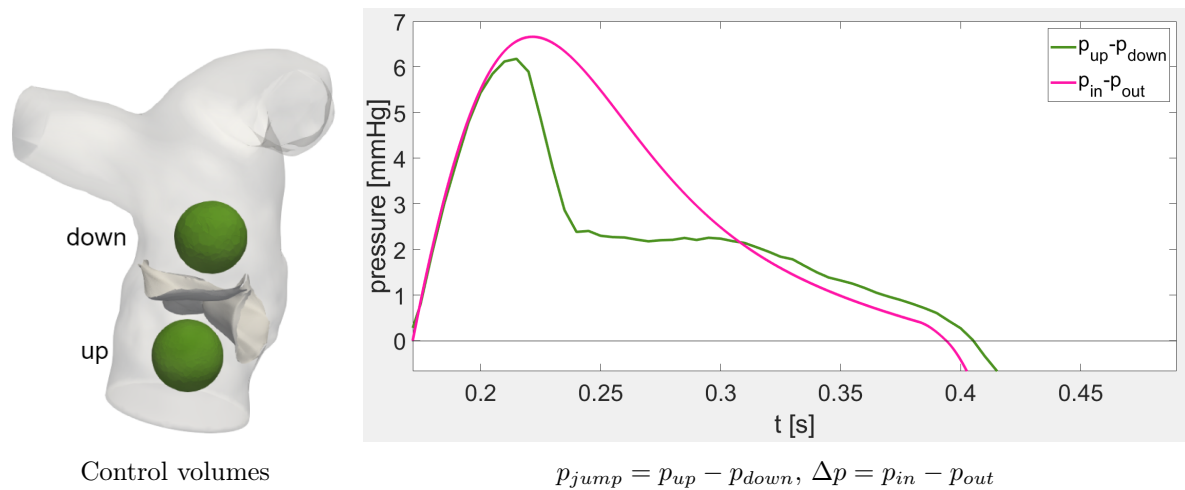

Control volumes

$$p_{jump} = p_{up} - p_{down}, \ \Delta p = p_{in} - p_{out}$$

Figure 4.12: Macroscopic pressure jump p_{jump} between two spherical control volumes (Patient 2). The overall pressure difference Δp is reported too, for comparison.
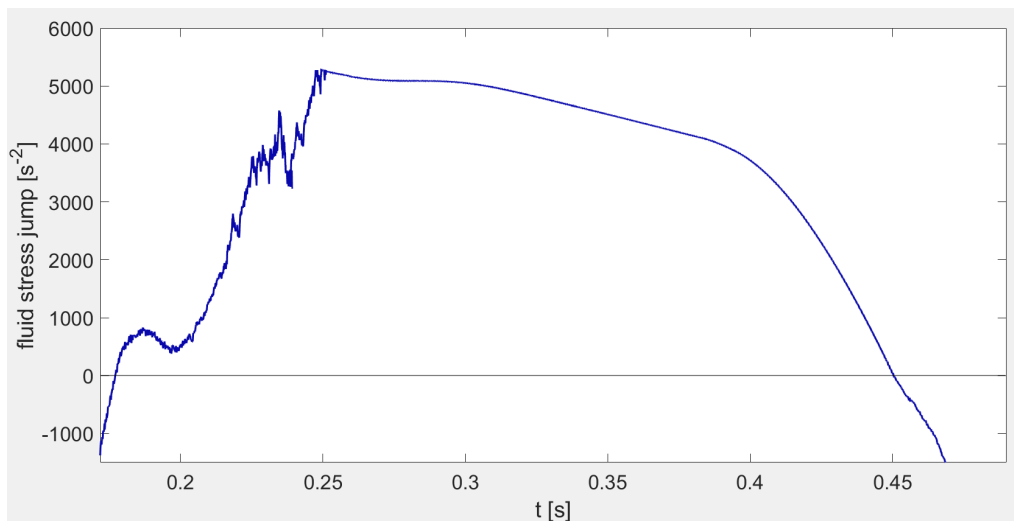
Figure 4.13: Transvalvular fluid stress jump (Patient 2).

4.4.2. Patient 1

Exploiting the results achieved for Patient 2, and thus skipping the calibration procedure step, we directly consider the whole systole for Patient 1.

We stress again the importance of the patient-specific geometry. Indeed the elasticity parameter γ has to be increased with respect to the one considered for Patient 2, in order to obtain for the two patients a similar valve opening instant (Table 4.5). We underline that increasing the elasticity term the opening phase is delayed, while the closing phase is brought forward.

damping	elasticity	density scaling factor	initial curvature term
$0.2\ s^{-1}$	$1\ N/m$	-0.12	$0.24\ m^{-1}$

Table 4.5: Model parameters calibrated for Patient 1.

With this geometry also, the inadequacy of the non approximated model is confirmed. Indeed, since the valve leaflets close when the flow is retrograde, there is not any guarantee for the valve to close and to maintain the closed configuration (Figure 4.14, *blue curve*). With Patient 1 geometry, $0.2\mathbf{u}_\Gamma$ is the approximation that better matches the physiological duration of valve opening and closing (Figure 4.14, *green curve*). This difference with respect to Patient 2 can be explained referring to the orifice size. In this case, since the geometry of Patient 1 has a smaller diameter, $0.2\mathbf{u}_\Gamma$ instead of $0.1\mathbf{u}_\Gamma$ allows to better estimate the orifice size. Indeed, as the quasi-static approximation artificially enlarges the obstacle that the immersed surface represents to the flow, by increasing the considered velocity leaflets fraction the effective orifice size increases too.
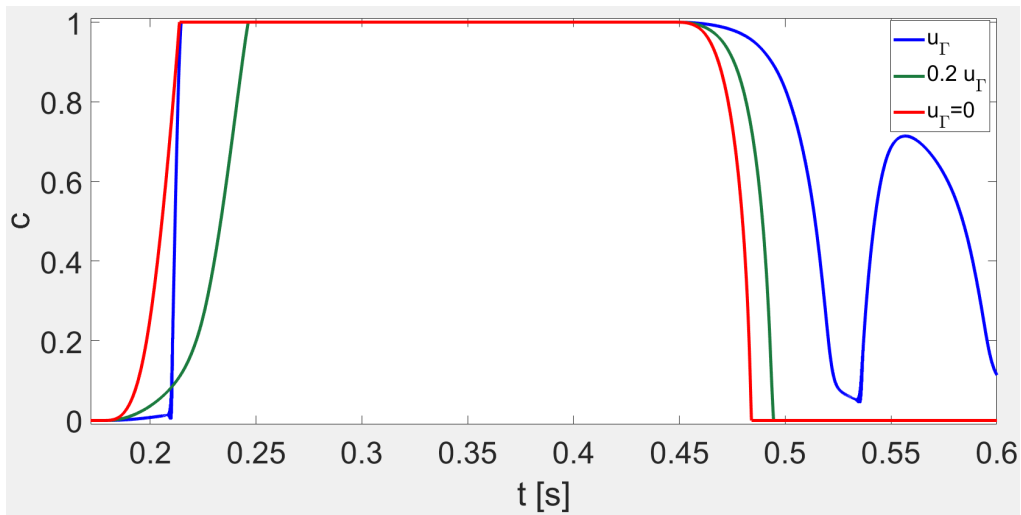
Figure 4.14: Opening coefficient c in Scenario *Full FSI* (Patient 1).

The opening and closing stages last $68\ ms$ and $47\ ms$, respectively (Table 4.6). These values lay in the physiological ranges, already reported for Patient 2.

valve opening time	$[0.1780 \ s, \ 0.2463 \ s]$
valve closing time	$[0.4478 \ s, \ 0.4945 \ s]$

Table 4.6: Opening and closing valve times in Scenario *Full FSI* (Patient 1).

The same analysis performed for Patient 2 has be repeated for Patient 1 and from Figure 4.15 and Figure 4.16 it is possible to draw similar considerations.
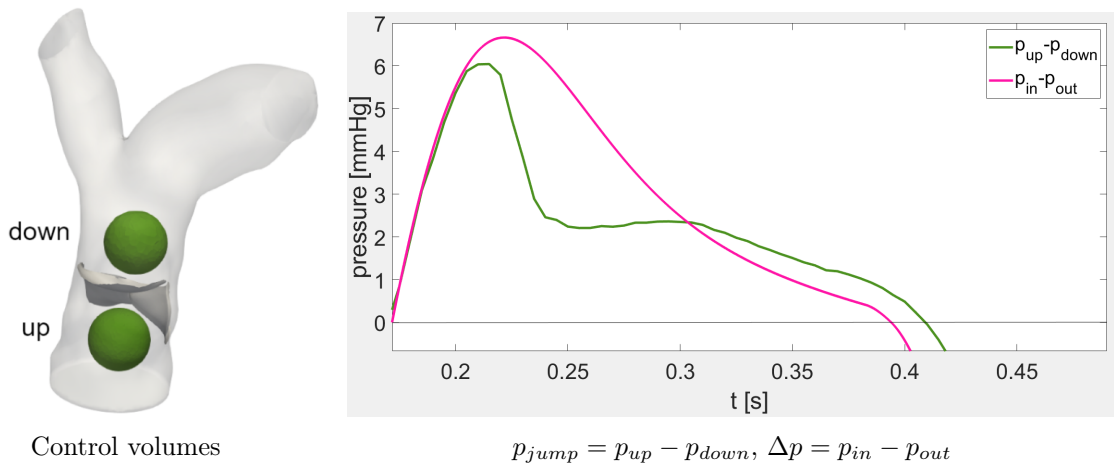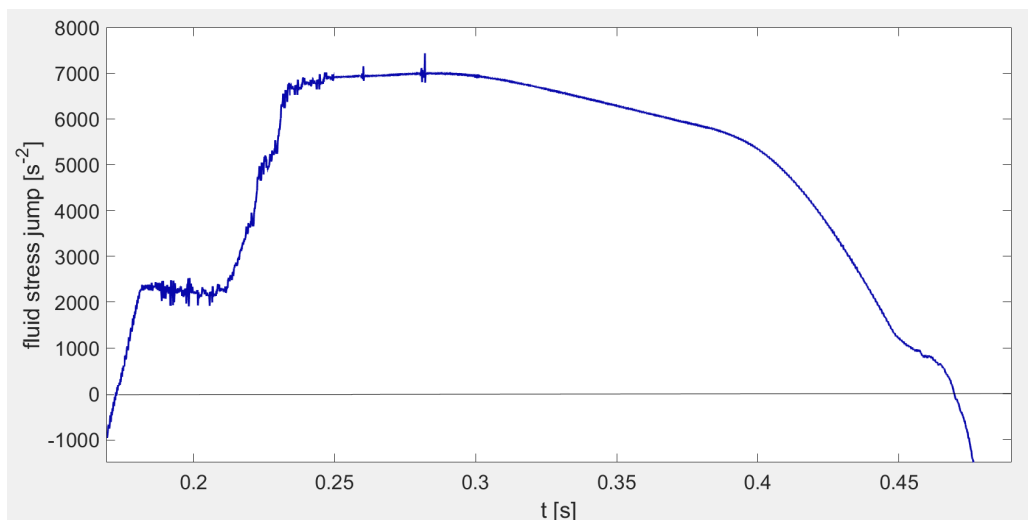

Control volumes

$$p_{jump} = p_{up} - p_{down}, \ \Delta p = p_{in} - p_{out}$$

Figure 4.15: Macroscopic pressure jump p_{jump} between two spherical control volumes (Patient 1). The overall pressure difference Δp is reported too, for comparison.

Figure 4.16: Transvalvular fluid stress jump (Patient 1).

4.5.   Results of the computational hemodynamic simulations in the Scenario *Full FSI*

We report the results of the computational hemodynamic simulations obtained with the model parameters and the approximation of the leaflets velocity that better reproduce the physiological behavior, discussed in Section 4.4.

Our goal is the visualization of the following fields:

- velocity field;

- pressure field;

- wall shear stress;

- Q-criterion.

The visualization on the 2D slices, reported in the following, have been obtained by cutting the arteries with two spheres to well capture their geometrical configurations (Figure 4.17). The choice of the sphere allows to cut perfectly the main, the left and the right pulmonary arteries. The leaflets are visible in transparency.

Patient 1   Patient 2
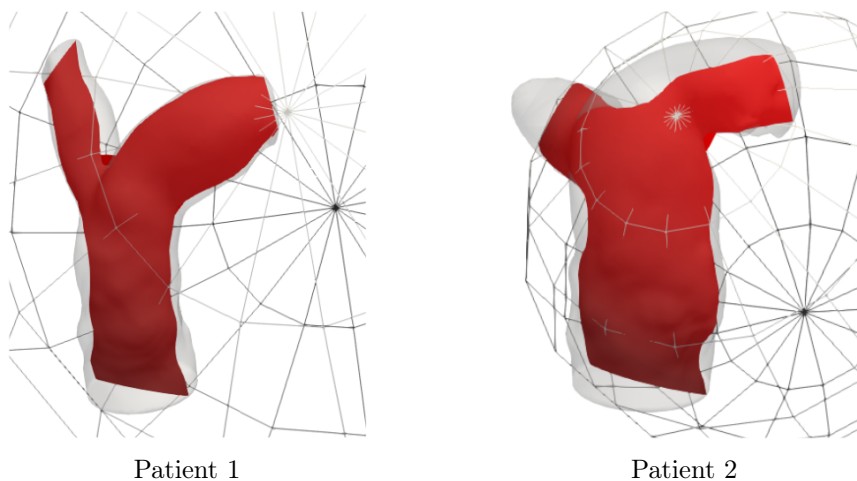
Figure 4.17: Slice visualization, obtained by cutting the arteries with two spheres.

Velocity field

We examine the velocity field on a slice of the pulmonary artery, in Figure 4.18 and in Figure 4.19 through streamlines.

The position of the slice allows to examine the deviation of the blood flow.

Patient 1

$t = 0.175\ s$ (closed valve) $t = 0.25\ s$ (valve just opened) $t = 0.31\ s$ (systolic peak)

$t = 0.445\ s$ (before valve closing) $t = 0.6\ s$ (closed valve)

Patient 2

$t = 0.175\ s$ (closed valve) $t = 0.245\ s$ (valve just opened) $t = 0.3\ s$ (systolic peak)

$t = 0.445\ s$ (before valve closing) $t = 0.6\ s$ (closed valve)

velocity magnitude (cm/s)

0.0e+00   20   40   60   80   1.0e+02
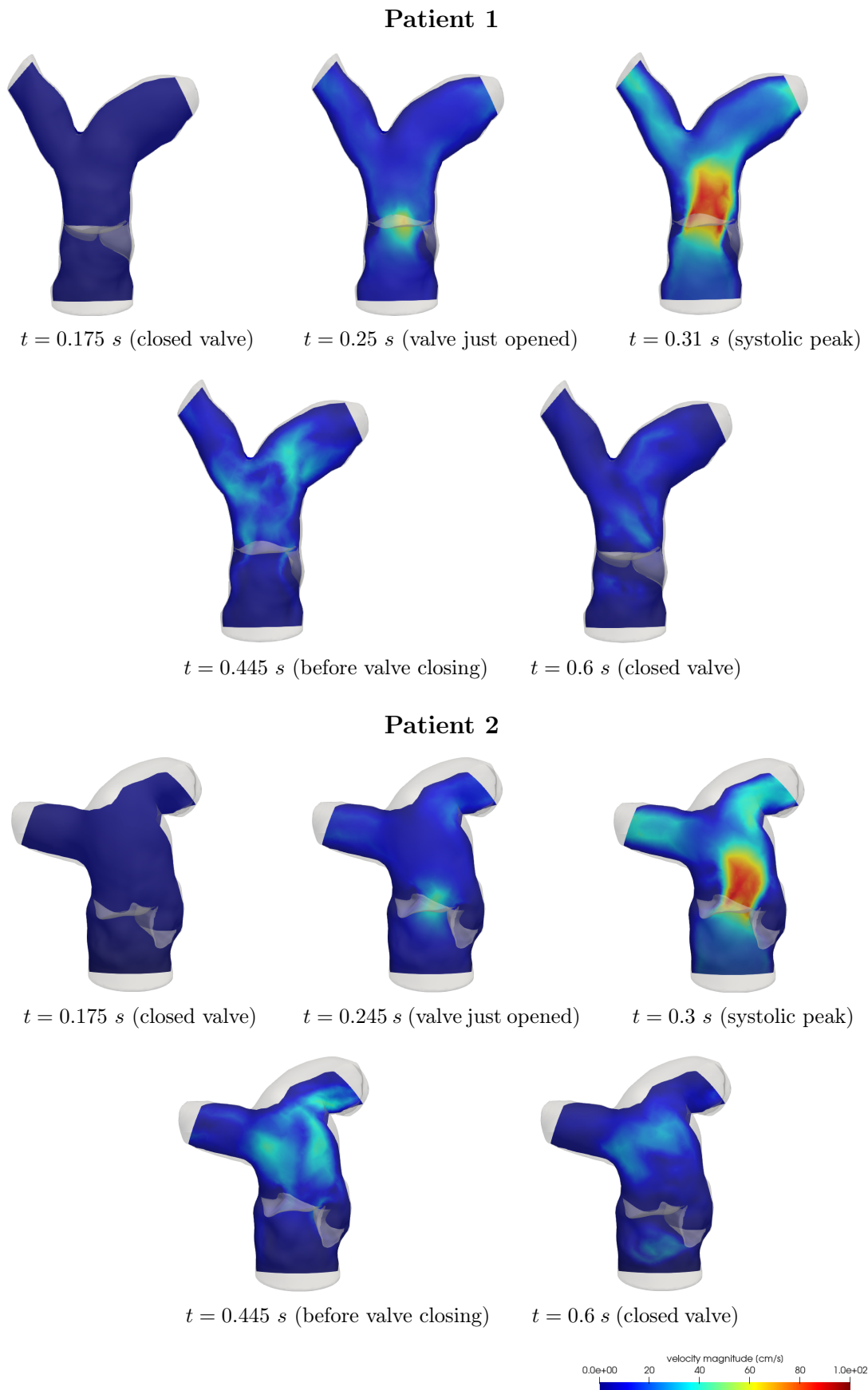
Figure 4.18: Velocity distribution at different times of Patient 1 (*top*) and Patient 2 (*bottom*).

We can notice that the flow direction is influenced by the patient-specific valve geometry that leads to an asymmetric jet impinging on the pulmonary artery wall. This phenomenon of flow deviation becomes appreciable when the valve has just reached the open position and becomes more considerable when the blood velocity reaches its maximum. We remark the importance of using the patient-specific geometry of the leaflets in order to visualize this behavior.

The streamlines visualization allows to analyze the pattern of the velocity field (Figure 4.19). In particular we notice a clear presence of coherent structures in the valve sinuses. They play a fundamental role in enhancing the efficiency of the blood supply and minimizing the blood backflow through the ventricle, ensuring a fast closure of the valve. Moreover some residual structures after the valve closing are also present, in this case both upstream and downstream the leaflets.

Patient 1

| $t = 0.25\ s$ | $t = 0.31\ s$ | $t = 0.445\ s$ | $t = 0.6\ s$ |
| (valve just opened) | (systolic peak) | (before valve closing) | (closed valve) |

Patient 2

| $t = 0.245\ s$ | $t = 0.3\ s$ | $t = 0.445\ s$ | $t = 0.6\ s$ |
| (valve just opened) | (systolic peak) | (before valve closing) | (closed valve) |

velocity magnitude (cm/s)
0.0e+00   20   40   60   80   1.0e+02
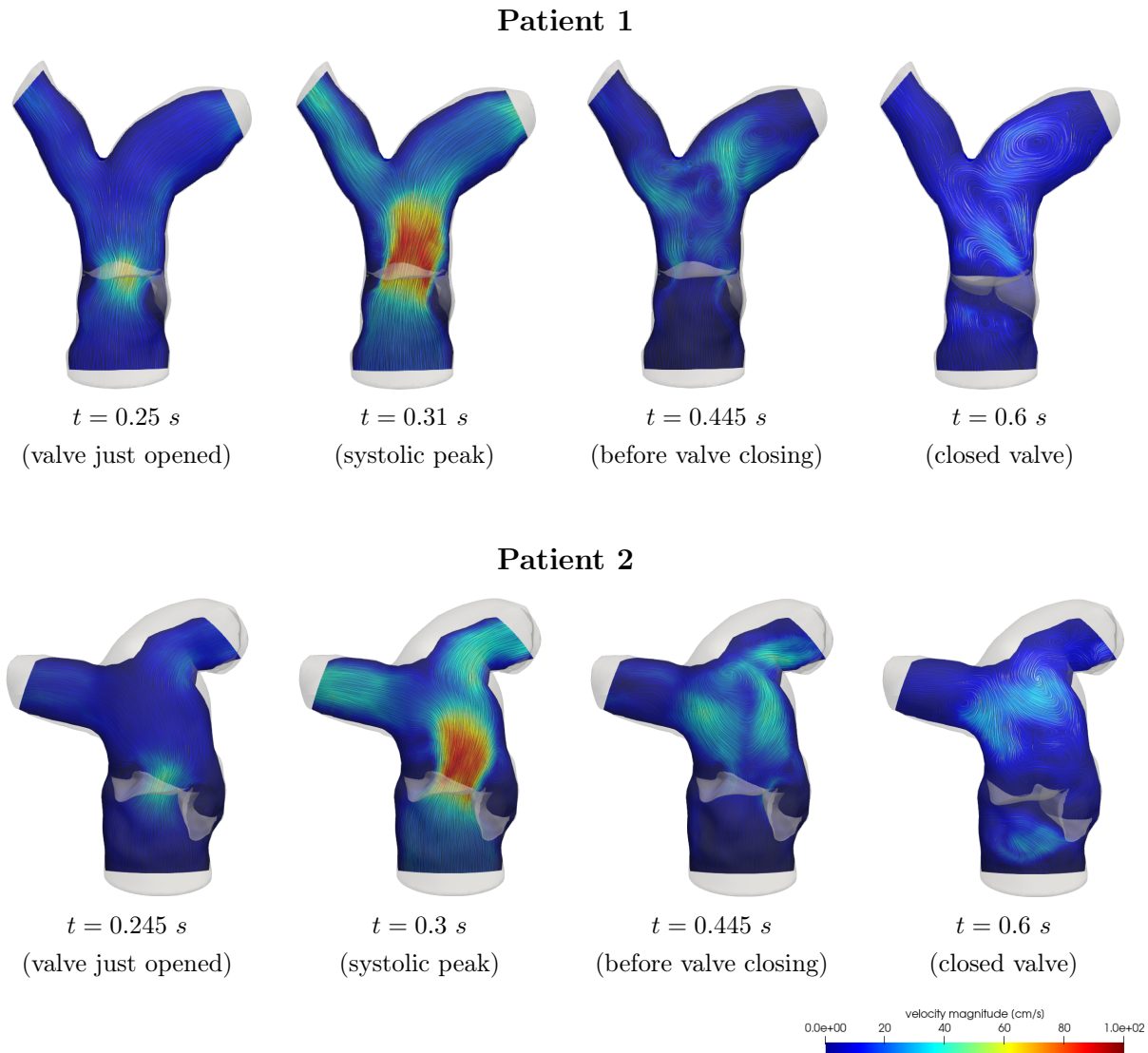
Figure 4.19: Velocity streamlines at different times of Patient 1 (*top*) and Patient 2 (*bottom*).

Figure 4.20 shows the leaflets velocity.

Patient 1

$t = 0.175\ s$ (closed valve)　　　$t = 0.225\ s$ (opening valve)　　　$t = 0.31\ s$ (open valve)

$t = 0.48\ s$ (closing valve)　　　$t = 0.6\ s$ (closed valve)

Patient 2

$t = 0.175\ s$ (closed valve)　　　$t = 0.22\ s$ (opening valve)　　　$t = 0.3\ s$ (open valve)

$t = 0.475\ s$ (closing valve)　　　$t = 0.6\ s$ (closed valve)
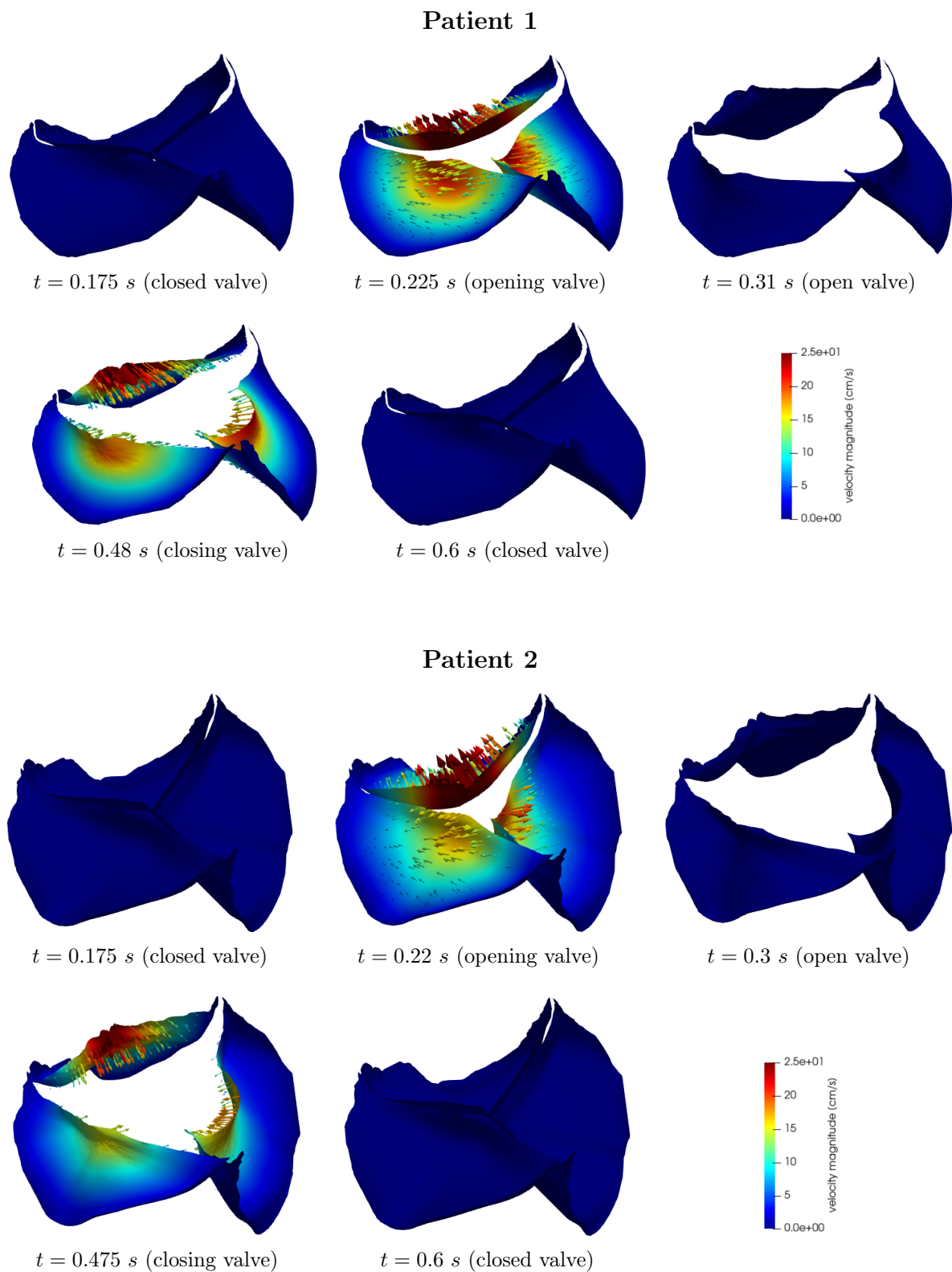
Figure 4.20: Leaflets velocity at different times of Patient 1 (*top*) and Patient 2 (*bottom*).

Pressure field

In this section we study the pressure distribution, both in the ϵ-neighborhood of the valve (Figure 4.21) and on a slice (Figure 4.22).

Patient 1

$t = 0.175\ s$ (closed valve) $t = 0.25\ s$ (valve just opened) $t = 0.31\ s$ (systolic peak)

$t = 0.445\ s$ (before valve closing) $t = 0.6\ s$ (closed valve)

Patient 2

$t = 0.175\ s$ (closed valve) $t = 0.245\ s$ (valve just opened) $t = 0.3\ s$ (systolic peak)

$t = 0.445\ s$ (before valve closing) $t = 0.6\ s$ (closed valve)
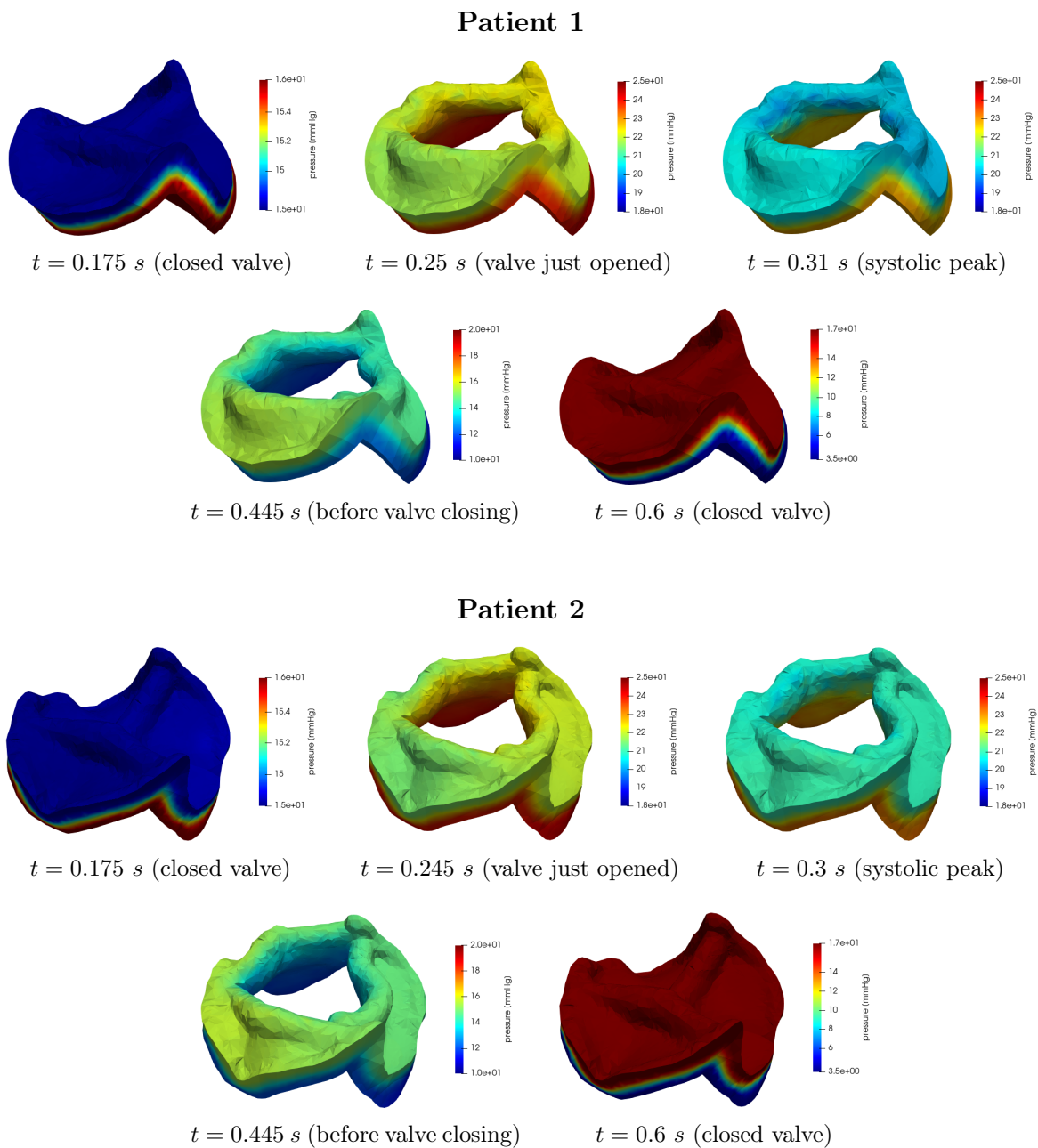
Figure 4.21: Pressure distribution across the valve at different times of Patient 1 (*top*) and Patient 2 (*bottom*).

Patient 1

$t = 0.175\ s$ (closed valve $t = 0.25\ s$ (valve just opened) $t = 0.31\ s$ (systolic peak)

$t = 0.445\ s$ (before valve closing) $t = 0.6\ s$ (closed valve)

Patient 2

$t = 0.175\ s$ (closed valve) $t = 0.245\ s$ (valve just opened) $t = 0.3\ s$ (systolic peak)

$t = 0.445\ s$ (before valve closing) $t = 0.6\ s$ (closed valve)
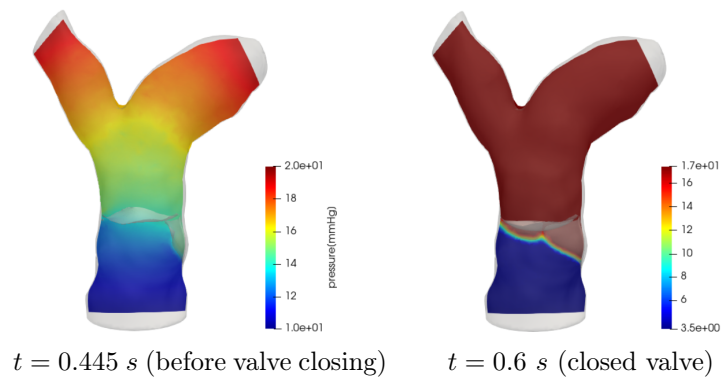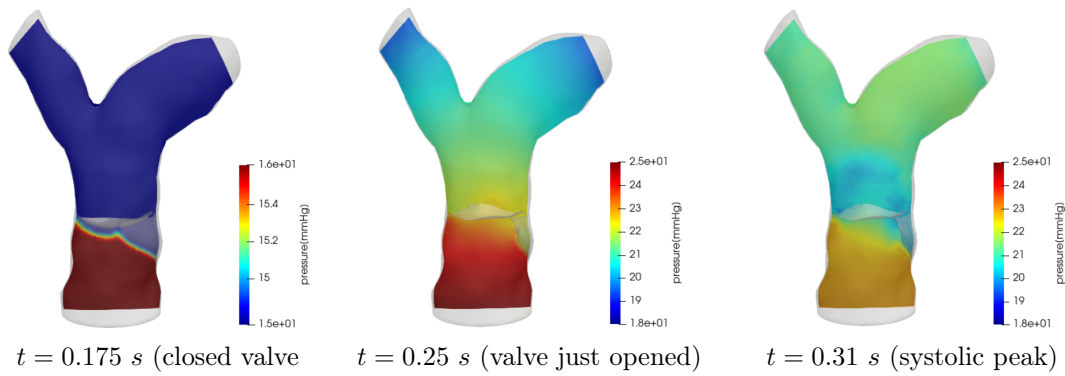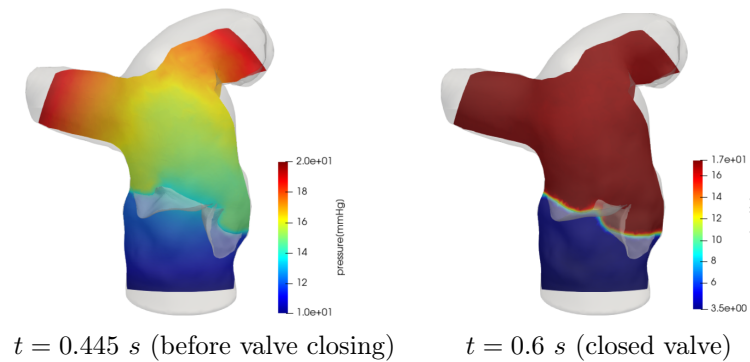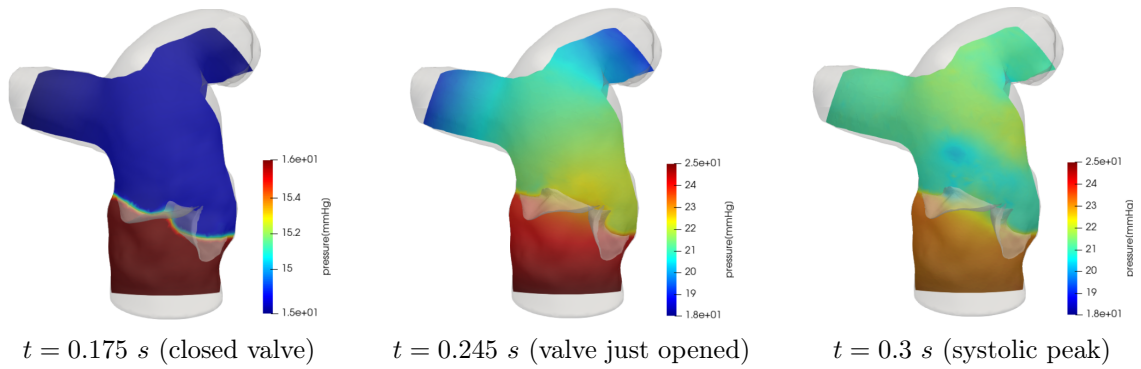
Figure 4.22: Pressure distribution on a slice at different times of Patient 1 (*top*) and Patient 2 (*bottom*).

When the valve is closed, the whole pressure gradient develops within the 2ϵ valve thickness, while outside that region the pressure is not affected by this high pressure jump. This shows the capacity of our method to reproduce the presence of the valve using the resistive RIIS term and its effectiveness in providing an obstacle to the flow.

When the valve is open, especially when the velocity in the region of the valve reaches its maximum, the pressure in the right ventricle and in the valve sinuses is almost homogeneous, with the highest pressure gradient localized among the leaflets, while downstream to the valve the deviation of the flow, already discussed, induces a corresponding pressure peak near the wall and, as a result, a depression zone in the central part of the main pulmonary artery.

Wall shear stress

We introduce the wall shear stress (WSS) to measure the tangential viscous forces magnitude exerted by the blood in motion on the vessel walls Σ_{wall}.

It is defined as:

$$WSS = \mu\sqrt{\sum_{j=1}^{2}((\nabla\mathbf{u}\mathbf{n})\cdot\boldsymbol{\tau}^{(j)})^2} \quad \text{on } \Sigma_{wall},$$

where $\mathbf{u}$ is the fuid velocity, $\mathbf{n}$ is the normal unit vector, and $\boldsymbol{\tau}^{(j)}$ $j = 1, 2$ represent the tangential unit vectors.

We underline that WSS is a scalar function [72].
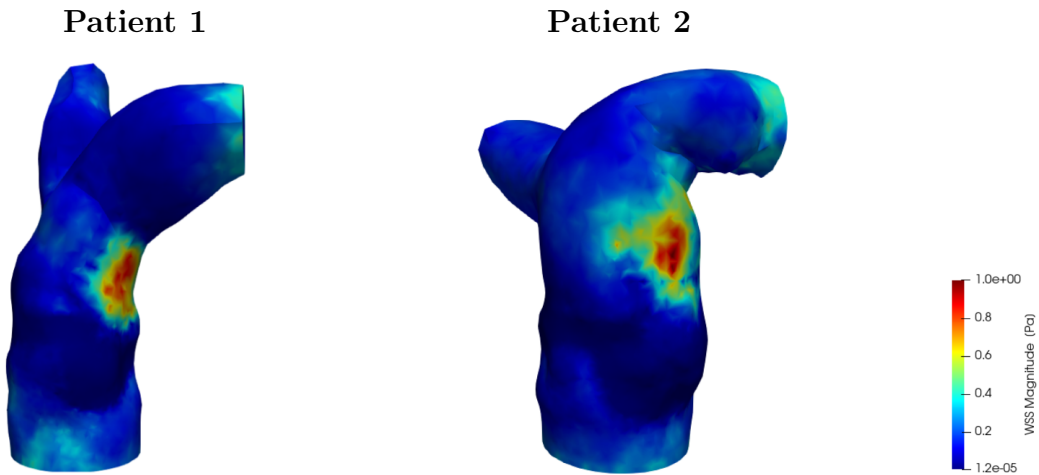
Figure 4.23: WSS of Patient 1 (*left*) and Patient 2 (*right*) at $t = 0.35\ s$.

Physically, the WSS indicates how fast the flow velocity increases when moving from a point on the vessel boundary to an adjacent point towards the normal direction to the wall [50].

In Figure 4.23 it is possible to observe a WSS almost null in correspondence on the valve, through which the blood flows not coming into contact with the artery wall, and a high value where the flow impacts upon the wall, emphasizing the shape of the jet blood already examined through the velocity distribution figures.

Q-criterion

We use the Q-criterion to visualize coherent vortex structures in the flow.

The Q function is:

$$Q = 0.5(|\mathbf{A}|_2 - |\mathbf{S}|_2),$$

where $\mathbf{A}$ and $\mathbf{S}$ are, respectively, the skew-symmetric and symmetric part of the velocity gradient.

To visualize the coherent vortex structures that appear in regions of a positive Q, we plot the iso-contours of Q, by selecting a suitable positive value [26].

In Figure 4.24 we can examine more clearly the vortex structures, already visualized through the streamlines (Figure 4.19).

When the valve opens a jet flow is generated, which leads to the formation of the classical ring coherent structures detaching from the tips of the leaflets. This underlines well organized laminar vortex structures in this phase of the cardiac cycle. During the central part of the systole, when the velocity magnitude reaches its peak value, the vortex structures are transported downwind in the artery and they break down in smaller structures just before the beginning of the closing phase. In this stage of the cardiac cycle the recirculation region increases its size and appears disorganized. These vortexes are physiological and contribute to the closure of the leaflets. Finally, after the valve has reached the closed position, residual flow recirculations can be appreciated both upstream and downstream to the valve.

Patient 1

$t = 0.225\ s$ (opening valve) $t = 0.25\ s$ (valve just opened) $t = 0.31\ s$ (systolic peak)

$t = 0.445\ s$ (before valve closing) $t = 0.6\ s$ (closed valve)

Patient 2

$t = 0.22\ s$ (opening valve) $t = 0.245\ s$ (valve just opened) $t = 0.3\ s$ (systolic peak)

$t = 0.445\ s$ (before valve closing) $t = 0.6\ s$ (closed valve)

velocity magnitude (cm/s)

0.0e+00   20   40   60   80   1.0e+02
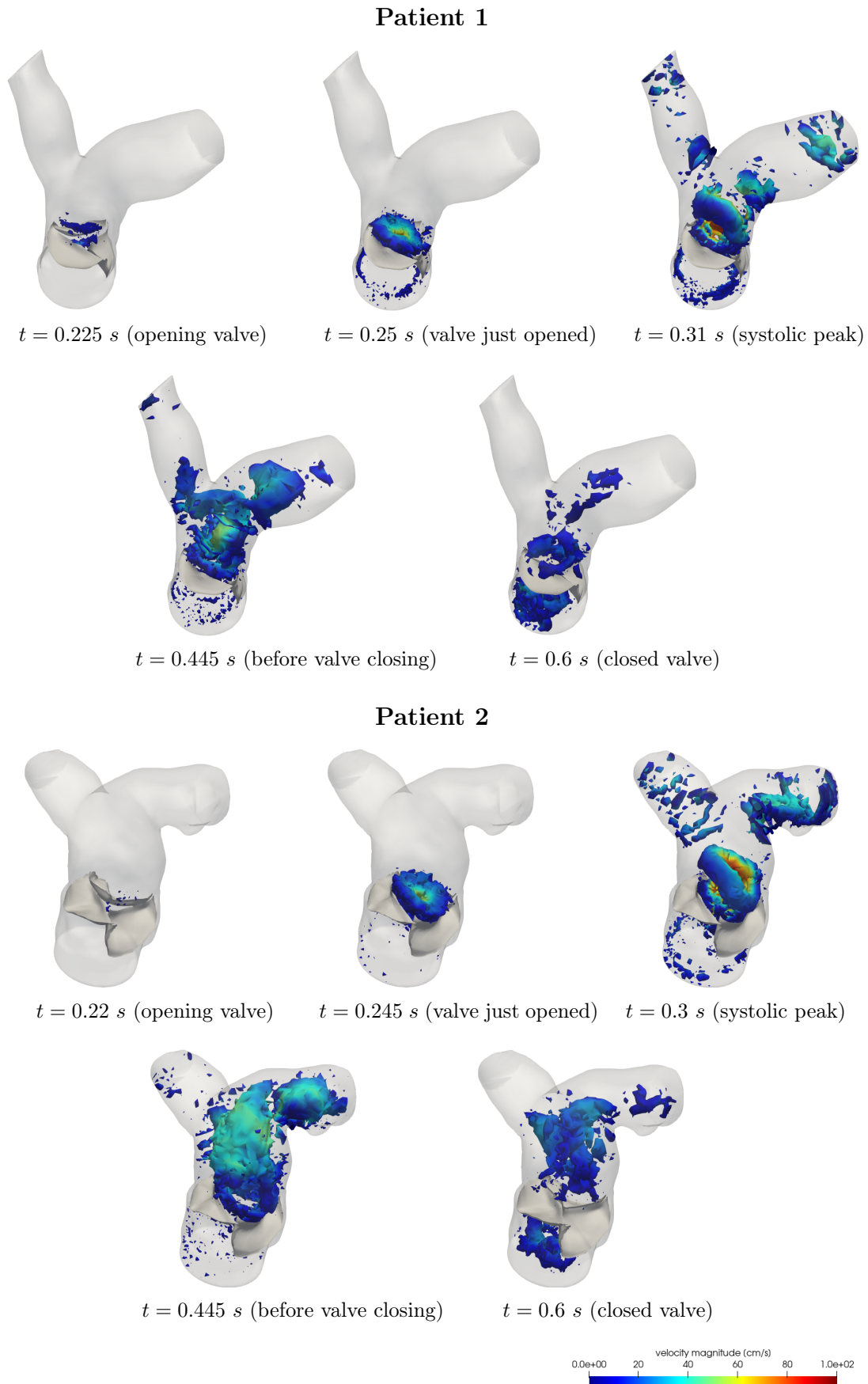
Figure 4.24: Q-criterion isosurfaces with $Q = 300\ s^{-2}$ colored with velocity magnitude at different times of Patient 1 (*top*) and Patient 2 (*bottom*).

4.6.   Final remarks

The resistive method, employed in this work, makes the valve perceived by the blood flow as an effective obstacle, being able to capture the sharp pressure jump across the valve without the necessity of meshing the leaflets.

The Scenario *Trial* allows to simulate the hemodynamics in the pulmonary artery with a computational cost which is smaller with respect to the one of the Scenario *Full FSI*. However, the prescribed instantaneous valve opening and closing stages neglect the transitory, intermediate effects between the closed and open configurations, which have to be taken into account in order to provide an exhaustive and complete description of the hemodynamics. Moreover, the resolution of the ordinary differential equation, describing the valve dynamics, in the Scenario *Full FSI*, states that the valve opens when a sufficiently large transvalvular pressure gradient develops, and not as soon as the upwind pressure is larger than the downwind one as it is prescribed in the Scenario *Trial*, better showing the physiological behavior.

The numerical simulations, in order to provide consistent hemodynamic results, in the Scenario *Full FSI*, have to be proceeded by a calibration phase in which the model parameters are appropriately tuned. This procedure, according to our experience, is not trivial, due to the sensitivity of the model. From our analysis, and with our patient-specific geometries, no value of the parameters allows to perfectly represent the valve motion trend. Thus, an approximation of the leaflets velocity, which allows to patient-specifically calibrate the orifice size, is needed in order to gain our goal of reproducing the physiological duration of the systole and of the valve opening and closing stages.

Finally the correct reconstruction of the artery and the appropriate positioning of the valve, which greatly influences the hemodynamics and can not be neglected, are of utmost importance to build our computational domain. These two steps allow to reproduce the physiological values of the main flow quantities, both the pressure values and the velocity pattern.

5 | Conclusions, limitations and future developments

In this work we have presented a reduced 3D-0D FSI model to describe the interaction between the blood flow in the pulmonary artery and the pulmonary valve.

The 3D fluid dynamics problem with the inclusion of the valve is solved by the Resistive Immersed Implicit Surface (RIIS) method. The presence of the valve is taken into account in the momentum equation of the Navier-Stokes equations by adding a resistive term, which weakly enforces the blood to adhere to the leaflets.

The blood flow dynamics is coupled with a 0D model which describes the valve dynamics reproducing its movement between the closed and open configurations. The model considers the flow-induced stress, the curvature-based elasticity and damping effects.

The reduced 3D-0D FSI model allows to describe the valve dynamics and the hemodynamics with a computational cost slightly higher than the effort of a CFD simulation with prescribed displacement; the additional cost lays in the assembly of the right-hand side of the ODE representing the valve dynamics, which can be done very efficiently on each quadrature node. Moreover the model explicitlely provides an expression for the leaflets velocity $\mathbf{u}_\Gamma$, without the discrete interpolation errors that would be introduced by a complex reconstruction procedure.

The remaining part of the cardiovascular system is accounted for by the boundary conditions which represent physiological values of pressure. The validity of the values of the parameters describing the pulmonary valve in the lumped-parameters model of the whole cardiovascular system is proved through a sensitivity analysis.

We have analyzed two different patients, affected by the tetralogy of Fallot, that after the Ross procedure in pediatric age and some years with pulmonary insufficiency, have undergone the implant of a prosthetic pulmonary valve. The data and the tomographic images are provided by the Niguarda Hospital, Milan. We have detailed the artery set-up and the valve reconstruction method in order to obtain the closed and open configurations of the patient-specific valve. We have not directly reconstructed the valve geometry from the CT, but we have adapted a generic valve model to our geometries considering the

position and the orientation of the valve sinuses, the stent and the commissures, derived from the images. This step is very thorny and challenging since the valve configuration greatly affects the blood dynamics.

We review the principal results:

- the pre-processing procedure succeeds in the reconstruction of the patient-specific pulmonary valve leaflets in both open and closed positions and for both patients;

- the calibration procedure of the 0D valve model, according to our experience not trivial at all due to the sensitivity of the model to the variation of the parameters, succeeds in reproducing the valve motion and consequently the associated hemodynamics;

- the RIIS method is able to provide an effective obstacle to the blood flow and to capture the sharp pressure jump across the valve without the necessity of meshing the leaflets;

- in order to obtain physiological results, a further model assumption is necessary, which allows to modulate the intensity of the leaflets velocity. Indeed, since considering the velocity of the blood flow in correspondence to the valve equal to the valve velocity itself causes the presence of some oscillations in the valve opening coefficient plot and a non physiological valve closure stage, the idea is to apply an approximation. In particular, considering only a certain fraction of the leaflets velocity, instead of the whole, allows to restore the correct trend of valve motion, in terms of physiological times of the valve opening and closing stages, as well as pressure and velocity values comparable with those reported in literature. This approximation can be interpreted as an extra parameter in the Navier-Stokes equation and a re-calibration of the orifice size. Physically, it violates the adherence of the blood to the moving valve, but only in a limited time during the opening and closing stages and in a limited space;

- the patient-specificity of the model is of utmost importance, as showed especially by the results concerning the velocity field. Indeed the variability among different patients can be captured only considering the patient-specific pulmonary artery geometry and the patient-specific leaflets in the correct position.

We now address the main limitations:

- the assumption of rigid artery walls for the pulmonary artery, that could be responsible for slightly overestimations of flow quantities. The interaction between fluid and pulmonary wall structure can be easily considered by extending the RIIS

approach to a fluid-structure model of the pulmonary artery;

- the pressure values imposed as outlet boundary condition, that should not be equal, since the two branches of the pulmonary artery have different shapes and sizes. Thus, for more accurate simulations we would need more precise pressure values.

Finally we discuss the possible developments of this work that can be undertaken in order to further enhance the proposed model for the study of different scenarios:

- the adoption of an implicit coupling between the blood and valve dynamics, instead of the explicit one considered in the present work;

- a further investigation on the leaflets velocity approximation or alternative strategies;

- the application of other 3D-0D FSI models to the same framework or the same model but to other patient-specific geometries, in physiological or different pathological conditions concerning both the artery geometry and the valve;

- the extension, being the model derived from a local force balance, to the atrio-ventricular valves, possibly introducing additional terms which take into account the subvalvular apparatus;

- the addition of complexity by introducing the contact forces exchanged among the leaflets, that may affect the dynamics in the early opening phase and in diastole;

- the investigation, regarding the model calibration phase, on an efficient semi-automatic calibration strategy of the model parameters or reduced order models and machine-learning-based surrogates of this complex system.

We remark that it is the first time that a 3D-0D FSI model is applied to the pulmonary artery and to the pulmonary valve. The pulmonary circulation is not much studied in literature and our work can be considered as a starting point in the context of coupled problems including the pulmonary valve.

Bibliography

[1] British heart foundation. Tetralogy of Fallot. *Understanding your child's heart.*

[2] Deal.II. URL `https://www.dealii.org/`.

[3] Life^x. URL `https://lifex.gitlab.io/lifex/`.

[4] Liverpool Heart and Chest Hospital. Ross procedure for aortic valve replacement. *Information for Patients & Families.*

[5] Matlab. URL `https://matlab.mathworks.com/`.

[6] Paraview. URL `http://www.paraview.org/`.

[7] Vmtk. The vascular modeling toolkit. URL `http://www.vmtk.org/`.

[8] Vtk. URL `https://www.vtk.org/`.

[9] Zygote Company. URL `https://www.zygote.com/`.

[10] F. Alauzet, B. Fabrèges, M. A. Fernández, and M. Landajuela. Nitsche-xfem for the coupling of an incompressible fluid with immersed thin-walled structures. *Computer Methods in Applied Mechanics and Engineering*, 301:300–335, 2016.

[11] B. Alsoufi, B. Fadel, Z. Bulbul, M. Al-Ahmadi, M. Al-Fayyadh, A. Kalloghlian, G. Siblini, and Z. Al-Halees. Cardiac reoperations following the Ross procedure in children: spectrum of surgery and reoperation results. *European Journal of Cardio-Thoracic Surgery*, 42(1):25–31, 2012.

[12] L. Antiga, M. Piccinelli, L. Botti, B. Ene-Iordache, A. Remuzzi, and D. A. Steinman. An image-based modeling framework for patient-specific computational hemodynamics. *Medical & Biological Engineering & Computing*, 46(11):1097–1112, 2008.

[13] C. Apitz, G. D. Webb, and A. N. Redington. Tetralogy of Fallot. *Lancet*, 374: 1462–1471, 2009.

[14] M. Astorino, J.-F. Gerbeau, O. Pantz, and K.-F. Traore. Fluid– structure interaction

and multi-body contact: application to aortic valves. *Computer Methods in Applied Mechanics and Engineering*, 198(45-46):3603–3612, 2009.

[15] F. Bailliard and R. H. Anderson. Tetralogy of Fallot. *Orphanet Journal of Rare Diseases*, 2009.

[16] Y. Bazilevs, V. M. Calo, J. A. Cottrell, T. J. R. Hughes, A. Reali, and G. Scovazzi. Variational multiscale residual-based turbulence modeling for large eddy simulation of incompressible flows. *Computer Methods in Applied Mechanics and Engineering*, 197:1–4, 2007.

[17] C. Bertoglio and A. Caiazzo. A tangential regularization method for backflow stabilization in hemodynamics. *Journal of Computational Physics*, 261:162–171, 2014.

[18] P. Besl and H. McKay. A method for registration of 3-D shapes. IEEE Trans Pattern Anal Mach Intell. *Pattern Analysis and Machine Intelligence, IEEE Transactions*, pages 239–256, 1992.

[19] P. J. Blanco and R. A. Feijóo. A 3d-1d-0d computational model for the entire cardiovascular system. *Computational Mechanics, eds. E. Dvorking, M. Goldschmit, M. Storti*, 29:5887–5911, 2010.

[20] A. Bordones-Crom, S. S. Patnaik, P. G. Menon, S. Murali, and E. Finol. Morphological Analysis of the Right Ventricular Endocardial Wall in Pulmonary Hypertension. *Journal of Biomechanical Engineering*, 143(7):074504, 2021.

[21] U. Bozlar, F. Ors, O. Deniz, M. Uzun, S. Gumus, M. S. Ugurel, F. Yazar, and C. Tayfun. Pulmonary artery diameters measured by multidetector-row computed tomography in healthy adults. *Acta Radiologica*, 48(10):1086–1091, 2007.

[22] P. Causin, J.-F. Gerbeau, and F. Nobile. Added-mass effect in the design of partitioned algorithms for fluid–structure problems. *Computer methods in applied mechanics and engineering*, 194(42-44):4506–4527, 2005.

[23] D. Chambers, C. Huang, and G. Matthews. *Basic physiology for anaesthetists*. Cambridge University Press, 2019.

[24] D. Chemla, V. Castelain, P. Hervé, Y. Lecarpentier, and S. Brimioulle. Haemodynamic evaluation of pulmonary hypertension. *European Respiratory Journal*, 20(5): 1314–1331, 2002.

[25] J. Chen, X.-Y. Lu, and W. Wang. Non-Newtonian effects of blood flow on hemo-

dynamics in distal vascular graft anastomoses. *Journal of Biomechanics*, 39(11): 1983–1995, 2006.

[26] L. Dedè, F. Menghini, and A. Quarteroni. Computational fluid dynamics of blood flow in an idealized left human heart. *International Journal for Numerical Methods in Biomedical Engineering*, 37:e3287, 2019.

[27] F. Domenichini and G. Pedrizzetti. Asymptotic model of fluid– tissue interaction for mitral valve dynamics. *Cardiovascular engineering and technology*, 6(2):95–104, 2015.

[28] P. D. Edwards, R. K. Bull, and R. Coulden. CT measurement of main pulmonary artery diameter. *The British journal of radiology*, 71(850):1018–1020, 2014.

[29] R. Fan, A. S. Bayoumi, P. Chen, C. M. Hobson, W. R. Wagner, J. E. M. Jr., and M. S. Sacks. Optimal elastomeric scaffold leaflet shape for pulmonary heart valve leaflet replacement. *Journal of Biomechanics*, 46(4):662–669, 2013.

[30] M. Fathallah and R. A. Krasuski. Pulmonic Valve Disease: Review of Pathology and Current Treatment Options. *Current Cardiology Reports*, 19(11), 2017.

[31] M. Fedele, E. Faggiano, L. Dedè, and A. Quarteroni. A patient-specific aortic valve model based on moving resistive immersed implicit surfaces. *Biomechanics and Modeling in Mechanobiology*, 16(5):1779–1803, 2017.

[32] M. A. Fernández and M. Moubachir. A newton method using exact jacobians for solving fluid-structure coupling. *Computers and Structures*, 83(2-3):127–142, 2005.

[33] M. A. Fernández, J.-F. Gerbeau, and V. Martin. Numerical simulation of blood flows through a porous interface. *ESAIM: Mathematical Modelling and Numerical Analysis*, 42(6):961–990, 2008.

[34] L. Formaggia and A. Veneziani. Reduced and multiscale models for the human cardiovascular system. *Lecture notes VKI lecture series*, pages 76–87, 2003.

[35] L. Formaggia, A. Quarteroni, and A. Veneziani. *Cardiovascular Mathematics: Modeling and Simulation of the Circulatory System.* Springer, 2009.

[36] L. Formaggia, A. Quarteroni, and A. Veneziani. *Cardiovascular Mathematics: Modeling and simulation of the circulatory system*, volume 1. Springer Science Business Media, 2010.

[37] D. Forti and L. Dedè. Semi-implicit BDF time discretization of the Navier-Stokes

equations with VMS-LES modeling in a High Performance Computing framework. *Computers & Fluids*, 117:168–182, 2015.

[38] I. Fumagalli, M. Fedele, C. Vergara, L. Dedè, S. Ippolito, F. Nicolò, C. Antona, R. Scrofani, and A. Quarteroni. An image-based computational hemodynamics study of the systolic anterior motion of the mitral valve. *Computers in Biology and Medicine*, 123:103922, 2020.

[39] I. Fumagalli, L. Dedè, and A. Quarteroni. A reduced 3D-0D fluid structure interaction model of the aortic valve that includes leaflets curvature. 2021.

[40] S. Ghiselli, C. Carro, N. Uricchio, G. Annoni, and S. M. Marianeschi. Mid- to long-term follow-up of pulmonary valve replacement with Biointegral injectable valve. *European journal of cardio-thoracic surgery*, 2020.

[41] A. Gilmanov and F. Sotiropoulos. A hybrid cartesian/immersed boundary method for simulating flows with 3D, geometrically complex, moving bodies. *Journal of Computational Physics*, 207(2):457–492, 2005.

[42] H. Gray. *Anatomy of the Human Body*. 20 edition, 2000.

[43] S. Grbic, R. Ionasec, D. Vitanovski, I. Voigt, Y. Wang, B. Georgescu, N. Navab, and D. Comaniciu. Complete valvular heart apparatus model from 4D cardiac CT. *Medical Image Analysis Journal*, 16(5):1003–1014, 2012.

[44] B. E. Griffith, R. D. Hornung, D. M. McQueen, and C. S. Peskin. An adaptive, formally second order accurate version of the immersed boundary method. *Journal of Computational Physics*, 223(1):10–49, 2007.

[45] J. D. Hart, G. W. M. Peters, P. J. G. Schreurs, and F. P. T. Baaijens. Collagen fibers reduce stresses and stabilize motion of aortic valve leaflets during systole. *Journal of Biomechanics*, 37(3):303–311, 2004.

[46] Humanitas. Mezzo di contrasto nella tac. URL `https://www.materdomini.it/visite-esami/il-mezzo-di-contrasto-nella-tac/`.

[47] Humanitas. Valvola polmonare, 2022. URL `https://www.humanitas.it/`.

[48] N. Institute of Biomedical Imaging and Bioengineering. Computed Tomography (CT). URL `https://www.nibib.nih.gov/`.

[49] A. Kandathil and M. Chamarthy. Pulmonary vascular anatomy & anatomical variants. *Cardiovascular Diagnosis and Therapy*, 8(3):201–207, 2018.

[50] D. Katritsis, L. Kaiktsis, A. Chaniotis, J. Pantos, E. P. Efstathopoulos, and V. Marmarelis. Wall Shear Stress: Theoretical Considerations and Methods of Measurement. *Progress in cardiovascular diseases*, 49(5):307–329, 2013.

[51] C. Kenney. What are Semilunar Valves?, 2022. URL `https://www.thehealthboard.com/`.

[52] V. O. Kheyfets, W. O'Dell, T. Smith, J. J. Reilly, and E. A. Finol. Considerations for numerical modeling of the pulmonary circulation - A review with a focus on pulmonary hypertension. *Journal of Biomechanical engineering*, 135(6):061011, 2013.

[53] W. T. Koiter. *A Consistent First Approximation In The General Theory Of Thin Elastic Shells. Part 1, Foundations And Linear Theory*. 1959.

[54] F. Kong, V. Kheyfetsand, E. Finol, and X.-C. Cai. An efficient parallel simulation of unsteady blood flows in patient-specific pulmonary artery. *International journal for numerical methods in biomedical engineering*, 34(4), 2017.

[55] F. Kong, V. Kheyfets, E. Finol, and X.-C. Cai. Simulation of unsteady blood flows in a patient-specific compliant pulmonary artery with a highly parallel monolithically coupled fluid-structure interaction algorithm. *International journal for numerical methods in biomedical engineering*, 35(7), 2019.

[56] T. Korakianitis and Y. Shi. Numerical simulation of cardiovascular dynamics with healthy and diseased heart valves. *Journal of biomechanics*, 39(11):1964–1982, 2006.

[57] B. C. Lampert. *Right Heart Catheterization*. Elsevier, 2018.

[58] A. Laudito, M. M. Brook, S. Suleman, M. S. Bleiweis, L. D. Thompson, F. L. Hanley, and V. M. Reddy. The Ross procedure in children and young adults: A word of caution. *The Journal of Thoracic and Cardiovascular Surgery*, 122(1):147–153, 2001.

[59] P. R. Lichtenthal. Normal hemodynamic parameters–adult. *J. Biomech.*, 2002.

[60] J. Liu, W. Yang, I. S. Lan, and A. L. Marsden. Fluid-structure interaction modeling of blood flow in the pulmonary arteries using the unified continuum and variational multiscale formulation. *Mechanics Research Communications*, 107:103556, 2020.

[61] F. B. M. O. C. B. A. G. M. Handke, G. Heinrichs. In vivo analysis of aortic valve dynamics by transesophageal 3-dimensional echocardiography with high temporal resolution. *The Journal of thoracic and cardiovascular surgery*, 125(6):1412–1419, 2003.

[62] E. N. Marieb. *Essentials of Anatomy and Physiology*. Benjamin Cummings, 4 edition, 2008.

[63] S. Osher and R. P. Fedkiw. Level set methods: an overview and some recent results. *Journal of Computational Physics*, 169(2):463–502, 2001.

[64] M. Padalino, V. L. Vida, and G. Stellin. Il paziente adulto dopo correzione chirurgica di tetralogia di Fallot: la storia infinita. *Giornale Italiano di Cardiologia*, 15(10):535–545, 2014.

[65] M. D. Patel, A. L. Dorfman, S. Yu, R. Lowery, M. G. Mahani, P. P. Agarwal, J. T. Christensen, and J. C. Lu. Neo-aortic Root Dilatation, Aortic Stifness, and Ventricular interactions in Long-Term Follow-Up After the Ross Procedure in Childhood. *Pediatric Cardiology*, 41:1107–1114, 2020.

[66] K. T. Patton and G. A. Thibodeau. *Anatomy & Physiology*. Mosby, 7 edition, 2010.

[67] K. Perktold and D. Hilbert. Numerical simulation of pulsatile flow in a carotid bifurcation model. *Journal of Biomedical Engineering*, 8(3):193–199, 1986.

[68] C. S. Peskin. Flow patterns around heart valves: a numerical method. *Journal of Computational Physics*, 10(2):252–271, 1972.

[69] G. Polazzo, A. Sapienza, and A. Zaccaria. Ricostruzione geometrica dell'arteria polmonare in pazienti con valvola autoespandibile. Laurea Triennale. Politecnico di Milano. 2021.

[70] A. Quarteroni, R. Sacco, F. Saleri, and P. Gervasio. *Matematica Numerica*, volume 77. Springer, 4 edition, 2014.

[71] A. Quarteroni, A. Veneziani, and C. Vergara. Geometric multiscale modeling of the cardiovascular system, between theory and practice. *Computer Methods in Applied Mechanics and Engineering*, 302(9):193–252, 2016.

[72] A. Quarteroni, A. Manzoni, and C. Vergara. The cardiovascular system: Mathematical modelling, numerical algorithms and clinical applications. *Acta Numerica*, 26: 365–590, 2017.

[73] F. Regazzoni, M. Salvador, P. Africa, M. Fedele, L. Dedè, and A. Quarteroni. A cardiac electromechanics model coupled with a lumped parameters model for closed-loop blood circulation. Part I: model derivation. *arXiv preprint arXiv:2011.15051*, 2020.

[74] E. Ruckdeschel and Y. Y. Kim. Pulmonary valve stenosis in the adult patient:

pathophysiology, diagnosis and management. *Education in Heart Congenital heart disease in adult patients*, 105(5), 2018.

[75] A. Rutten and M. Prokop. Contrast agents in X-ray computed tomography and its applications in oncology. *Anti-Cancer Agents in Medicinal Chemistry*, 7(3):307–316, 2007.

[76] F. Saremi, A. Gera, S. Y. Ho, Z. M. Hijazi, and D. Sánchez-Quintana. CT and MR imaging of the pulmonary valve. *Radiographics*, 34(1):51–71, 2014.

[77] F. J. Schoen. Cardiac valves and valvular pathology: update on function, disease, repair, and replacement. *Cardiovascular Pathology*, 4(14):189–194, 2005.

[78] J.-H. Seo, C. Zhu, J. Resar, and R. Mittal. Flow physics of normal and abnormal bioprosthetic aortic valves. *International Journal of Heat and Fluid Flow*, 86:108740, 2020.

[79] X. Shen, L. Bai, L. Cai, and X. Cao. A geometric model for the human pulmonary valve in its fully open case. *PLoS One*, 13(6):e0199390, 2018.

[80] X. Shen, Q. Yang, L. jin Li, L. Cai, and X. shan Cao. An Elastic Shell model for the Human Tricuspid Valve. *Acta Mathematicae Applicatae Sinica, English Series*, 35(1):111–128, 2019.

[81] X. Shen, Y. Xue, L. Bai, and L. Cai. An elastic shell model for the human pulmonary valve. *Journal of Elliptic and Parabolic Equations*, 6:99–112, 2020.

[82] Y. Shi, P. Lawford, and R. Hos. Review of Zero-D and 1-D Models of Blood Flow in the Cardiovascular System. *BioMedical Engineering OnLine*, 10(1):33, 2011.

[83] B. T. Tang, T. A. Fonte, F. P. Chan, P. S. Tsao, J. A. Feinstein, and C. A.Taylor. Three-dimensional hemodynamics in the human pulmonary arteries under resting and exercise conditions. *Annals of biomedical engineering*, 39(1):347–358, 2011.

[84] B. T. Tang, S. S. Pickard, F. P. Chan, P. S. Tsao, C. A. Taylor, and J. A. Feinstein. Wall shear stress is decreased in the pulmonary arteries of patients with pulmonary arterial hypertension: an image-based, computational fluid dynamics study. *Pulmonary circulation*, 2(4):470–476, 2012.

[85] G. J. Tortora and B. Derrickson. *Introduction to the human body : the essentials of anatomy and physiology. 8th ed.* John Wiley Sons, 8 edition, 2010.

[86] H. S. Udaykumar, R. Mittal, and W. Shyy. Computation of solid–liquid phase fronts

in the sharp interface limit on fixed grids. *Journal of Computational Physics*, 153(2): 535–574, 1999.

[87] R. van Loon, P. D. Anderson, and F. N. van de Vosse. A fluid-structure interaction method with solid-rigid contact for heart valve dynamic. *Journal of Computational Physics*, 217(2):806–823, 2006.

[88] E. Votta, T. B. Le, M. Stevanella, L. Fusini, E. G. Caiani, A. Redaelli, and F. Sotiropoulos. Toward patient-specific simulations of cardiac valves: State-of-the-art and future directions. *Journal of Biomechanics*, 46(2):217–228, 2013.

[89] L. Wang, M. Zhang, X. Chen, H. Hong, J. Liu, Z. Xu, L. Hu, Y. Zhong, Q. Jin, L. Chen, and Y. Zhang. Hemodynamic analysis of pulmonary arterial hypertension associated with congenital heart disease: a numerical study of patient-specific models. *11th International Congress on Image and Signal Processing, BioMedical Engineering and Informatics(CISP-BMEI 2018)*, 2018.

[90] W. G. Wier, M. N. Levy, and A. J. Pappano. *Cardiovascular Physiology: Mosby Physiology Monograph Series*. Elsevier Health Sciences, 2013.

[91] T. Xanthos, I. Dalivigkas, and K. A. Ekmektzoglou. Anatomic variations of the cardiac valves and papillary muscles of the right heart. *Italian Journal of Anatomy and Embryology*, 116(2):111–126, 2011.

[92] B. A. Zambrano, N. McLean, X. Zhao, J.-L. Tan, L. Zhong, C. A. Figueroa, L. C. Lee, and S. Baek. Patient-specific computational analysis of hemodynamics and wall mechanics and their interactions in pulmonary arterial hypertension. *Frontiers in bioengineering and biotechnology*, 8, 2021.

[93] L. Zheng and X. Zhang. *Modeling and Analysis of Modern Fluid Problems*. Elvisier, 2017.

[94] S. Zonca, C. Vergara, and L. Formaggia. An unfitted formulation for the interaction of an incompressible fluid with a thick structure via an XFEM/DG approach. *SIAM Journal of Scientific Computing*, 40(1):B59–B84, 2018.

A | Runge Kutta methods

Runge-Kutta methods are effective and widely used for solving the initial-value problems of differential equations [93]. They gain accuracy from the one-step structure, but they loose linearity due to an increasing number of functional evaluations at each step. In fact the difference between the Runga-Kutta methods and the classical numerical methods for ODEs (e.g. implicit and explicit Euler or the Crank-Nicholson method) is that the right-hand side term is multiple evaluated and consequently an accurate approximation is achieved [70].

We consider a Cauchy problem of this form:

$$\begin{cases} \dfrac{dy(t)}{dt} &= f(t, y(t)) \qquad t \in (0, T] \\ y(0) &= y_0 \end{cases}$$

We introduce a uniform partition of the time interval $[0, T]$ with step-size Δt and nodes $\{t^n\}_{n=0}^N$ such that $t^n = n\Delta t$. Accordingly, the time-discrete counterparts of all quantities, evaluated at time t^n, will be denoted by a superscript $\cdot^n$. We express with u^n the approximation of the exact solution $y(t^n)$ in the node t^n.

In the most general form, a Runge-Kutta method can be written as

$$u^n = u^{n-1} + \Delta t F(t^{n-1}, u^{n-1}, \Delta t; f) \qquad n > 0,$$

where F is defined in the following way:

$$F(t^{n-1}, u^{n-1}, \Delta t; f) = \sum_{i=1}^{s} b_i K_i,$$

$$K_i = f(t^{n-1} + c_i \Delta t, u^{n-1} + \Delta t \sum_{j=1}^{s} a_{ij} K_j) \qquad i = 1, 2, ..., s,$$

where s is the number of stages. The coefficients $\{a_{ij}\}$, $\{c_i\}$ and $\{b_i\}$ completely characterize the method, and they are typically collected in the so-called Butcher tableau:

$$
\begin{array}{c|cccc}
c_1 & a_{11} & a_{12} & \dots & a_{1s} \\
c_2 & a_{21} & a_{22} & \dots & a_{2s} \\
\vdots & \vdots & & \ddots & \vdots \\
c_s & a_{s1} & a_{s2} & \dots & a_{ss} \\
\hline
& b_1 & b_2 & \dots & b_s
\end{array}
$$

We suppose the following condition to hold:

$$
c_i = \sum_{j=1}^{s} a_{ij} \qquad i = 1, \dots s.
$$

If $a_{ij} = 0$ for $j \geq i$, with $i = 1, 2, \dots, s$, each K_i can be explicitely computed only with the $i-1$ coefficients $K_1, \dots, K_{i-1}$, previously computed. In this case the method is explicit, otherwise it is implicit and for the computation of the coefficients K_i it is necessary to solve a non linear system of dimension s, much expensive. Another possibility is the semi-implicit method. In this case $a_{ij} = 0$ for $j > i$ and consequently each K_i is given by the resolution of a non linear equation. Thus, a semi-implicit scheme requires the resolution of s non linearly independent equations [70].

We report some properties of the Runge-Kutta methods [70]:

- a Runge-Kutta method is consistent only if the condition $\sum_{i=1}^{s} b_i = 1$ is verified. Moreover if the method is consistent it is also convergent, since, for one-step methods, consistency implies stability and then convergence;

- a Runga-Kutta explicit method with s stages can not have order greater than s. Moreover Runge-Kutta explicit methods with s stages and with order s can not exist if $s \geq 5$. In Table A.1 it is possible to observe, for orders from 1 to 8, the minimum number of stages that is necessary to obtain a method of correspondent order. The maximum number of stages in correspondence of which the order is not less than the number of stages itself is 4.

order	1	2	3	4	5	6	7	8
s_{min}	1	2	3	4	6	7	9	11

Table A.1: Relation between order and minimum number of stages.

The classical 4th order Runge-Kutta explicit method is defined by means of the following Butcher tableau:

$$
\begin{array}{c|cccc}
0 & 0 & 0 & 0 & 0 \\
\frac{1}{2} & \frac{1}{2} & 0 & 0 & 0 \\
\frac{1}{2} & 0 & \frac{1}{2} & 0 & 0 \\
1 & 0 & 0 & 1 & 0 \\
\hline
 & \frac{1}{6} & \frac{1}{3} & \frac{1}{3} & \frac{1}{6}
\end{array}
$$

Therefore the solution reads:

$$
u^n = u^{n-1} + \frac{\Delta t}{6}(K_1 + 2K_2 + 2K_3 + K_4)
$$

where

$$
\begin{aligned}
K_1 &= f(t^{n-1}, u^{n-1}), \\
K_2 &= f\left(t^{n-1} + \frac{\Delta t}{2}, u^{n-1} + \Delta t \frac{1}{2}K_1\right), \\
K_3 &= f\left(t^{n-1} + \frac{\Delta t}{2}, u^{n-1} + \Delta t \frac{1}{2}K_2\right), \\
K_4 &= f(t^{n-1} + \Delta t, u^{n-1} + \Delta t K_3).
\end{aligned}
$$

The Runge Kutta methods can be easily extended to a system of ODEs of the form

$$
\begin{cases}
\dfrac{d\mathbf{y}(t)}{dt} = \mathbf{f}(t, \mathbf{y}(t)) & t \in (0, T] \\
\mathbf{y}(0) = \mathbf{y}_0
\end{cases}
$$

List of Figures

List of Tables

Acknowledgements